Implementation of Machine Learning Techniques in Brake NVH
Using Computational and Experimental Data

by

Morteza Gorzinmataee

A dissertation submitted in partial fulfillment
of the requirements for the degree of
Doctor of Philosophy
(Automotive Systems Engineering)
in the University of Michigan-Dearborn
2020

Doctoral Committee:

     Assistant Professor, Abdallah Chehade, Chair
     Assistant Professor, Georges Ayoub
     Assistant Professor, Zhen Hu
     Guanghui Liang, Ford Motor Company
     Nariman Mansouri, Ford Motor Company

Morteza Gorzinmataee

mgorzinm@umich.edu

ORCID iD: 0000-0001-9220-0293

ACKNOWLEDGEMENTS

TABLE OF CONTENTS

LIST OF TABLES

TABLE

LIST OF FIGURES

FIGURE

ABSTRACT

A complex system contains a broad range of intrinsic properties and parameters. Involved interconnections between parameters make it extremely difficult to decompose the system into pieces and predict its behavior. In automotive NVH, brake squeal is a dynamic instability phenomenon that contains complex physics due to its nature of the problem and complicated interconnections and variations; Also includes a wide range of operational conditions over a broad range of frequencies. Squeal noise is one of the most significant customer claims results in high warranty costs for vehicle manufacturers. Engineers study brake NVH using city and chassis dynamometer tests and computational techniques. These methods are costly and time-intensive. In recent years, by advancements in CAE tools and resources, numerical methods are vastly employed; They can replace physical experiments.

This research proposes and implements an innovative Machine Learning based technique on brake noise analysis and accelerates computational methods. The proposed approach introduces a new metric that explores correlations of operating condition distributions from the virtual and physical models. Data-driven methods incorporated with numerical simulations have been increasingly developed and utilized in recent years to improve virtual models' efficiency. This work demonstrates an ML-based model can significantly save computational cost by exploring an entire design space and skipping over duplicative iterations.

The second part of the research proposes and implements a multi-fidelity Deep Learning approach to predict brake pad NVH modal characteristics. This approach, inspired by both physics

and statistics. It leads to a perception of component properties, and sequentially, their modal responses. This work initially develops a high-fidelity numerical model and correlates with experimental data capturing brake pad component physical aspects. Then uses a Design of Experiment technique to generate a high-resolution database from CAE. This database is ultimately used to develop a physics-inspired deep learning model. The deep learning algorithm is composed of distinct multi-layer perceptron (MLP) modules that define component properties. The goal of this ML-based approach is to accelerate design and development processes in brake NVH and minimize urgency to additional experiments and simulations. This methodology may apply to other components and full system analysis.

CHAPTER I

Introduction

Research Background

Brake squeal is a complex phenomenon due to the dynamic instability emergence of resonant modes in the brake system. The excitation comes from the friction couple between pad linings and the disc [Massi et al. (2006), Akay (2002), and Hoffman and Gaul (2008)]. Several theories are describing possible root causes for brake squeal occurrence. One possible approach introduces an intermittent sticking phase that static frictional contact applies, followed by kinetic friction, in which a stick-slip phenomenon causes squealing. The other possible explanation is when two neighboring vibration modes couple due to a gradient increase of friction to create a complex, unstable mode in a nearby frequency. Another theory describes the sliding motion of caliper assembly toward the axial motion of discs, which induces a tangential load which excites the resonance mode of the system [Oberst and Lai (2011), Chen et al. (2003), Chen et al. (2003 a-b) and Ouyang (2005)]. Brake squeal is a high-frequency noise in a frequency range of 1 to 16 kHz, which is audible to both vehicle occupants and passers-by. This disturbing noise displeases passengers as well as the environment, which causes high customer dissatisfaction [Kinkaid et al. (2003) and Hamzeh et al. (1999) and Papinniemi et al. (2002)]. Squeal noise is reported to be one of the major customer claims, which result in high warranty costs for vehicle manufacturers [Ouyang et al. (2005) and Triches et al. (2004)].

During last years, the brake squeal problem has been studied by experimental approaches such as vehicle tests, chassis dynamometer tests, and modal tests as well as analytical methods and numerical simulations such as finite element analysis (FEA) [Papinniemi et al. (2002), Nagy et al. (1994) and Liles (1989)]. However, with all these approaches, squeal predictions in the early phase of the design are not achieved yet. Analytical approaches integrated with numerical finite element simulation provide a somehow understanding of brake squeal after the model calibrated with some level of test data. With the advances in CAE tools, it is now feasible to develop a machine learning tool integrated with the FEA model that facilitates brake squeal prediction.

A full vehicle city test is a standard procedure currently is used in many OEMs for the final sign-off and validations for the brake squeal performance. However, this procedure is highly expensive and time inefficient to be conducted on the roads. This approach is not suitable for design recommendations in an early design phase because the experiment requires manufactured parts or a prototype vehicle. The chassis dynamometer test is also a decent representative of the full vehicle behavior within the laboratory environment. It is capable of accurately replicate squeal noise, and it consists of a full range of operating conditions. The dyno test is a standard procedure and can be performed in a design stage by building prototype test fixtures and subassembly parts. It still requires physical components to be fabricated and expensive test equipment and facilities to complete the test. However, both dyno and vehicle tests are undesirable for design iterations and recommendations.

Nonetheless, the numerical simulations and analytical approach do not require any physical parts or facilities, and the analysis can start in the very early stage of the design. Computational methods (CAE) could potentially predict squeal performance if a high-resolution model is available. It also can be a time-saving and cost-efficient approach in the long run that is easy to

implement for studying more design iterations. On the other side, the CAE methods are computationally expensive. They require an understanding of the system's physics and modeling of detailed interactions, material properties, and existing nonlinearities. Also, the number of operating conditions to be run in CAE is quite large. Besides, it requires other expensive tests in addition to the dyno test for correlations and validations. Table I.1, lists the positive and negative attributes related to these three main approaches currently is used in studying the brake squeal noise.

Table I.1. Advantages and disadvantages of current approaches in studying brake squeal noise

Approaches	Advantages	Disadvantages
Full vehicle Test	1- Accurate in replication of real noise events 2- Reliable procedure for sign-off and final validations 3- For subjective and objective evaluations	1- Highly expensive and time-taking 2- Physical parts and prototype vehicle are required
Prototype Chassis Dynamometer Test	1- Accurate method for noise prediction 2- Consists of the full range of operating conditions 3- Capable of capturing the part variations 4- The test can be conducted in the design stage	1- Expensive equipment and facilities 2- Physical prototypes need to be manufactured 3- The procedure requires building a test fixture 4- The procedure is relatively time-taking takes
Numerical Simulations and Analytical Solutions	1- No physical parts or facilities required 2- Analysis can start in very early stage of the design and lead the design 3- Easy to implement several iterations for design recommendations 4- Time saving and cost efficient in long run 5- Capable of capturing part variations	1- Computationally expensive 2- Requires modeling of interconnections, materials and nonlinearities 3- Not accurate enough yet for predicting of squeal 4- Requires other expensive tests for validations

From a vehicle or chassis dynamometer test, noise occurrence and sound pressure data are collected over a range of frequencies, temperatures, pressures, and velocities of brake pads and rotor. The number of noise occurrences and amplitudes of sound pressure (dB level) determines an intensity of noise from Fast Fourier Transform (FFT) [Cerna (2000)]. The correlation between vehicle road test and dynamometer test and the correlation between two dyno tests are common problems in brake squeal due to the environmental factors and variations in the components. Therefore, repeatability for tests is essential; however, both vehicle and dyno tests are highly costly. The other challenge is a correlation between computational models as an alternative low-cost solution and physical experiments.

Furthermore, complexity for subsystem interactions in a wide range of operating conditions such as temperatures, pressures, and frequencies induce a severe nonlinear model to capture all real test aspects. A system considered complex when it contains many intrinsic properties and parameters, and convoluted interconnections exist between parameters that make it extremely difficult to decompose the system and predict its behavior. It is incredibly challenging to adequately explain a complex system by pure experimental and computational methods. Plenty of interdependent variables result in a massive number of input dimensions to be accounted for analysis. Besides, not all variables can be sufficiently modeled and embedded into the correlation examination. Based on the preceding, constructing such a CAE model to compromise all the operating conditions and variations is not computationally feasible.

Machine learning (ML) models in recent years played a pivotal role to support critical decision making, automation of time-consuming processes, predicting complicated systems, and advancing scientific discoveries [Karpatne et al. (2017), Karpatne et al. (2018), Nathan (2017) and Rahul Rai and Chandan (2020), Baker (2019)]. State-of-the-art machine learning research has been

4

making significant progress in many directions. In engineering, due to an increasing evolution of standard testing and design rules, ML has potential applications for product characteristics identification, decision-making, and process optimization, specifically in product developments [Willard et al. (2020)]. ML-based model aspires to equip a system with an intelligent element to automatically improve its performance through experience, pattern recognition, and statistical inference [Pham and Afify (2005)]. Progressive ML techniques discover sophisticated data patterns and transform information into an autonomous system that imitates human intelligence and activities [Panchal et al. (2019)]. ML techniques increasingly developed and deployed in growing engineering and technology industries in a wide range of activities from the tuning of numerical parameters [Lynch et al. (2019)] and synthesizing high-dimensional optimizations [Chen and Fuge (2019)] to extracting human preferences and design strategies [Raina et al. (2019)]. On the flip side, predicting behaviors for complex systems by only exploring correlation and reasoning relationships between inputs and outputs could be inefficient and may have multiple drawbacks. Besides, by developing the physics-based models, it is expansive and infeasible to run many design iterations within the demanded resolution. Because neither an absolute ML-based nor an explicit physics-based methodology alone functions effectively for complex science and engineering problems. Thus, researchers are recently studying the continuum between mechanistic and ML models to incorporate merits from science-based and data-driven learnings [Karpatne et al. (2017) and Rahul Rai and Chandan (2020)].

Integrating science-based principles and ML models in a synergistic fashion appears to be an efficient technique to accelerate the computationally expensive physics-based model. The essential to this approach is to generate a data repository that could be used to discover a pattern for predicting of system's outcome. In many cases, the disadvantage of this technique is that the

prediction is unreliable beyond a range of tested input variables. In training a machine learning algorithm directly from the operative data, the model prediction capability shrinks as parameters diverge from trial data, knowing that machine learning algorithms tend to fail predictions with extrapolation nature. One remedy to improve predictive ability is to implement a physics-guided machine learning algorithm with a structured architecture that accounts for the complexity of input features and variables and allows for expansion of the range for variables independently at any point. This facilitates the machine learning algorithm's training by employing a structured framework designed based on the physical properties of the data. This technique provides a more precise image to find the patterns according to the underlying physics of the system [Willard et al. (2020), Karpatne et al. (2017), Schleder et al. (2019), Ivezic et al. (2019) and Raccuglia et al. (2016)].

The current chapter outlines firstly, introduction and research background, and secondly, problem statements. Contributions of this scholarly research are multi-fold, which are summarized in the chart shown in Figure I.1. In chapter II, (1) Recent advancements in CAE models for brake squeal systems and correlations and validations process between numerical approach and physical squeal test are described and elaborated. Chapter III, in the first place, (2) provides a metric to validate unstable modes without a need to run expensive tests such as laser vibrometers and full-field operational deflection shapes. At the end of Chapter III, (3) A machine learning-based physics-inspired model is developed that efficiently reconstructs CAE outputs for squeal analysis. In Chapter IV (4), a physics-guided multi-resolution deep learning technique proposed to predict brake pad NVH modal characteristics from its physical properties.
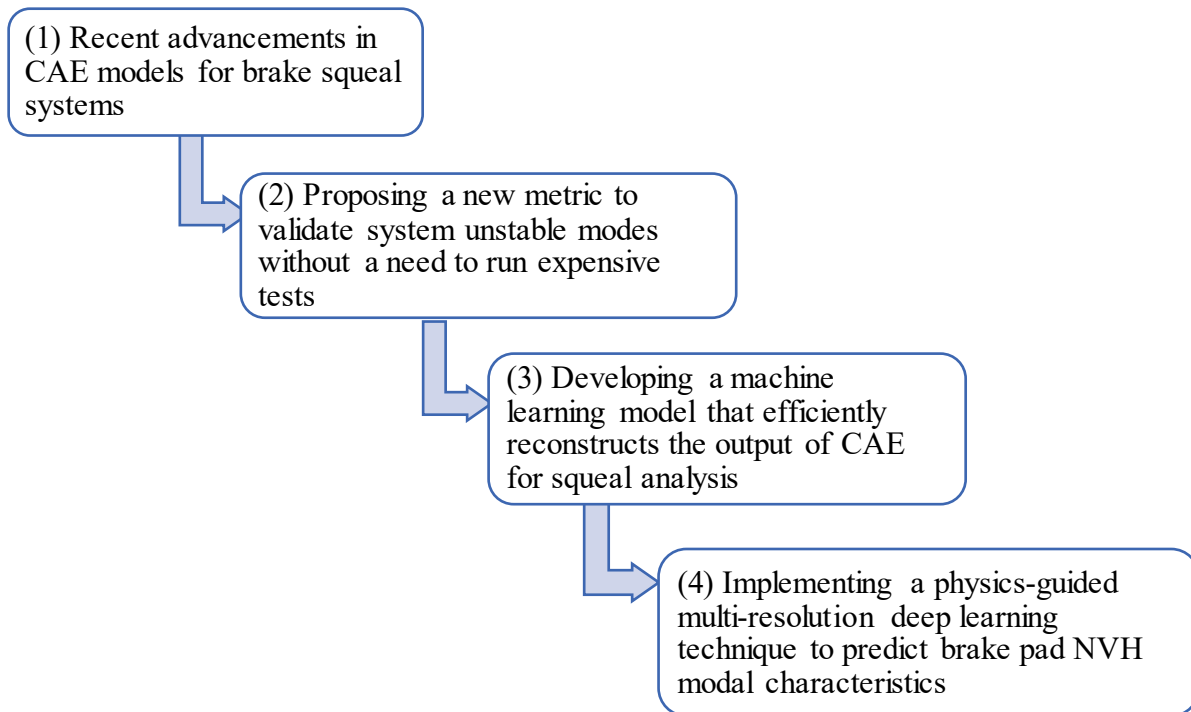
Figure I.1. The research contribution chart

Problem Statement

However, numerical approaches are currently primarily efficient tools for addressing brake squeal noise in product development; These methods are expensive in terms of the computational time and number of simulation jobs to incorporate a high-fidelity Finite Element (FE) model. It also depends on the scale of operating conditions that need to be considered in the analysis. The number of operating conditions depend on the operating parameters such as brake pressure and temperature, friction between pad and disc, rotational speeds of the disc, and component's property-dependent materials for frequency and temperature variations. The computational time for running one operating condition using a FE model with approximately half a million elements

7

takes nearly 2 hours on a supercomputer. A full Finite Element Analysis (FEA) job with all the operating conditions that replicate a standard range of parameters for a dynamometer test could take several weeks to complete on a supercomputer. Considering modeling correlations and post-processing time and sequentially design iterations using such a model, it would be computationally expensive and exhaustive to pursue such an approach. A Machine Learning (ML) model that is architected from the system's physics and trained based on combined CAE and experimental data and can compromise a whole range of operating conditions can only take few seconds to run on a local computer. Figure I.2 summarizes challenges with the current approaches (Physical test and numerical approach) and the alternative proposed approach. Both the physical experiment and CAE are expensive and time-taking and have limitations in the number of runs.

The ML model, however, is cost and time-efficient. Still, there are several challenges: (1) Infrastructure for data collection and acquisition, (2) Data sparsity, integrity, and dynamics (3) Precision and predictability of the model, and (4) Model generalizations and extrapolations. One crucial challenge ahead is, essential infrastructures required for collecting and processing data. Regardless, leveraging data from external sources is adopted in many cases, and it could be an acceptable practice to save time and accelerate the process. Yet, there is no quality control on how data is collected.

On the other hand, spending internal resources on collecting data could be costly and time-intensive. Besides, data integrity is essential to ensure consistency and fidelity of analysis. Static data could be just as good as a starting point, but in complex behavior, dynamic data required, which adds more cost and time to the process. The chain of data custody is also critical to assure data acquired as intended. The precision and predictivity of the model depend on multiple involved

factors. Most importantly, a machine-learned model that captures a system's fundamental physics is in the likelihood of being more reliable and better predictive.

Moreover, it is essential to optimize the model parameters and hyperparameter to reach a global optimal solution. Extending prediction behavior and extrapolation usually is a failure for most data-constrained machine learning algorithms because machine learning algorithms would only interpolate within the constraint of the given data. Still, estimation outside the box is impractical unless adding mechanistic features to the algorithm to enhance the model's structure.

However, in this research, the goal is not to generate an autonomous ML model to replace CAE completely. The main objective here is to advance the correlation of CAE to Dyno and accelerate the process when a large number of operating conditions are required. The aim is to improve the correlation precision and ultimately reduce the analysis cost by saving engineering hours spent on an expensive validation procedure and post-processing for the numerical model. In this work, a computationally efficient ML-based model is proposed to effectively replicate the CAE results and identify the real unstable modes representing the brake squeal noise using an innovative metric.
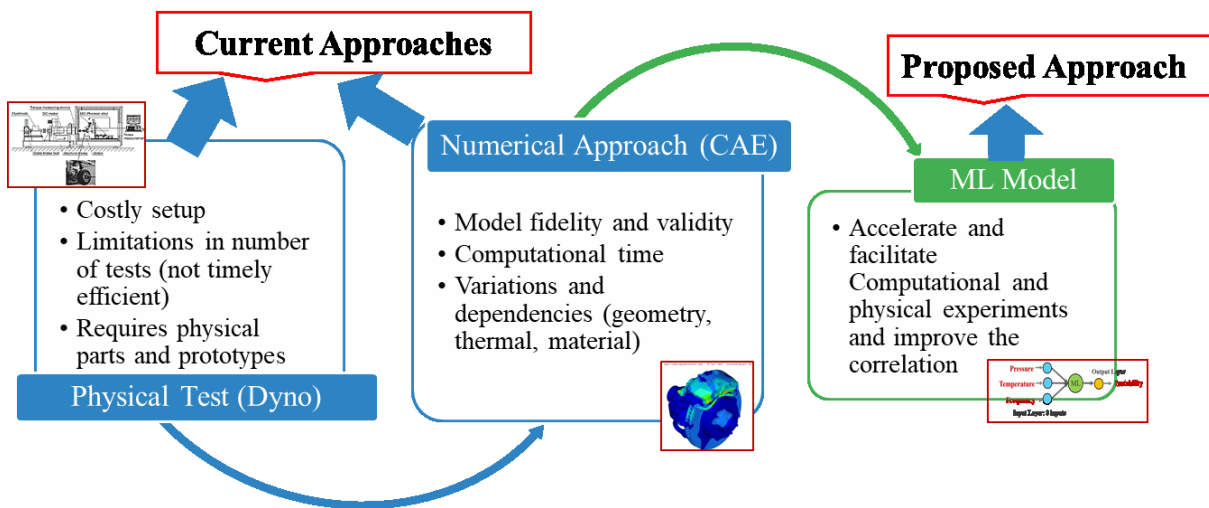
Figure I.2. Challenges for current approaches in brake system squeal analysis using: physical test, numerical model and the proposed ML-based approach

For components in bake NVH, physical tests and numerical simulations are currently used to investigate their modal characteristics. Studies indicated an association of system and component mode-coupling on brake squeal noise. Aforementioned, that at high-frequency noise, this circumstance has mainly driven by pads and rotor modal characteristics. The brake pad, known as the vibration excitation source, considerably impacts brake noise and vibration performance. Researchers studied this phenomenon, demonstrated the influence of subsystems' eigenfrequencies and eigenmodes on overall system response. Computational physics-constrained methods developed to explore component's modal characteristics precisely and simulate the experimental tests based on these observations. However, shortcomings of these physics-based models are 1- They still rely on physical inspection of parts, 2- Tuning of materials and geometries to incorporate variations and nonlinearities, and 3- Accordingly, this practice is computationally expansive and time-taking.

Meanwhile, an Artificial Intelligent (AI) tool that utilizes a deep learning algorithm by inspiration from both physics and statistics could be an effective method to accelerate and facilitates this procedure. The proposed technique can be applied to all brake system components and efficiently accelerate NVH analysis and developments. This approach aims to enable an efficient technique for component study and avoid redundancy for analysis.
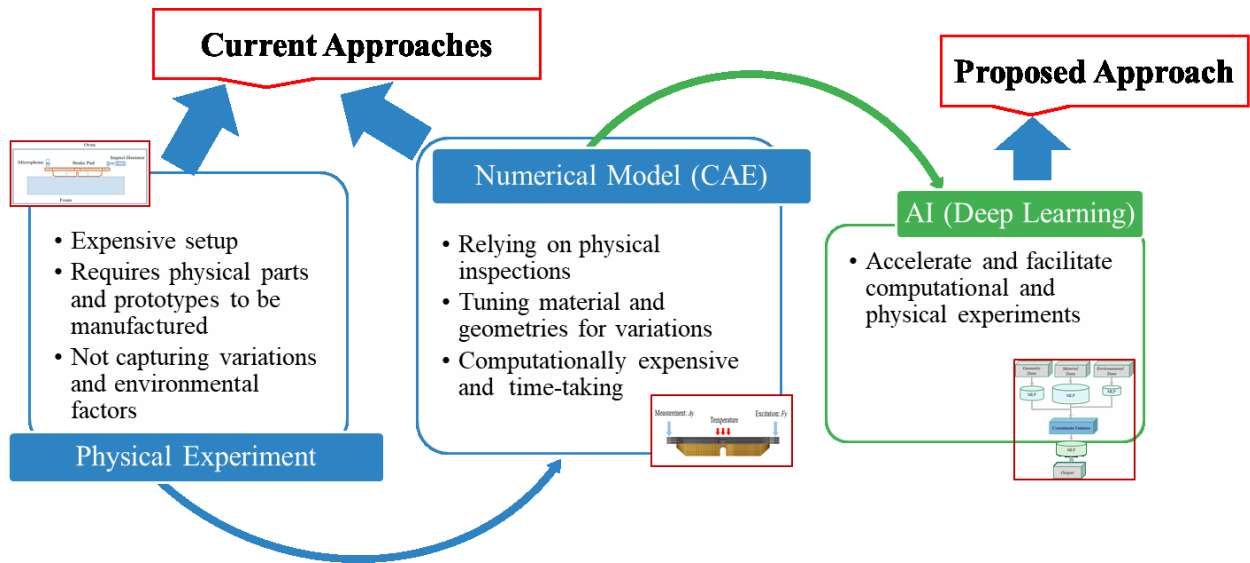
Figure I.3. Challenges for current brake pad component NVH analysis using: physical test, numerical model and the proposed deep learning approach

CHAPTER II

CAE Advancements in Brake Squeal

There are mainly two numerical FEA approaches for brake squeal analysis in CAE. One is Transient Analysis, which studies the brake system's vibration through dynamic loading of braking. The transient analysis uses a Fourier transform for transformation from the time domain to the frequency domain to compute squeal frequencies. Simulation time for transient analysis is quite large; moreover, this analysis cannot provide information on the system's unstable modes. The other approach, which is more desired by CAE analysts, is Complex Eigenvalue Analysis (CEA), which determines the system's instabilities under small perturbation.

This approach calculates complex eigenvalues of the system under certain boundary conditions and braking preloads [Triches et al. (2004), Nagy et al. (1994) and AbuBakar and Ouyang (2006)]. Damping ratios of the system are calculated from real parts, and imaginary parts of eigenvalues and the imaginary parts also identify instabilities in the system [Adhikari and Friswell (2007) and Adhikari (2000)]. It is mathematically proven that a negative damping ratio at a specific frequency indicates the presence of an unstable mode at that frequency [Kang et al. (2009)]. This approach is relatively fast and provides more information such as complex mode shapes and coupling modes; additionally, contributions of subsystems of unstable modes at specific frequencies.

However, the major issue with using CEA is an over-prediction of noise. The CAE model includes many false positives and delivers much more unstable modes than the real noise event occurs in a physical test. Calibration is required for CAE model parameters that need additional validation tests to overcome over-prediction and mitigate the false positives issue. One critical test is a Frequency Response Function (FRF) test for subsystems. The test provides information such as precise dynamic stiffness and damping properties of components. Another important test is a contact pressure distribution scan, which offers pressure contours of contact surfaces. The latter is crucial for calibrating the model for component interactions under static braking load. Besides the fact that these calibration tests are expensive and time-consuming, they do not entirely solve the over-prediction problem, and still, false positives occur with the CEA approach.

CAE Analysis Using Numerical Approach for Brake Squeal

Currently, numerical approaches are primarily efficient tools for brake squeal investigations in product development. But they are still expensive for computational time and scale of simulation jobs that need to incorporate for a high-fidelity model. Hence, it depends on a variety of operating conditions to be considered. The brake system operating conditions are physical and environmental parameters, including brake pressure and temperature and friction between pad and disc, the disc's rotational speed, and component property dependent materials for frequency and temperature variations.

A brake system in the analysis consists of subsystems, including brake rotor, pads, shims, caliper, piston, mount, and drive. Figure II.1 shows the assembly of brake squeal analysis components under the computational model in this study.
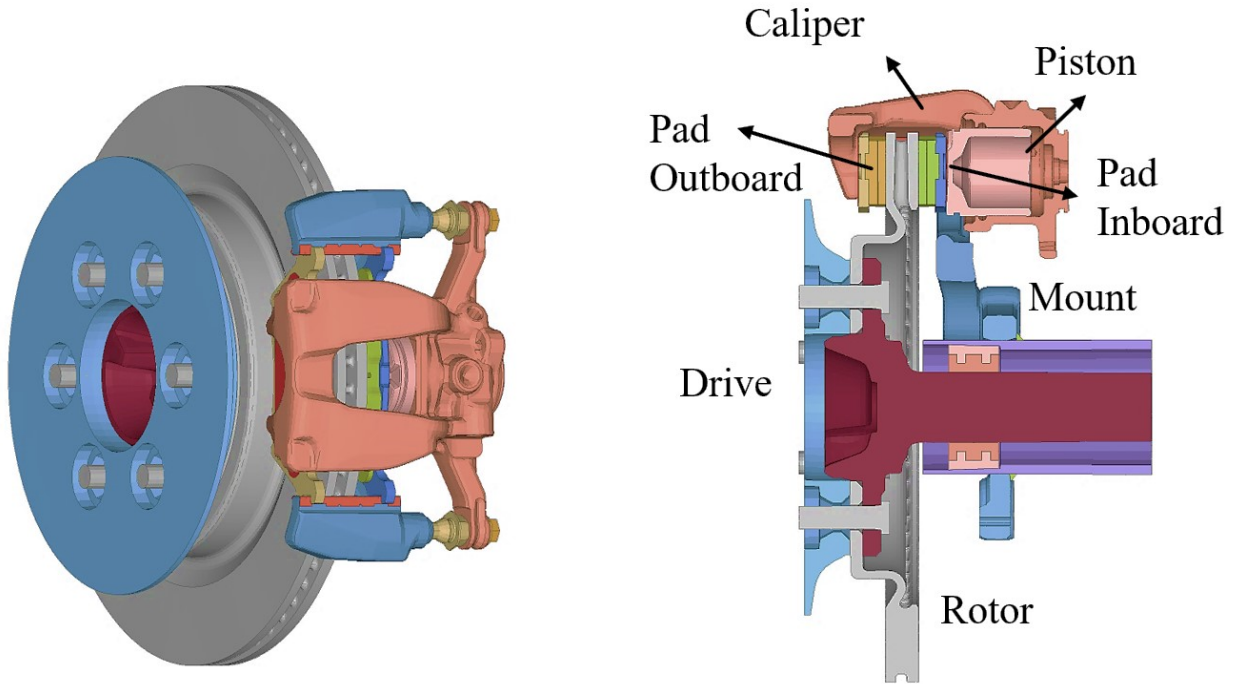
Figure II.1. A 3D model of brake assembly in brake squeal analysis

This section describes a finite element (FE) model for brake NVH system, including subsystems and interconnections. Then, it discusses the most recent and common numerical approach to represent the physics of the system. The FE model contains a detailed high-resolution element representation of components from their 3D CAD geometries. Additionally, the material properties and element formulation assigned to create a modal stiffness matrix. For initial modal analysis, the eigenvectors of components normalized, as shown in the formulations in Table II.1. The diagonal features in the modal stiffness matrix represent eigenvalues, and the modal mass matrix given by a unit matrix. K indicates the modal stiffness matrix for each component, and λ stands for the respective eigenvalue matrix composed of eigenvalues (for eigenmodes from 1 to n) [Garg (1973) and Lee et al. (1996) and Lee (2000)].

14

Table II.1. Modal stiffness matrix for brake components

Component	Modal Stiffness Matrix
Rotor	$$K_{Rotor} = I\{\lambda_{Rotor}\} = \begin{bmatrix} \lambda^1_{Rotor} & \cdots & 0 \\ \vdots & \ddots & \vdots \\ 0 & \cdots & \lambda^n_{Rotor} \end{bmatrix}$$
Pad	$$K_{Pad} = I\{\lambda_{Pad}\} = \begin{bmatrix} \lambda^1_{Pad} & \cdots & 0 \\ \vdots & \ddots & \vdots \\ 0 & \cdots & \lambda^n_{Pad} \end{bmatrix}$$
Shim	$$K_{Piston} = I\{\lambda_{Shim}\} = \begin{bmatrix} \lambda^1_{Shim} & \cdots & 0 \\ \vdots & \ddots & \vdots \\ 0 & \cdots & \lambda^n_{Shim} \end{bmatrix}$$
Caliper	$$K_{Caliper} = I\{\lambda_{Caliper}\} = \begin{bmatrix} \lambda^1_{Caliper} & \cdots & 0 \\ \vdots & \ddots & \vdots \\ 0 & \cdots & \lambda^n_{Caliper} \end{bmatrix}$$
Piston	$$K_{Piston} = I\{\lambda_{Piston}\} = \begin{bmatrix} \lambda^1_{Piston} & \cdots & 0 \\ \vdots & \ddots & \vdots \\ 0 & \cdots & \lambda^n_{Piston} \end{bmatrix}$$
Mount	$$K_{Mount} = I\{\lambda_{Mount}\} = \begin{bmatrix} \lambda^1_{Mount} & \cdots & 0 \\ \vdots & \ddots & \vdots \\ 0 & \cdots & \lambda^n_{Mount} \end{bmatrix}$$
Drive	$$K_{Drive} = I\{\lambda_{Drive}\} = \begin{bmatrix} \lambda^1_{Drive} & \cdots & 0 \\ \vdots & \ddots & \vdots \\ 0 & \cdots & \lambda^n_{Drive} \end{bmatrix}$$

Correspondingly, the structural stiffness matrix for assembly of the brake components given as:

(Equation II.1)

$$K_{structural} = \begin{pmatrix} K_{Rotor} & 0 & 0 & & & & \\ 0 & K_{Pad\,IB} & 0 & -0- & & -0- & \\ 0 & 0 & K_{Shim} & & & & \\ & -0- & & K_{Caliper} & & -0- & \\ & & & & K_{Piston} & 0 & 0 \\ & -0- & & -0- & 0 & K_{Mount} & 0 \\ & & & & 0 & 0 & K_{Drive} \end{pmatrix}$$

The structural stiffness matrix is a diagonal matrix composed of components' eigenvalues. The structural stiffness is useful for optimizing the system's structure for NVH performance and mitigating squeal noise.

Other critical elements for system stiffness are interconnections between components and frictional interactions between rotor and pads. Precisely modeling of interconnections is crucial for achieving a high-fidelity paradigm. Examining transfer energies from the components facilitate to verify if interactions are adequately captured. This can be studied by correlation and comparing the frequency response functions in subassemblies from the computational model to the physical system. The other critical element is a fictional representation of the pad-to-rotor interface. Previous research believed this is the most important consideration in modeling and simulating brake squeal using numerical approaches. The frictional mechanism in simulations must incorporate nonlinear and asymmetric behavior for contact pressure distributions [Lee et al. (1996) and Spurr (1971)]. The interconnection between rotor and pads is considered a spring-type connection, as shown in Figure II.2, when they are fully engaged.
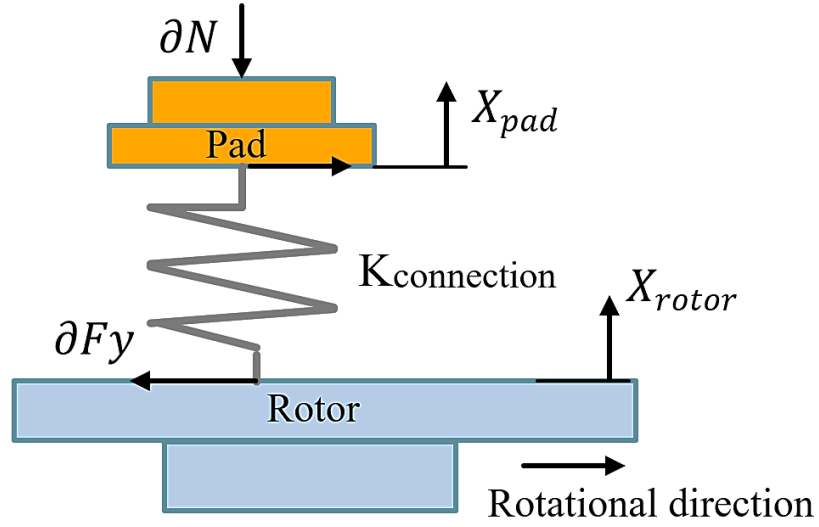
Figure II.2. A schematic of physical interactions between brake rotor and pad

Variation of the brake force is proportional to the friction coefficient and the variation of the normal force as written in Equation II.2:

(Equation II.2)

$$\partial F_y = \mu . \partial N$$

Where μ is the friction coefficient, and ∂N is the variation of the normal force.

The variation of the normal force can also be written in terms of connection stiffness and the relative displacement of the pad to the rotor as below:

(Equation II.3)

$$\partial N = K_{connection} . (X_{pad} - X_{rotor})$$

On the other side, the equation of motion is presented as:

(Equation II.4)

$$M\ddot{x} + Kx = F_{friction}$$

Where $F_{friction}$ is given by:

(Equation II.5)

$$F_{friction} = K_{friction}.x$$

By combining Equations II.2- II.5, the equation of motion becomes homogenous and represents in Equation II.6. According to Equation II.6, the resultant stiffness matrix becomes asymmetric in the aftermath of friction term [Lee (2000) and Mottorshead et al. (1997)]; Therefore, the eigensolutions appear in a complex form. As a result, the frictional force induces asymmetric formulation to the system stiffness matrix.

(Equation II.6)

$$M\ddot{x} + (K - K_{friction}).x = 0$$

Including all the terms in the modal stiffness matrix, it is given as equation below:

(Equation II.7)

$$K = K_{structural} + K_{connection} + K_{friction}$$

Since the modal mass matrix is normalized, the friction force and interconnections won't affect it. Therefore, the modal stiffness matrix contains all necessary information for system analysis.

The two most recent and popular approaches for analyzing brake squeal are 1- Complex eigenvalue analysis (CEA) and 2- Transient analysis.

This research employs the Complex eigenvalue analysis (CEA) approach rather than the transient analysis for studying brake squeal. CEA is the most common approach and relatively time-efficient comparing to transient analysis. It also leverages examining a more comprehensive range of operating conditions that could mimic the real physical test. A 5-step CEA approach used in this research work consists of the following:

- Step 1: Static pretension clamp load of rotor-wheel-hub bolts

- Step 2: Static pressure load of piston and caliper that induces pads to rotor contacts

- Step 3: Static step to induce steady-state rotation of brake disk and pad-to-rotor nonlinear friction establishment

- Step 4: Extraction of natural frequencies of the system under the brake loading and boundary conditions

- Step 5: Extraction of complex eigenvalues of the system and mode shapes of unstable modes

The FE model for brake squeal system studied in this work includes nearly half a million elements. FE model is developed from a 3D solid mesh model of all the components in the brake assembly. The system's boundary is a portion of the wheel from one side and a part of the axle tube and hub from the other side. Because wheel and axle components have a minimal impact on the problem's frequency range, only a part of those components is included to capture contact interactions. This assumption reduces the computational time for analysis.

Overview of Brake Squeal CEA

Several theories describe instability of brake squeal, including (i) a stick-slip contact of frictional material and disk, (ii) a modal coupling of two neighboring vibration modes of the system, (iii) a cross-coupling tangential excitation and, (iv) an axial oscillation due to frictional force of disk to pads [Hoffmann et al. (2002)].

To solve a complex eigenvalue problem: Firstly, Normal Mode Analysis extracts the natural frequency of an un-damped system under static loads and constraints. Next, by incorporating the effect of a friction coupling, Eigensolver extracts complex eigenvalues of the

system utilizing a projection method [Bajer et al. (2003) and Bajer and Belsky (2004)]. The equation for the complex eigenvalue problem is given by:

(Equation II.8)

$$(\lambda^2 [M] + \lambda[C] + [K])\{\psi\} = F_{ext}$$

Where [M] indicates the mass matrix, [C] is damping the matrix and [K] is the stiffness matrix of the brake system. The damping matrix includes frictional induced damping and material damping. F_{ext} is the external force. Also, λ and ψ are eigenvalue and eigenvector terms correspondingly that defines system vibration modes. It is worth noting here that the mass matrix [M] is symmetric. However, the stiffness matrix [K] is an un-symmetric matrix due to inclusion of the frictional effect, which includes loading conditions from the aforementioned static steps. The right side of the equation is zero since squeal problem is a self-excited vibration.

The eigenvalues of the system present in a complex form as below due to the un-symmetric stiffness matrix of K [Nouby et al. (2011), Nouby et al. (2009), and Esgandari et al. (2013)]:

(Equation II.9)

$$\lambda_i = a_i + i\omega_i$$

Where a_i is the real part and ω_i is the imaginary part of complex mode 'i'. Thus, the damping ratio of the system represents the equation below:

(Equation II.10)

$$\zeta i = -2\frac{a_i}{\omega_i}$$

The system becomes unstable when the real part of the eigenvalue becomes positive, which induces a negative damping ratio [Esgandari et al. (2013), Kang et al. (2009) and Caughey]. In brake squeal analysis using the CEA approach, the negative damping ratio indicated the tendency of noise in a brake system model. A major complication of the CEA approach in brake squeal is

20

over-prediction. Generally, there will be much more unstable modes from the numerical model results than those observed in the physical test. Therefore, the prediction of noise in the early stage of the program is unfortunate. On the other hand, instability results are highly sensitive to a small variation in components' geometries and materials and subsystem interactions and system operating conditions. Material properties and surface interactions are also nonlinearly dependent on temperature changes during braking operations and frequency range. Besides, the frequency range of the problem is quite extensive, often from 1 kHz to 16 kHz.

Although one potential remedy to address the over-prediction problem is to include the components' damping properties, capturing the proper damping is another challenge in CEA. To overcome these challenges, the numerical model has to correlate with an initial dyno test result. Alongside this, an additional validation test is required to validate this correlation and calibrate the model.

CAE to Test Correlation and Validation

Using the CEA approach, CAE simulations generate several unstable data points in a given frequency range, depending on the number of operating conditions considered in the analysis. Many of these instabilities are false positives and may not occur as a noise event in the dyno. Figure II.3 shows the comparison between CAE and dyno test plot for a production Ford vehicle. Here, the CAE result is computed based on system negative damping as indications of the system instabilities through a range of frequency from 0 to 16 kHz. The dyno noise results are in dB level through the test's given frequency range and operating conditions.

From CAE data, several false positives are occurred, which are not observed as a noise event in the dyno test. This indicates the challenge of using a numerical model for the prediction of squeal noise. Without a valid touchstone, instability result alone is a sophisticated metric and even can be contradictory and misguiding for decision making.
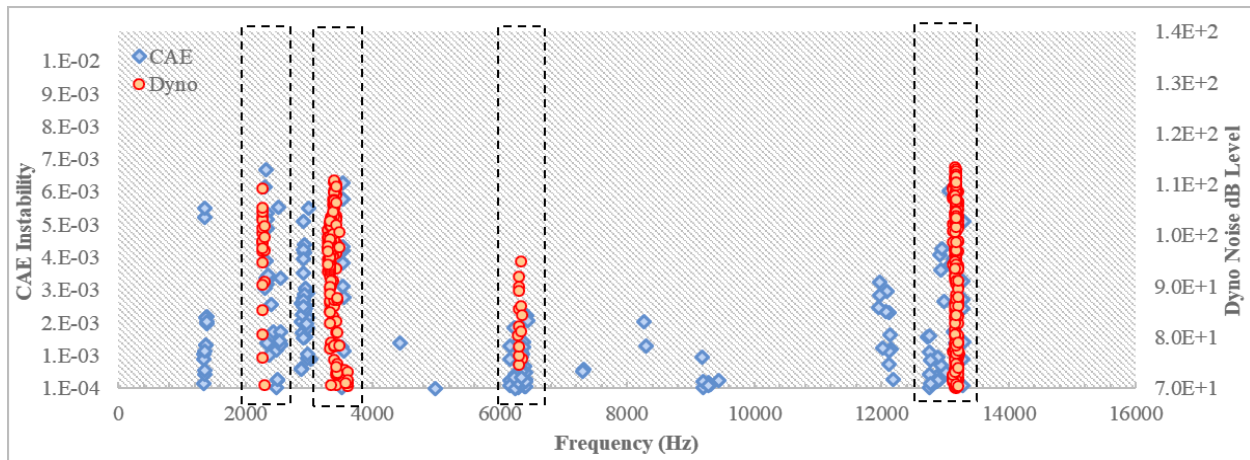
Figure II.3. Comparison of CAE (system instability) and dyno test (noise occurrence) for the frequency range of brake squeal from 0 to 16 Hz

In order to evidently differentiate between false and true positive instabilities, currently, an expensive technique is being carried out. One approach is to validate the system's unstable mode shape by comparing the CAE mode shapes versus the Dyno test mode shapes at the target frequency. However, computing a 3-Dimensional (3D) displacement of the unstable modes in CAE is affordable; the post-processing and visualizing of such a mode shape is a tedious process when the number of the data point is extensive. This is highly dependent on the number of operating conditions that are executed in the analysis. An expensive technique is currently used to verify CAE to dyno result correlation and identify real instabilities from the false positives. The current approach validates the system's unstable mode shape by comparing the CAE to Dyno mode shapes at a target frequency. However, computing and post-processing for the 3-Dimensional (3D) unstable modes in CAE is a tedious process when the number of data points is extensive. The

22

number of CAE data points highly depends on the number of operating conditions considered in the analysis.

Besides, additional physical experiments are required to identify the dyno test mode shape. One approach is non-contact full-field vibration analysis. Such analysis is a high-speed scanning laser vibrometer test to enable measurement of full-field operational deflection shape for brake components under a transient excitation enforcing braking load. The experimental measurement from the deflection shape test is compared to CAE to validate the CAE analysis's true mode shape. This validation is to distinguish the true unstable mode from the false one.

Figure II.4 shows the brake disk's measured deflection shape test results at the primary squeal noise frequency at 13 kHz. This measurement corresponds to the same brake configuration that was previously displayed in Figure II.3. The vertical axis in Figure II.4 is the amplitude of measured acceleration on the outer edge of the brake disk. As a result of the deflection shape test at 13 kHz, the primary vibration is observed in a Tangential direction (Figure II.4. b). There are also minor contributions in the axial direction (Figure II.4. a), and the radial contributions are negligible (Figure II.4. c).

The CAE unstable mode shapes shown in Figure II.3, at three different operating conditions of -15 C, 25 C, and 100 C temperatures at 10 bar pressure. Figure II.5. a (at -15 C), shows the primary in-plane vibration of the disk plates that indicates the Tangential mode of the disk. Figure II.5. c (at -15 C) displays out–of–plane displacement of the disk plates in the axial direction, indicating a Nodal Diameter (ND) mode of the rotor is being excited. In Figure II.5. b (at 25 C), the mode shape comprises both contributions of tangential and axial directions.

As a result, for this case study, by comparison of the unstable mode shapes from CAE (Figure II.4) to the deflection shape test (Figure II.5): Those mode shapes with tangential contributions agree to the test measurements. The corresponding operating conditions (temperature) are -15 C and 25 C. In contrast, the unstable mode with pure axial mode shape does not match the test result. The respective operating condition (temperature) for the false-positive instability point is at 100 C temperature. This circumstantial evaluation of system modes shapes at unstable datum validates if the CAE output is a real NVH concern in the physical system.

(a)   (b)   (c)
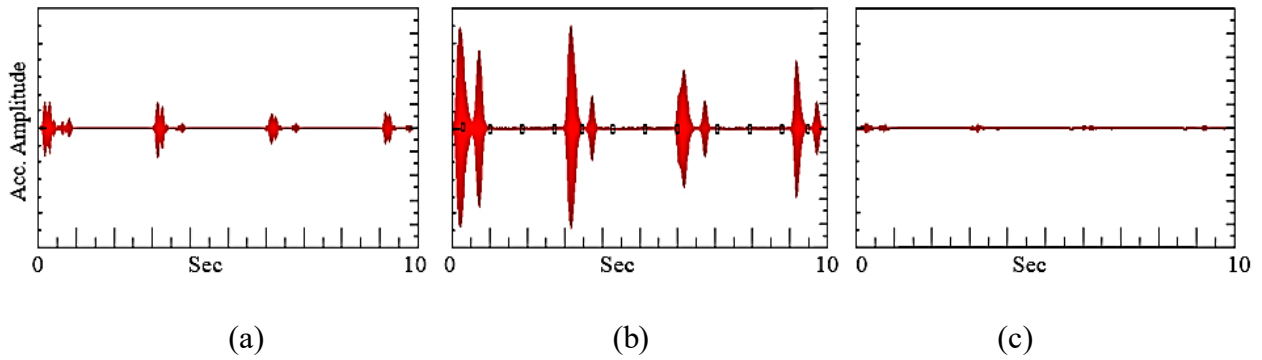
Figure II.4. Measured acceleration of the rotor in brake assembly at 13 kHz from the deflection shape test: (a) Axial direction; (b) Tangential direction; (c) Radial direction

(a)   (b)   (c)
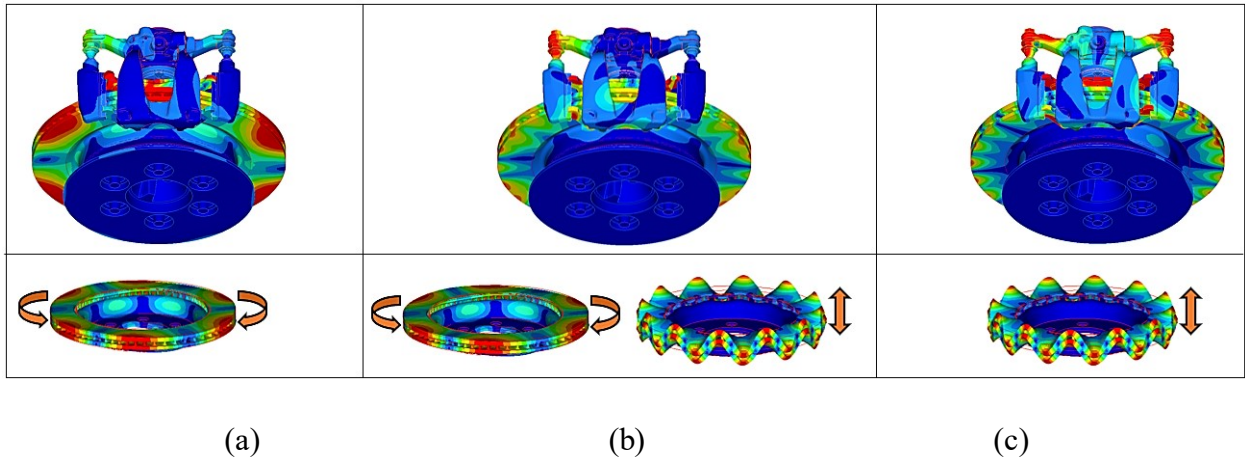
Figure II.5. CAE unstable mode shapes at 13 kHz and 10 bar pressure at (a) -15 C, (b) 25 C, and (c) 100 C

CHAPTER III

An ML-Enabled Metric to Predict Unstable NVH Modes Using Operating Conditions of Squeal Analysis

Motivation and Significance

Recent numerical approaches using the complex eigenvalue analysis for solving brake squeal; however, widely used in industry, it has a substantial disadvantage. When a high-fidelity model is required, the process is considerably slow and computationally expensive. This is due to broad ranges of operating conditions from the dynamometer test that induces extensive iterations in CAE to capture those conditions. In addition to the computational time for running such an analysis, the engineering time spent to validate the results is a more significant challenge. The validation process through the classic approach explained in the previous Chapter through unstable mode shape analysis is considerably time-consuming and costly.

In this research, an alternative technique offered to validate the correlation by matching the CAE operating conditions to the dyno test using a Machine Learning (ML) technique. This ML technique suggests selected operating conditions from the dyno test that need to be executing in CAE analysis. It uses an interpolation of the CAE data comparable with physical runs in the test. A surrogate model is generated from the operating conditions' statistical data by implementing this approach, which results from the correlation of CAE to baseline test. This model applies for further CAE iterations used for predicting noise and providing design recommendations. This approach illustrates a massive saving in computational time for CAE and the correlation process.

The Object Process Methodology (OPM) diagram for the current correlation technique is displayed in Figure III.1. The first step in the correlation process is capturing the material properties and the subsystems' resonance frequencies. The next step is correlating the noise frequencies, noise percentage, and dB level of the noise to the system level's instabilities. In the last step, the unstable mode shape is being examined between the two by conducting an operational deflection shape or laser vibrometer test using a 3D deflection comparison. It has been discussed that this validation process is a time-taking and costly procedure and requires expensive test facilities.

In Figure III.1. b, the proposed approach is shown using an innovative validation metric and imposing a Machine Learning (ML) model. The first three steps in the correlation process are the same as the classic methodology. The last step for validation at the system level is where a surrogate model is implemented to accelerate this process. The ML model distinguishes the true and false CAE data through operating condition profiles and verifies the correlations without running expensive tests such as the deflection shape test. This research work demonstrates the validation is achieved efficiently by matching the operating condition profiles. It enables an affordable and computationally reasonable technique that saves many engineering times.
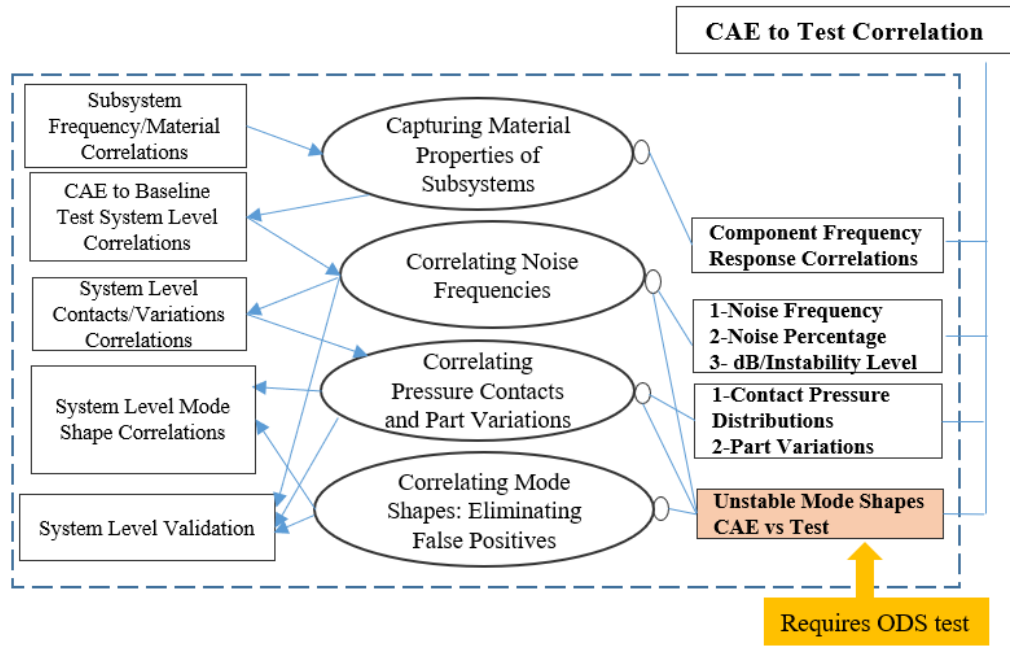
(a)
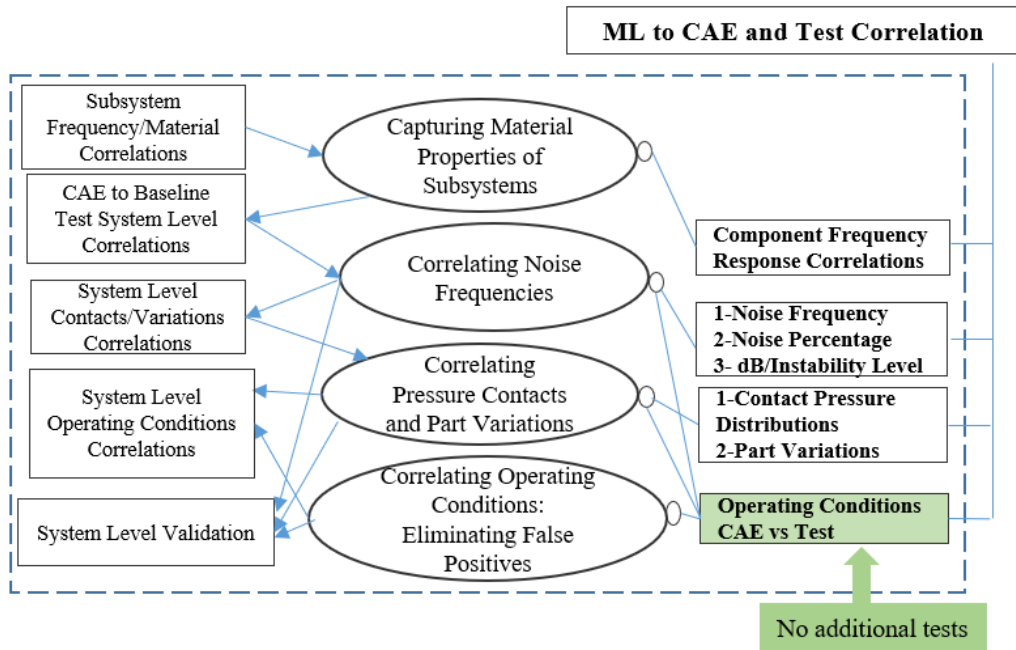
(b)

Figure III.1. Object Process Methodology (OPM) diagrams for: (a) the current correlation technique and (b) the proposed ML approaches

Nonlinearities of Analysis as a Result of Complex Operating Conditions

Nonlinearities in brake squeal analysis include material and geometrical nonlinearities. The geometrical nonliterary is due to a complex thermal and mechanical loading during braking operations. In the CEA approach, brake loading is simplified into three major static steps:

1. A thermal loading between pad and rotor due to energy dissipation induced by frictional force
2. A mechanical pressure loading that applies from caliper/piston assembly to brake pads
3. A steady-state rotation of the disk that determines the direction for frictional contact

As shown in Figure III.2, these static steps induce a contact interaction between the inboard and outboard pads to the brake rotor. These loading steps are modeled in ABAQUS to define frictional contact behavior. As the friction contribution increases, the system's adjacent modes at nearby frequencies could couple with each other and destabilize the system. The frictional model is described by contact surface interactions between rotor and pads and the friction coefficient. The friction coefficient is calculated based on the contact pressure, contact temperature, and the slip rate and predefined field variable as the formula in below:

(Equation III.1)

$$\mu = \mu(\dot{\gamma} eq, p, \theta, f)$$

Where $\dot{\gamma} eq$ is the equivalent slip rate, p is the contact pressure, θ is the average temperature at the contact point, and f is the predefined field variable.
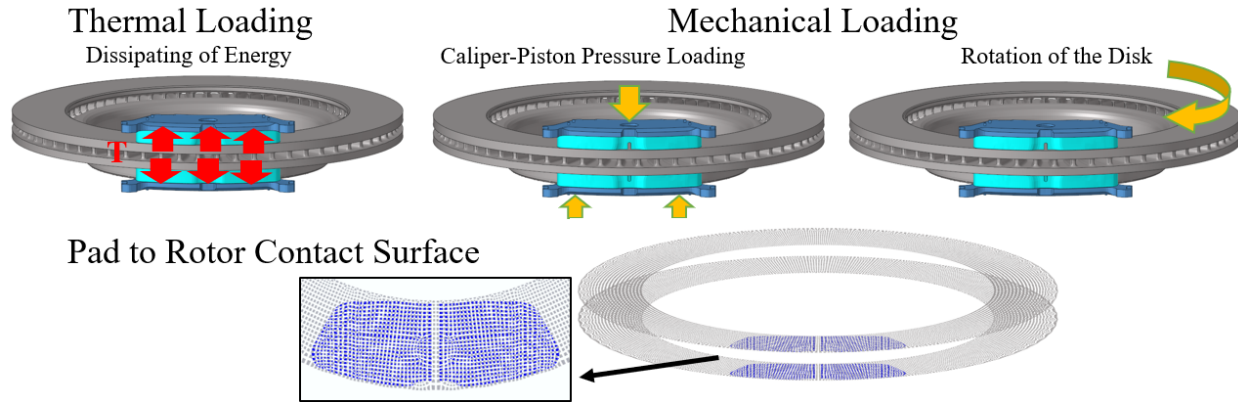
Figure III.2. Pad to rotor thermal and mechanical braking loading in numerical simulation

Simulating precise contact distribution is critical because it defines the interaction between the nodes in the pad and rotor contact surface in their engagement region. Also, it determines a precondition for eigenvalue calculations. This contact definition essentially reforms the system's un-symmetric stiffness matrix before conducting the eigenvalue and complex eigenvalue steps. Validating simulated contact distribution precision is challenging due to complex dynamic circumstances in braking operation. However, in this works, a static contact distribution is validated by comparing a scan of the physical assembly contact distribution in clamped loading from the dyno test and the CAE simulations. The discussion of contact correlations between the brake pads and the rotor is beyond this study's scope.

In the first loading step in CAE simulations, a combination of thermal and mechanical loading applies to the system to establish a contact pressure distribution pattern in the contact surface between the pad and the rotor. The thermal loading condition is determined by pad-to-rotor temperature and the braking's operation conditions (pressure and friction). This deforms the pad's surface and changes it into nonlinear (concave, convex, or complex) shapes. Through the thermal expansion equations, the phenomena regulate the pad lining's contact profile toward the disk.

Additionally, the mechanical loading is defined by pressure operation conditions through pressurizing piston and caliper during the braking operation. In below Figure III.3, a simulation for scaled deformations of the inboard and outboard pads under thermal and mechanical loading steps are displayed. Before applying the loading, the pad surface is perfectly flat. This figure shows the scaled deflections after applying a 10-bar pressure load through the piston and caliper at -15 C (Cold temp.), 25 C (Room temp.), and 100 C (Hot temp.). The deformed profile indicates a concave pad shape at the cold temperature and a convex pad shape at the high temperature.

This deflection in the pad surface is due to the component temperature dependency behavior regulated in the analysis with the corresponding thermal expansion. This enables for capturing of geometrical nonlinearities due to thermal effects. The thermal expansion model is included in material definitions. The thermal strains for the homogeneous solid continuum elements obtained according to the equation below:

(Equation III.2)

$$\epsilon^{th} = \alpha.\left(\theta, f_\beta\right).(\theta - \theta^0) - \alpha.\left(\theta^I, f_\beta^I\right).(\theta^I - \theta^0)$$

Where α is the thermal expansion coefficient; θ is the current temperature; θ^I is the initial temperature; f_β are the current values of the predefined field variables; f_β^I are the initial values of the field variables; and θ^0 is the reference temperature for the thermal expansion coefficient. The second term in the above equation represents the strain due to the difference between the initial temperature, θ^I, and the reference temperature, θ^0.
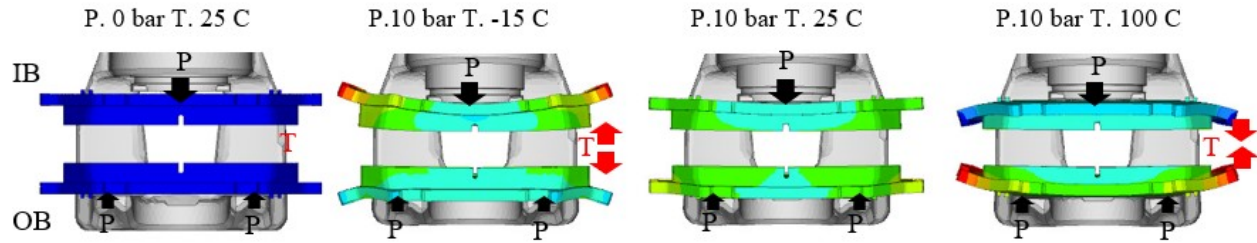
Figure III.3. CAE simulation of the inboard and outboard pad deformations under the combined thermal and mechanical loading

Modal characteristics of components are also temperature-dependent. Therefore, material elastic constants are considered temperature-dependent. Figure III.4 shows variations for the pad's first two eigenfrequencies and eigenmodes: the first bending mode (f_b) and the first torsional mode (f_t). This is through temperature variations between -15 C to 150 C. This data is collected from a Frequency Response Function (FRF) test for a production Ford vehicle brake pad in various temperatures. From this experimental data, variations are:

- 14% for the first bending mode eigenfrequency (fb)

- 17% for the first torsional mode eigenfrequency (ft).
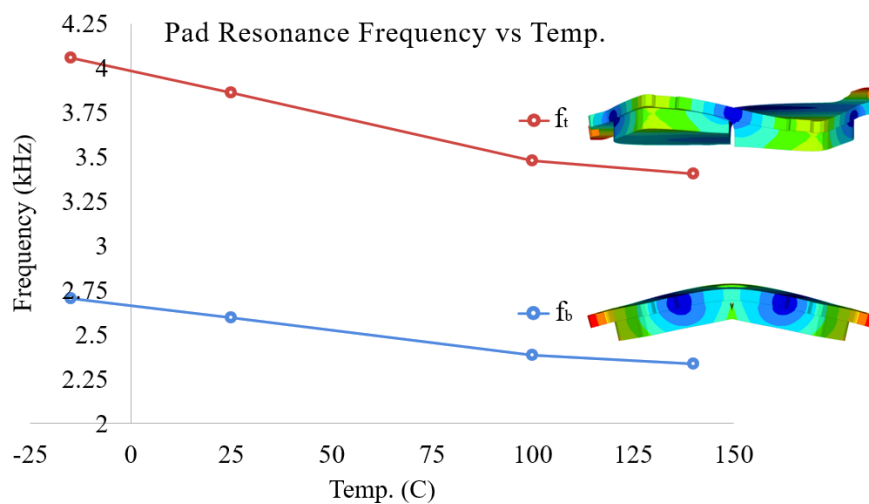
Figure III.4. Experimental data: eigenfrequencies vs temperature for the first bending mode (f_b) and the first torsional mode (f_t) in -15 C to 150 C (a production brake pad)

31

The range of the temperature variation in this brake squeal CAE analysis is from -15°C (cold brake) to 200°C (hot brake) to be proportional to the dyno test operating conditions. The variation range for pressure is from 0 bar to 30 bar based on the dyno test's operating condition range. The temperature and pressure conditions specified in the pressure loading step has a major role in defining the contact distribution pattern and nonlinearity of geometry. The disk's rotation direction induces asymmetrical contact distribution in a tangential direction in the rotational loading step. The pad leading side first contacts the rotor and forms a broader contact pressure area. Figure III.5 displays the contact pressure distributions for the inboard (IB) and the outboard (OB) pad surfaces to the rotor at -15 C (Cold temp.), 25 C (Room temp.), and 100 C (Hot temp.) for the pressure step (a) and the rotations step (b) from the CAE simulations. In the first static step (a), the pressure distribution from leading to the trailing is symmetric because there is no tangential activation. Applying the disk's rotational motion in the second step (b) enforces asymmetric distributions representing the brake's dynamic loading. By comparing the contact pressure contours in three various temperatures, the observations are:

- At the cold temperature, the distribution is more toward the center of the pad near the center slot (mainly for the inboard pad), and in hot temperature, it is more toward the pad's outer edges.

- The pressure concertation for the outboard pad is more toward the outer diameter (regarding rotor) than the inboard pad.

- The pad shape deformations can reasonably explain these contact conditions through the thermal variations.

(a) Pressure Step

(b) Rotation Step
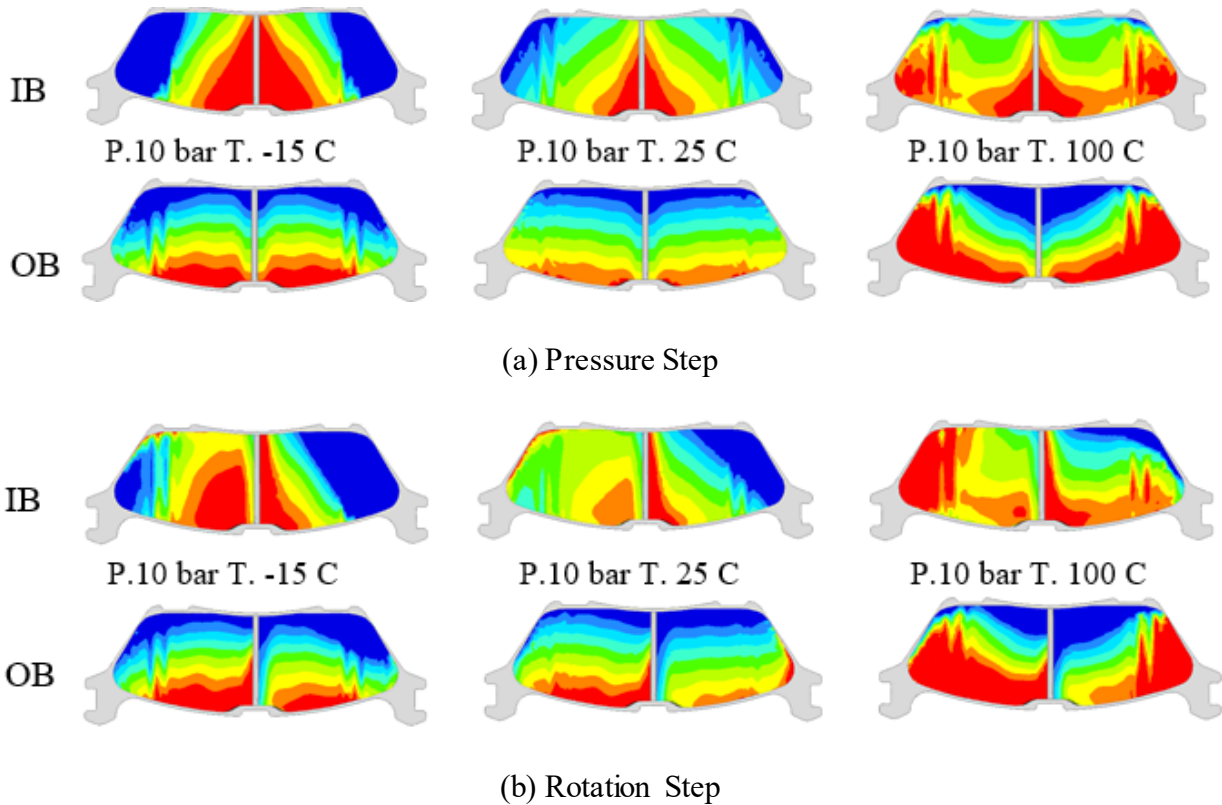
Figure III.5. Contact pressure distributions for the IB/OB pad surface to the rotor at -15 C (Cold temp.), 25 C (Room temp.), and 100 C (Hot temp.) simulated in CAE

Braking pressure levels also changes the pressure contours between the pad-to-rotor surfaces. The brake pressure level is determined by the pressure of fluid inside the piston and caliper housing, which applies a vertical load to the backing plates' surfaces and transfers the forces to the pads' surface toward the rotor. This pressure directly changes the contact pressure magnitude and the contact distribution of pad-to-rotor. Figure III.6 displays simulated contact pressure distributions for the inboard (IB) and the outboard (OB) pad surfaces to the rotor at 2 bar, 10 bar, and 30 bars at ambient temperature.
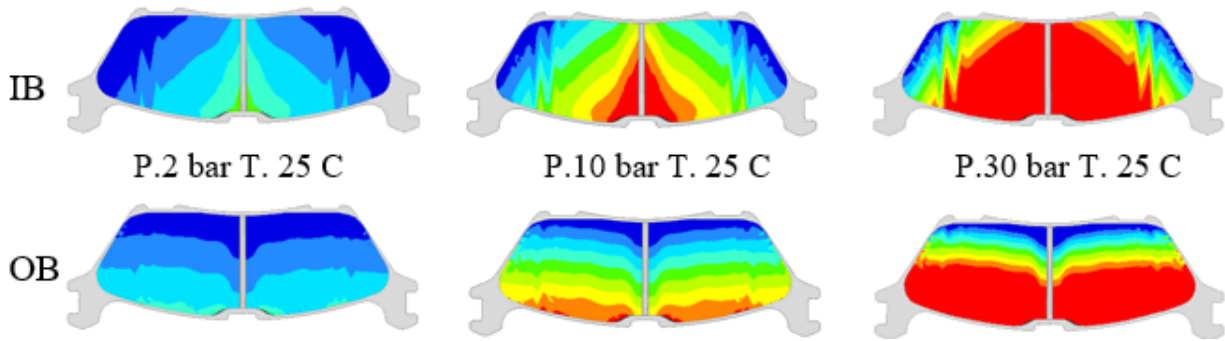
Figure III.6 Contact pressure distributions for the IB/OB pad surface to the rotor at 2 bar, 10 bar, and 30 bar at ambient temperature simulated in CAE

Another operating condition is directions of braking. In forward braking, as shown in Figure III.7, the initial contact point is the edge of the pad, where it is first in contact with the rotor. This region is where the contact pressure is mostly concentrated. As shown in the left figure, contact distribution in the tangential direction is more toward the leading side and the center for the inboard pad. For the outboard pad, however, the distribution is more shifted to the outer edge of the diameter (rotor), where the caliper finger applies pressure to the pad. Also, similar distribution is observed in the tangential direction for the leading to the trailing. In reverse braking, an opposite contact pattern is formed as simulated and displayed on the right side. These results also imply that the opposite braking direction will not impose an utterly different boundary condition that significantly impacts this case study.
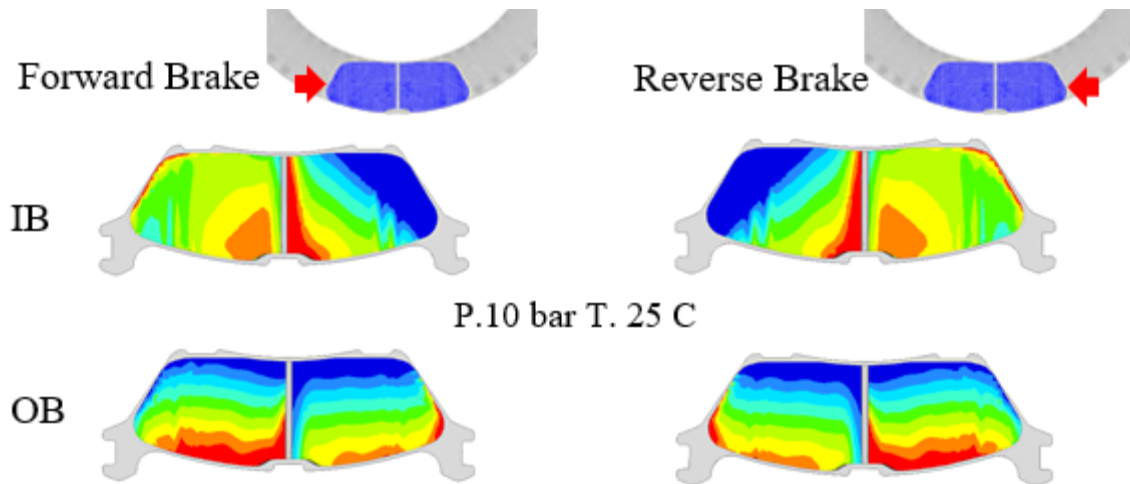
Figure III.7. Contact pressure distributions for the IB/OB pad surfaces in forward and reverse braking operation at 10 bar and ambient temperature simulated in CAE

A New Metric for Accelerated Unstable Modes Validations Using Operating Condition Profiles

A physical dyno or vehicle test for brake squeal noise provides information such as noise occurrences, including frequencies of the noises, dB level of the noises, and percentage of the noisy events. Besides, operating condition inputs such as temperatures, pressures, frictions, and rotor velocity for the noisy occurrences are recorded for each test. Material properties and frequency response function (FRF) of brake components are measured at the subsystem level before performing the test. Uncertainties are also studied in the analysis to include part characteristic variations and contact surface pressure distributions (for rotor-to-pads and caliper/piston-to-pads).

In CAE simulations using complex eigenvalue analysis, system instabilities are observed in an entire frequency spectrum. Every operating condition, including temperatures, pressures, and frictions, and the system's unstable mode shapes, are determined.

The numerical FE model is developed from brake component geometries and the CAD assemblies. The subsystems' correlations to the physical components are evaluated and verified, and then material properties are adjusted in the CAE. Variations and uncertainties could be considered depending on the fidelity of the model. Capturing the nonlinearities and variations in CAE requires typically further testing, such as scanning contact pressure distributions and physical parts. After the subsystems correlated from the virtual to the physical model, the system results must achieve a certain correlation level between the two systems. In the system-level analysis, the test's noise occurrences are compared to the CAE's instability results. Firstly, the frequencies of noise occurrences are cross-checked. Next, the noise dB level versus instability level and percentages of the noise occurrences versus the volume of instability occurrences are compared.

CAE to test correlation in brake squeal analysis is challenging because of the physical system's nonlinearities and uncertainties. The correlation process might need several trial and error and tedious efforts when there is a lack of data; if the correlation was not satisfactory, a CAE diagnosis is required to tune the model's parameters and achieve a better correlation. As described in the previous chapter, the CEA approach generates over-prediction, i.e., many more instabilities than the actual experimental results. Many of these instabilities are false positives that will not occur as real noise. This research proposes a new metric to address this discrepancy, which cross-checks the virtual model's operational condition profiles with the physical test.

Figure III.8 shows the probability density function of pressure and temperature operation conditions for the noise events from the baseline dyno result shown in the previous chapter in Figure II.3. In this case study, the density plots indicate that noisy occurrences mainly concentrate on medium pressure from 5 to 15 (bar). And for temperature, it primarily occurs in the cold regions

in -15 to 0 (Celsius). There are some occurrences in a mild to warm range between 25 to 75 (Celsius).
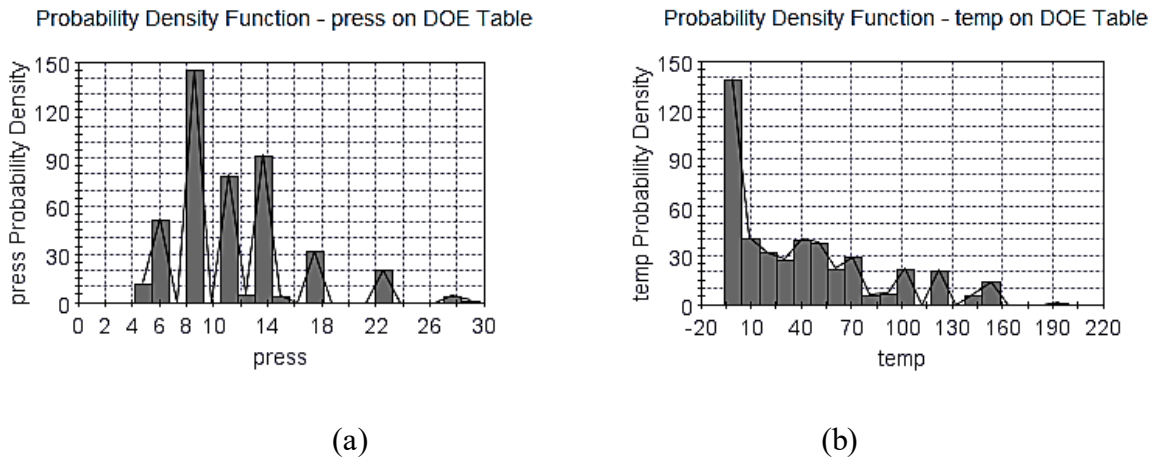
Figure III.8. Probability density function plots for (a) pressure and (b) temperature

Figure III.9 (a - d) displays the bivariate probability density function of temperature and pressure for four primary noise frequencies observed in this study. From the dyno test results, 13.1 kHz was detected as a dominant noise frequency compared to the overall noise events in the whole frequency range measured in 1 to 20 kHz. The probability density at 13.1 kHz (Figure III.9. d) indicates concentration in low to medium pressure range between 5 to 12 (bar) and cold-to-mild temperature from -15 to 50 (Celsius). Almost the same extent of pressure and temperature is observed at 2.2 kHz and 6.3 kHz (Figure III.9. a and c). Only at 3.2 kHz (Figure III.9. b), the range of the operating conditions observed is at medium-to-high pressure in 7 to 20 (bar) and room-to-high temperature in 25 to 120 (Celsius).
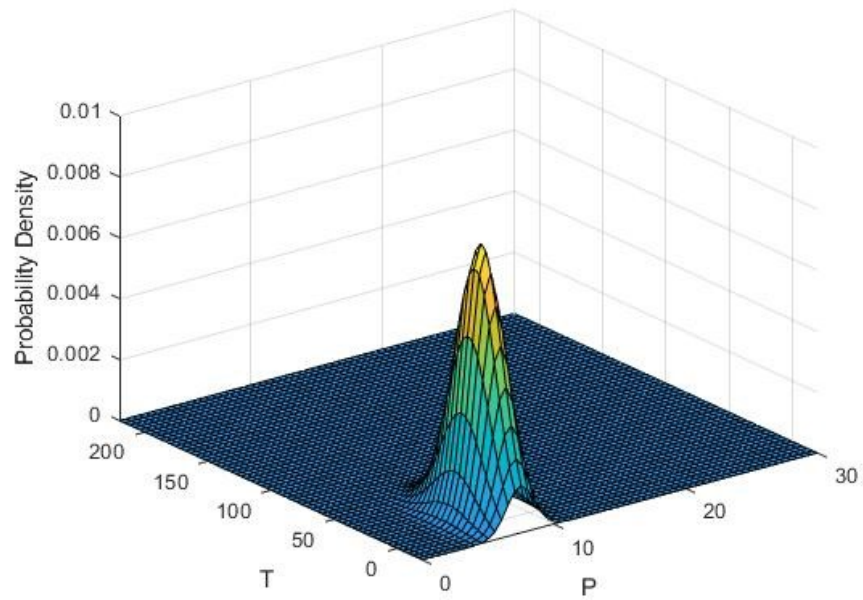
(a)
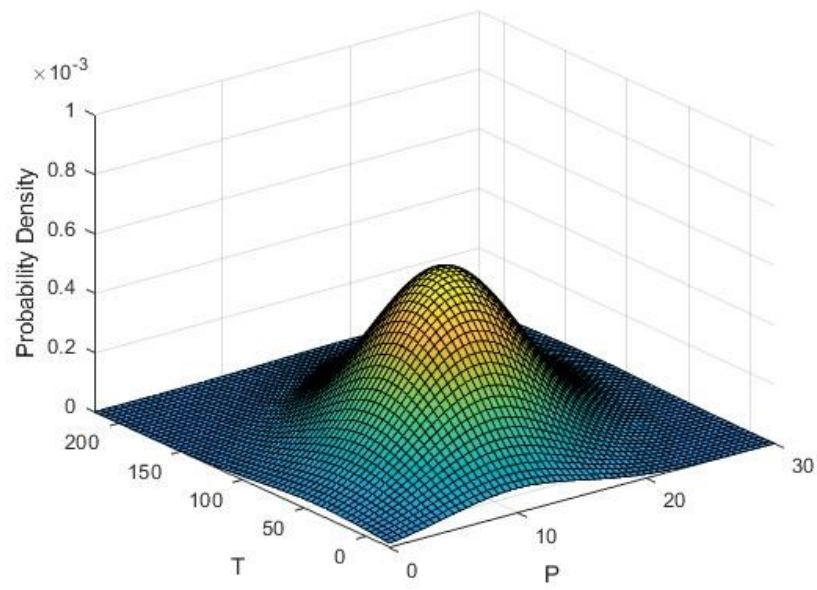
(b)
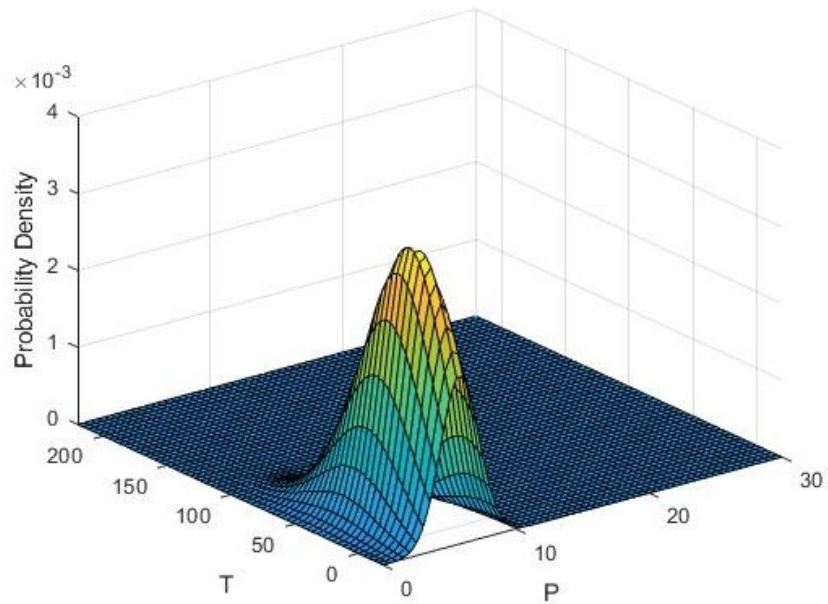
(c)
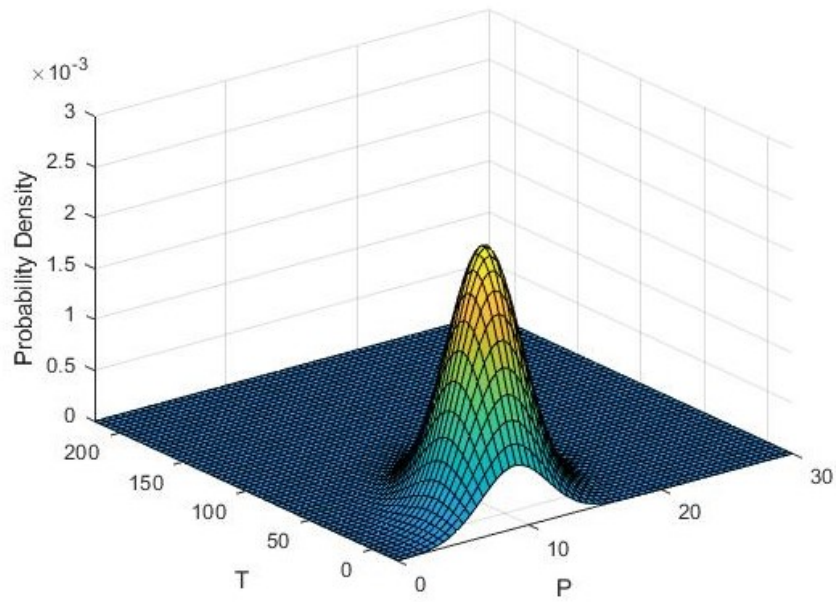
(d)

Figure III.9. Bivariate probability density function from dyno operating conditions (T: temperature and P: pressure) at: (a) 2.2 kHz, (b) 3.2 kHz, (c) 6.3 kHz and (d) 13.1 kHz noises

Given the relevance of the operating conditions in identifying unstable modes at target noise frequencies, the previous sections extensively discussed conceptual theory and complex physics. Equating the physical experiments' and the CAE simulations' operational condition profiles yields an additional layer of concrete data for validating and advancing the computational model. This leads to adding a physics-guided dimension for cross-checking of the computational model by adjusting its mechanistic features and parameters.

However, a proper statistical approach is required to quantify the two sources' correlation level, i.e., CAE and test, concerning their profiles of operational conditions. The probability intersection is one technique that the author believes it effectively addresses this matter. However, this requires sufficient data from both resources. Besides, a machine-learning algorithm has to be employed to adopt parameters and quantities from these two essentially different fashions.

Machine Learning Based Model to Accelerate CAE to Test Correlation

In order to implement the newly proposed metric based on operating conditions, a mathematical approach has to be implemented. One argument here is the number of operating conditions from the dyno test is significantly larger than the number of operating conditions in CAE. This will also depend on the fidelity of the virtual model and the computational resources available. The CAE instability results (previously shown in Figure II.3) ran over 96 different operating conditions, including pressures and temperate in forward and backward directions. With an average running time of 2 hours per each job on a supercomputer, the overall computational time was about 192 hours. Another argument is if the number of conditions is adequate to be comparable to the physical test; because the experimental test runs over thousands of operational

40

conditions (pressure, temperature) continuously. A key point here is an approach that has to be employed to minimize the computational time and still provides a quality correlation from the proposed metric. This approach requires developing a legitimate machine-learning model from the CAE results and interpolating the CAE data to be comparable to the experimental results.

Establishing an effective ML model requires a proper mathematical approach based on the input and output features and the dataset's characteristics. The ML model inputs are: 1- Pressure operating condition, 2- Temperature operating condition, and 3- Frequency of the instabilities from the CAE runs; and the output of the model is the projected instabilities. It is worth noting that the CAE's instability values are the absolute values of negative damping from the complex eigenvalue analysis. A schematic of the input and output features for the ML model is shown in Figure III.10 below.
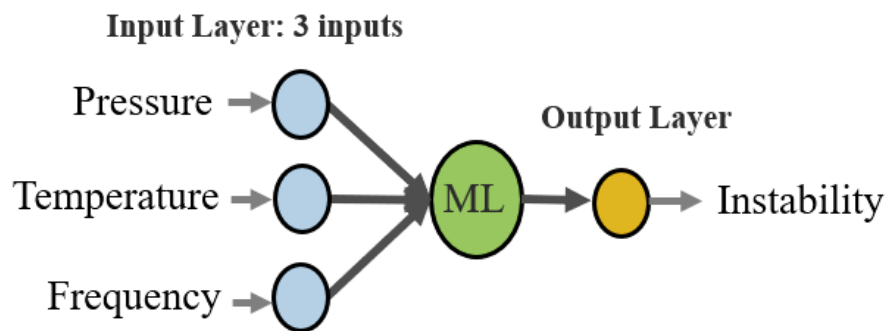
Figure III.10. Inputs and outputs for the proposed ML model

For preliminary analysis, a Gaussian process is developed to model the CAE instabilities as a function of the operating conditions at any frequency of interest. This enables generating millions of surrogate CAE simulations at different operating conditions with the need to run only a few actual CAE simulations. The Gaussian process model for the instability is explicitly written as:

(Equation III.3)

$$y(x) \sim \text{GP}\big(m(x), k(\theta, x, x')\big),$$

Where $m(x)$ is the basis function for the instability with inputs x, $k(\theta, x, x') = \text{cov}\big(y(x), y(x')\big)$ is the covariance function that correlates the pairwise instabilities for any two set of inputs x and x'. θ are the hyper-parameters of the covariance function.

To better elaborate the model in this section, denote $\{(x_i, y(x)); i = 1, \ldots, N\}$ for N experiments where the input x_i corresponds to the frequency, temperature, and pressure of test-case i, and the output $y(x_i)$ corresponds to the instability value (i.e., the negative of the complex part of the eigen-value) for test-case i.

The major advantage of considering the Gaussian process is to capture the complex correlations between the instabilities at different inputs (frequency, temperature, and pressure). Unlike the deterministic nonlinear models such as neural networks, the Gaussian process provides an entire distribution of estimations, which further quantifies the uncertainty in the estimation. The mean of the distribution is chosen as the point estimate, and its variance quantifies the uncertainty around the mean.

The name Gaussian process comes from its core assumption that any subset of capacity measurements follows a normal distribution. Consequently, the joint distribution of the instabilities from the available test-cases $y(x_1), y(x_2), \ldots, y(x_N)$, follows the multivariate normal distribution:

(Equation III.4)

$$y(X) = \begin{bmatrix} y(x_1) \\ y(x_2) \\ \vdots \\ y(x_N) \end{bmatrix} \sim N\left(\begin{bmatrix} m(x_1) \\ m(x_2) \\ \vdots \\ m(x_N) \end{bmatrix}, K(\theta, X, X) \right),$$

Where

(Equation III.5)

$$K(\boldsymbol{\theta}, X, X) = \begin{bmatrix} k(\boldsymbol{\theta}, x_1, x_1) & k(\boldsymbol{\theta}, x_1, x_2) & \dots & k(\boldsymbol{\theta}, x_1, x_N) \\ k(\boldsymbol{\theta}, x_2, x_1) & \ddots & \dots & k(\boldsymbol{\theta}, x_2, x_N) \\ \vdots & \vdots & \ddots & \vdots \\ k(\boldsymbol{\theta}, x_N, x_1) & k(\boldsymbol{\theta}, x_N, x_2) & \dots & k(\boldsymbol{\theta}, x_N, x_N) \end{bmatrix}$$

The covariance function depends on the domain knowledge and the number of available test-cases. With enough test-cases, the Gaussian kernel or the scaled Gaussian kernel captures the local trends in small time windows. For long-term cyclic trends, customized compound kernels can be developed that consists of seasonal kernels and/or seasonal mean functions are considered. For the available dataset in this case study, the scaled Gaussian kernel in (6) seems to be powerful.

(Equation III.6)

$$\text{cov}\big(y(\boldsymbol{x}), y(\boldsymbol{x}')\big) = k(\boldsymbol{x}, \boldsymbol{x}' | \theta_F, \theta_T, \theta_P, \theta_s)$$

$$= \theta_s^2 \exp\left[-\frac{1}{2}\left(\frac{f_x - f_{x'}}{\theta_f}\right)^2 - \frac{1}{2}\left(\frac{T_x - T_{x'}}{\theta_T}\right)^2 - \frac{1}{2}\left(\frac{P_x - P_{x'}}{\theta_P}\right)^2 \right]$$

Here, $\boldsymbol{x} = [f_x, T_x, P_x]$, f_x is the frequency for input $\boldsymbol{x}$, T_x is temperature for input $\boldsymbol{x}$, and P_x is the pressure for input $\boldsymbol{x}$.

The log-likelihood of the instabilities from the available CAE simulations is calculated as a function of the hyper-parameters $\boldsymbol{\theta}$. The data is imbalanced because only a limited number of instability points are recorded, and the rest are denoted to be stable. Therefore, an importance weighting technique is applied to address the imbalance problem. The hyper-parameters are then estimated by maximizing the log-likelihood of the pre-processed using quasi-newton optimization algorithms.

(Equation III.7)

$$\log\big(p(\boldsymbol{y}(X)|\boldsymbol{\theta})\big) =$$

$$-\frac{1}{2}\big(\boldsymbol{y}(X)-\boldsymbol{m}(X)\big)^{T}\boldsymbol{K}(\boldsymbol{\theta},\boldsymbol{X},\boldsymbol{X})^{-1}\big(\boldsymbol{y}(X)-\boldsymbol{m}(X)\big)-\frac{1}{2}\log\big(\det\big(\boldsymbol{K}(\boldsymbol{\theta},\boldsymbol{X},\boldsymbol{X})\big)\big)-\frac{N}{2}\log(2\pi)$$

Given the prior information $\boldsymbol{m}(X), \boldsymbol{y}(X), \boldsymbol{x}^{*}, \boldsymbol{X}, \boldsymbol{\theta}$, the only unknown is the instability $y(\boldsymbol{x}^{*})$ and its predictive posterior distribution is:

(Equation III.8)

$$\hat{y}(\boldsymbol{x}^{*})|\boldsymbol{m}(X), \boldsymbol{y}(X), \boldsymbol{x}^{*}, \boldsymbol{X}, \boldsymbol{\theta} \sim N\big(\hat{\mu}(\boldsymbol{x}^{*}), \hat{\sigma}^{2}(\boldsymbol{x}^{*})\big),$$

Where

(Equation III.9)

$$\hat{\mu}(\boldsymbol{x}^{*}) = \boldsymbol{k}(\boldsymbol{\theta}, \boldsymbol{x}^{*}, \boldsymbol{X})\boldsymbol{K}(\boldsymbol{\theta}, \boldsymbol{X}, \boldsymbol{X})^{-1}\big(\boldsymbol{y}(X)-\boldsymbol{m}(X)\big),$$

(Equation III.10)

$$\hat{\sigma}^{2}(\boldsymbol{x}^{*}) = k(\boldsymbol{\theta}, \boldsymbol{x}^{*}, \boldsymbol{x}^{*}) - \boldsymbol{k}(\boldsymbol{\theta}, \boldsymbol{x}^{*}, \boldsymbol{X})\boldsymbol{K}(\boldsymbol{\theta}, \boldsymbol{X}, \boldsymbol{X})^{-1}\boldsymbol{k}(\boldsymbol{\theta}, \boldsymbol{X}, \boldsymbol{x}^{*})$$

And

(Equation III.11)

$$\boldsymbol{k}(\boldsymbol{\theta}, \boldsymbol{x}^{*}, \boldsymbol{X}) = [k(\boldsymbol{\theta}, \boldsymbol{x}^{*}, \boldsymbol{x}_{1}) \quad ... \quad k(\boldsymbol{\theta}, \boldsymbol{x}^{*}, \boldsymbol{x}_{N})]$$

A structured flowchart in Figure III.11 describes the proposed correlation and validation procedure between the virtual model and the physical test. The validation process is through the proposed metric using operational conditions profiles (Temperature and Pressure). Contributions for this research are 1- To present and 2- Establish this metric, and 3- Implement a machine-learning (ML) model that efficiently fits the CAE model and improves the correlation.

The correlation is calibrated when the fitted ML model agrees to the test results; Otherwise, a diagnosis is required for tuning the parameters of the ML model; or the CAE model needs to be further improved for higher accuracy. The data set used in this case study is based on the CAE, which is composed of instability data at 96 different operating conditions (pressure and

temperature data) that match frequencies of the noisy occurrences in the dyno test at approximately 2, 3, 6, and 13 kHz. The collected database contains 9328 samples of CAE instability points.
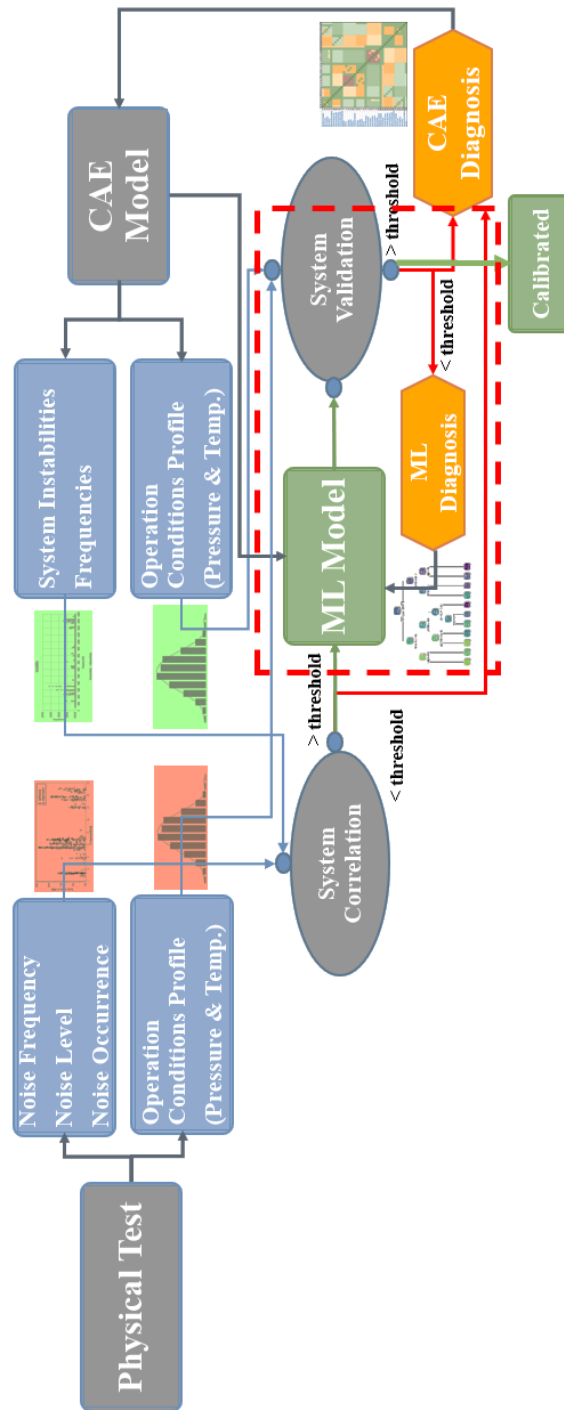
Figure III.11. A structured flowchart for the proposed correlation and validation process between the virtual model and the physical test

Results and Discussion

The implemented ML model developed over 96 operating condition runs from CAE results (previously shown in Figure II.3) employing a Gaussian process. Figure III.12 below shows the instability plot resulting from the ML model compared to the CAE instabilities through the whole range of the frequency. The ML model is based on both false and true positive data points from the CAE output. As observed from the plot below, more than one trend of unstable data points exists around the noise frequencies: 2.2, 3.2, 6.3, and 13.1 kHz, which were observed from the corresponding dyno plot in Figure II.3.
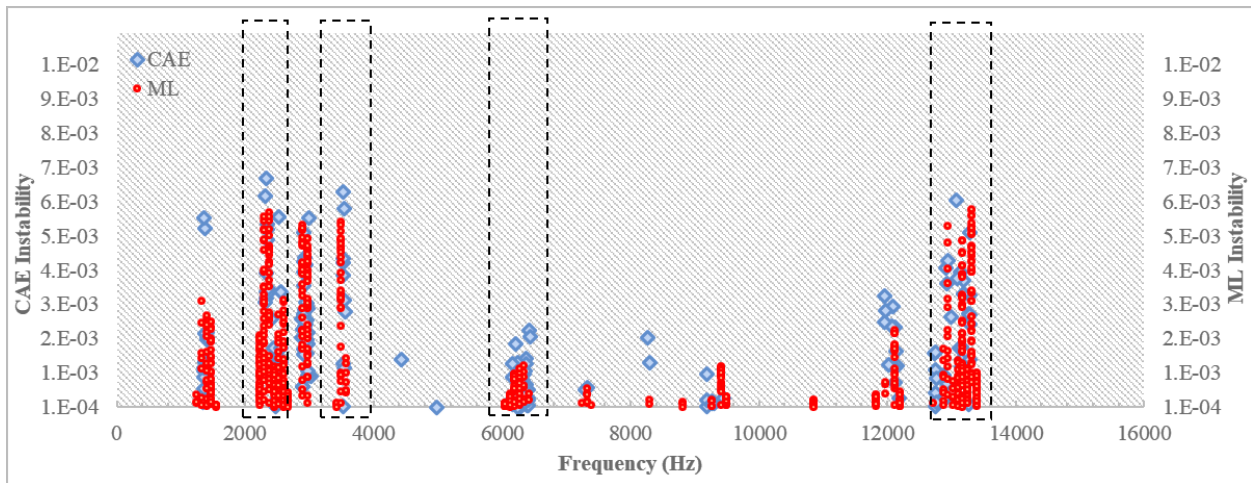
Figure III.12. Comparison of CAE and ML model outputs for the entire frequency spectrum

The noise at 13 kHz frequency is the primary target noise observed in the dyno test. This result elaborates the target noise frequency for discussion and proving the concept. The goal here is to identify the trend of instability data points as the real highest potential noise in the physical system. Substantially, data from the ML model and dyno are compared using distribution plots. The noisy stops in the dyno test occur in the frequency range between 13150 Hz to 13200Hz. On the other hand, in the ML model, the first frequency peak is at 12950 Hz and the second and third

ones are at 13150 and 13350 kHz. However, it is worth noting that the CAE and corresponding ML model may not be accurate enough to predict the target frequency within the 3% range.

Applying the proposed metric using the ML-based model presented here, validation of real instability peaks is by assessing the correlation of the operating conditions. Figure III.13. (a-c) shows a 3-dimensional probability density outputs from the ML model's operating condition at 12950 Hz, 13150 Hz, and 13350 Hz. Here the P indicates pressure (bar), and the T is for temperature (Celsius), and the vertical axis is the probability density magnitude. These plots indicate the range and the density of distributions through temperature and pressure. From the density plots, at 12950 Hz (Figure III.13. a), the temperature range is mainly at the warm and hot range, and the pressure range is from 3 to 12 bar. However, the density plots at 13150 Hz (Figure III.13. b) and 13350 Hz (Figure III.13. c) imply the temperature range from cold to mild, and the pressure is in the mid-range from 7 to 15 (bar). From the dyno probability density plot at the 13 kHz noise previously displayed in Figure III.9. b, the range of the operating conditions reported in low to medium range from 7 to 12 (bar) pressure and cold to mild temperature. Finally, from this observation and correlating the density plots of the ML model and dyno test, the real instabilities are determined at 13150 Hz and 13350 Hz. The operating condition metric provides validation for the CAE model and identifies the true unstable modes through this assessment. There are two main advantages to this validation approach. Firstly, it doesn't require additional physical tests such as laser deflection shape test; Secondly, it is computationally affordable and doesn't require computing and visualizing modes shapes. However, the computational model's fidelity has a significant role in this process, and it must be capable of predicting temperature-dependent behavior for materials and nonlinear frictional contacts. The other metric used to validate the real instability peak is by exploring the unstable mode shapes and comparing it to the deflection shape

47

test described in the earlier sections. The drawback of the latter approach is that it requires high-cost physical experiments from one side, and on the other side, it requires slow and expensive postprocessing.
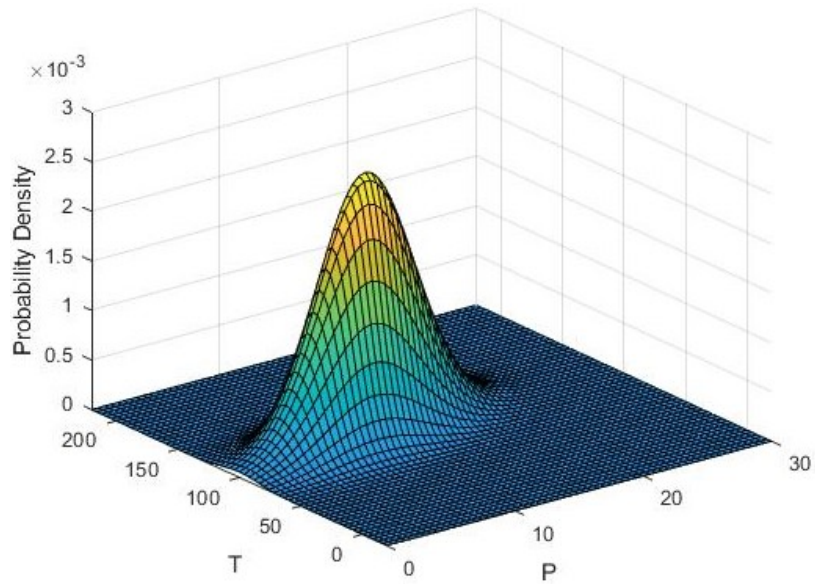
(a)
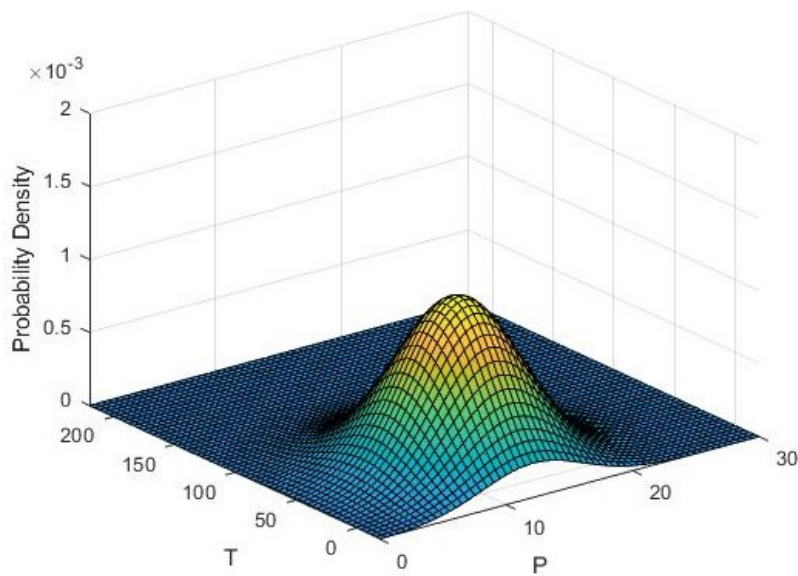
(b)
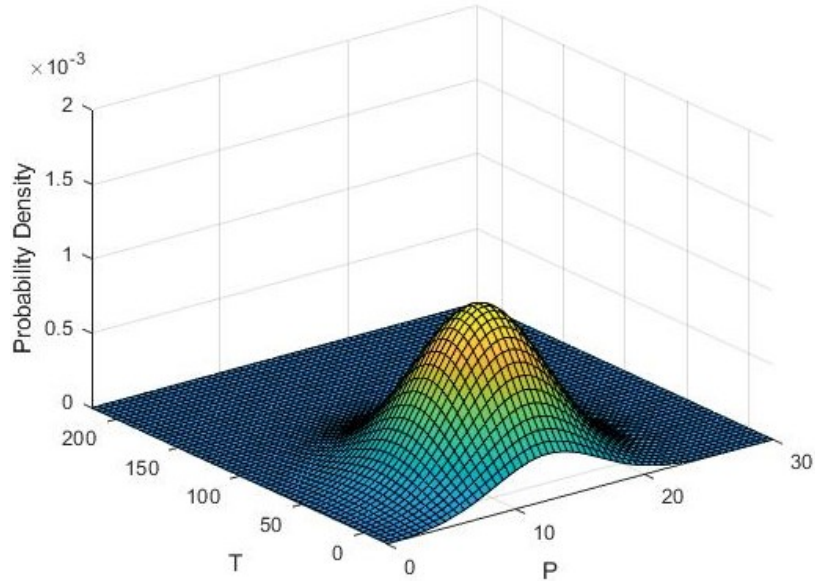
(c)

Figure III.13. ML model operating conditions distributions (temperature and pressure) at:
(a) 12950 Hz, (b) 13150 Hz and (c) 13350 Hz

Brake NVH is a challenging area due to brake subsystems' nonlinear interactions and complex thermal and mechanical loading cycles in a wide range of frequency and operating conditions. Numerical approaches currently exist to simulate brake squeal, but they are computationally expensive and highly challenging for predicting the phenomena. A high-fidelity numerical model (captures features such as variations and contact nonlinearities) still requires additional physical experiments to identify real instabilities from false positives. For this validation, an expensive approach is currently used, that is described in this work. This method requires extra computational time to evaluate the unstable complex mode shapes, and an operational deflection shape analysis is needed from the physical system.

In this work, an alternative time-efficient approach for validation is presented by introducing a statistical technique and assessing operating conditions' correlation. The proposed

49

scheme introduces a metric that explores the correlation of operating condition distributions from the virtual and physical models. It eliminates the necessity for additional physical testing, such as the deflection shape test, to verify the correlation.

Statistical techniques incorporated with the numerical models have been increasingly developed and employed to improve virtual models' efficiency. These collaborations and interactions brought new challenges to the research areas in Computer Aided-Engineering. To present a robust solution, the statistical models must adequately fit the output of computer experiments, which requires an accurate estimation of uncertainties in physical experiments and incorporating acceptable physics-based criterion.

This research presented an algorithm is to implement a Machine Learned model based on CAE data for brake squeal analysis to simulate the dyno test results. It discussed the challenges to incorporate the presented ML model into such a complex problem. Further, the author proposed a new validation process. It described extensively the learning approach and equations employed to construct the surrogate models. Particularly, it showed the ML-based model presented in this study reduced the computational cost significantly by exploring the whole design space from operating conditions and skipping over duplicative iterations.

Even though only one primary noise frequency was evaluated and validated in this study, a full spectrum of noise frequencies can be examined using the same method. Moreover, a higher-dimension model can be used in future studies, including additional parameters for operating conditions such as friction values, material properties, and geometrical variations.

CHAPTER IV

A Deep Learning Technique to Predict Brake Pad NVH Modal Characteristics Based on Physical Properties

Introduction to Brake Pad NVH Modal Characteristics and Physical Properties

Brake in automotive converts kinetic energy into thermal energy by engaging pad's stationary friction surface to rotating brake disk to develop a frictional torque to stop the motion that happens through a complex loading process with thermo-mechanical divergences and many uncertainties. Brake pads must sustain a high frictional contact in a sudden temperature shift due to a dissipation of energy and exhibit steady performance [Kinkaid and O'Reilly (2003)]. The pad component comprises frictional additives, fillers, binders, and reinforcement fibers [Eriksson (1999)]. Pad lining is generally classified into low metallic, semi-metallic, and non-asbestos organic (NAO) concerning its ingredients [Alemani et al. (2017) and Sanders (2003)]. Brake pad material has a complex formulation and consists of multiple compounds, including metal fiber, organic/inorganic fiber, barite, several other additives, graphite, and phenol-formaldehyde resin binder [Sasaki et al. (2003)]. Physical properties of pads and their friction material formulation play a key role in braking systems' performance and controlling friction, wear, and NVH characteristics [Sriwiboon et al. (2018)].

According to many works of literature [Papinniemi (2002), Kinkaid and O'Reilly (2003), Chen (2007), Dunlap (2008) and Dai and Lim (2008)], brake NVH has been studied in a frequency domain and, in general, classified in 3 categories by the range of the frequency. Low-frequency

noise and vibration occur in 0 to 1000 Hz, which has multiple categories for several types of noise and vibration. From 1000 to 3000 Hz, low-frequency squeal noise occurs more related to brake components. A high-frequency squeal noise occurs in about 3000 to 16,000 Hz range, which is dominantly influenced by the brake pad's dynamic characteristics and interactions with the brake disk. Squeal Noise is a major NVH problem and considered a highly disturbing noise, causing customer complaints and dissatisfaction. It is a failure for the quality of products [Kinkaid et al. (2005), Hoffmann and Gaul (2008), Mottershead (1998), Papinniemi (2002), and Kinkaid and O'Reilly (2003)].

Several studies and analyses [Earles and Soar (1971), Earles and Lee (1976), Earles (1977), Earles and Badi (1984) and Earles and Chambers (1987)] indicated that brake squeal is due to a mode-coupling induced by the neighboring of two or more natural frequencies of the brake system, which is mainly governed by the pads and rotor's natural frequency. Pad is the excitation source that significantly influences brake vibration and noise performance [Massi et al. (2006)]. Several analytical models and analyses developed in the past to explore the brake squeal phenomenon and the potential solution to that. These analyses demonstrated that the influence of the frictional contact surface is highly significant, as well as modal eigenfrequencies and eigenmodes [Ouyang et al. (2005), Oura et al. (2008) and Giannini and Sestieri (2006)]. Elaborated nonlinear finite element models of brake squeal demonstrated that a correlation is achievable when the nonlinear effects are captured and incorporated into the system model and an accurate material properties identification conducted and validated by physical tests [Mottershead (1995), Nack and Joshi (1995) and Nack (2000)]. It is demonstrated in multiple research studies that there is an interrelationship between components modal characteristics and system modal response [Ouyang

et al. (2003), Matsuzaki and Izumihara (1993), Chen et al. (2002), Chen et al. (2003), Bae and Wickert (2000) and Brunel and Dufrénoy (2008)].

The investigation to find an explicit correlation between pad friction material parameters and the NVH performance is still under review and research in the automotive industry. A statistical study [Wegmann and Dohle (2015)] performed by conducting physical measurements on a relatively large number of pad samples to collect data on pad NVH related features such as K3 Compressibility, Specific compress, Eigenfrequency, Dynamic Material Properties (DMP), and pad geometry. This study aimed to investigate a correlation between the measured pad parameter and the noise performance on dyno tests. A wide range of pads from a serial production is used to minimize influences of part variations. This study has not found any resealable correlation between the measured pad parameters and the noise results. [Wegmann and Dohle (2015), Steege et al. (2008), and Wegmann et al. (2010)]. However, other researches indicated NVH sensitivity to parameters such as compressibility and eigenfrequency [Lee and Cho et al. (2017), Nonaka (2012) and Oura et al. (2009) and Yuhas and Yamane (2010)].

Within this research scope, NVH modal characteristics of brake pads are described by eigenfrequencies and eigenmodes in the frequency range of 500 Hz to 16 kHz according to the standard test SAE J2598 (2012). The main objective of this test is to establish a standardized and repeatable method for measuring the Frequency Response Function (FRF) of disc brake pads. This data used as a multifold index for the component modal map, benchmark, and dynamic stiffness identification.

The test setup is shown in Figure IV.1, according to the standard procedure. The FRF measurements are performed by striking one end of the pad using an impact hammer and recording

the response using an accelerometer on the pad's farthest edges in multiple locations to ensure that

the first three natural frequencies and responses are measured precisely.
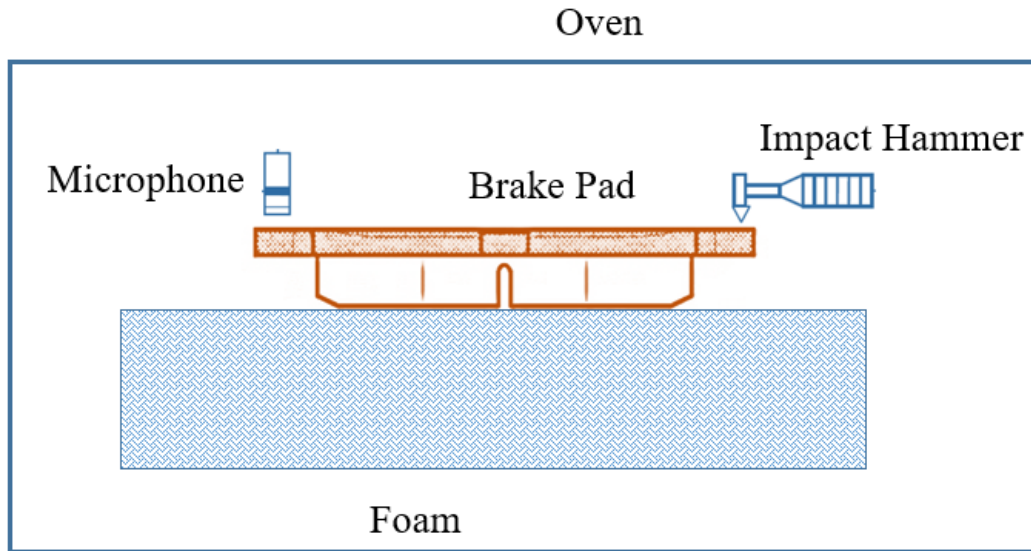
Figure IV.1. Test set up for standard test SAE J2598 (2012) to measure brake pad frequency response function

The CAE model set up for simulating the brake pad's frequency response function is shown

in Figure IV.2. The simulation is performed using a mode superposition method. Modal analysis

of the component is performed in the first step, which provides natural frequencies and vibration

modes in a free-free boundary condition. In the second step, by applying a unit harmonic loading

condition: (F_y=1 N) as the source of the excitation at the furthest end of the pad backing plate, the

response is measured in terms of acceleration (A_y) at the other end. Steady-state dynamic analysis

is conducted in the finite element model using Fourier transform, and therefore the modal

coordinates are extracted in the frequency domain. FRF is calculated as a complex function, with

real and imaginary parts that can be interpreted in terms of magnitude and phase angle. The

response magnitude and phase angle are determined by the components' physical features,

including geometry and material properties (defined by elastic constants and density). One critical

element that crucially controls the magnitude of the response is material damping. Damping can be included in the analysis as structural damping, classic Rayleigh damping, or frequency-dependent viscous damping. In this research work, the Rayleigh damping approach is used for the numerical model, which contains a mass-proportional and a stiffness-proportional value for the entire frequency range. Other researches [Esgandari et al. (2013), Liu and Gorman (1995), and Giannini and Meerbergen (2008)] discussed the advantage of using Rayleigh damping in brake NVH analysis and have shown results that improved the correlation of CAE to the experimental tests using this damping definition.
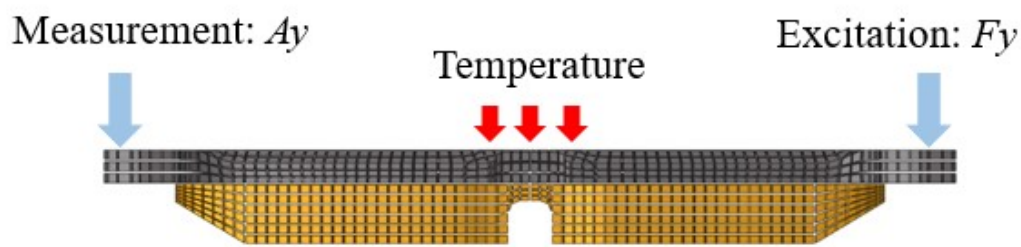
Figure IV.2. CAE model set up for simulating brake pad frequency response function

This research conducts an experimental work by correlating the frequency response function from the finite element model to the physical test for a production brake pad from a Ford vehicle. The experimental test is based on the SAE J2598 (2012) standard procedure. The material and geometry parameters adjusted precisely to ensure the preconditions for the correlation exists. The numerical model is based on a steady-state dynamic analysis in CAE using a high-resolution finite element model. Comparing the CAE results to the physical test is shown in Figure IV.3 (Left), which demonstrates the correlation of the brake pad's frequency response function at 1st and 2nd normal modes between the CAE simulation vs. the Test measurements at ambient

55

condition. The 1st peak corresponds to the pad's 1st normal mode, and the 2nd peak corresponds to the 2nd normal mode. However, SAE J2598 suggests the measurement of the first three eigenmodes. In this case study, the 3rd eigenmode is a higher order of 2nd eigenmode, and their characteristics correlate with each other. Therefore, it is dismissed from this study. For this experiment, the 1st and 2nd normal modes were observed as bending and torsional modes, respectively, as illustrated in Figure IV.3 (right). However, pad eigenmodes' order depends on the pad's structure and the backing plate geometry and could vary for the other geometries.
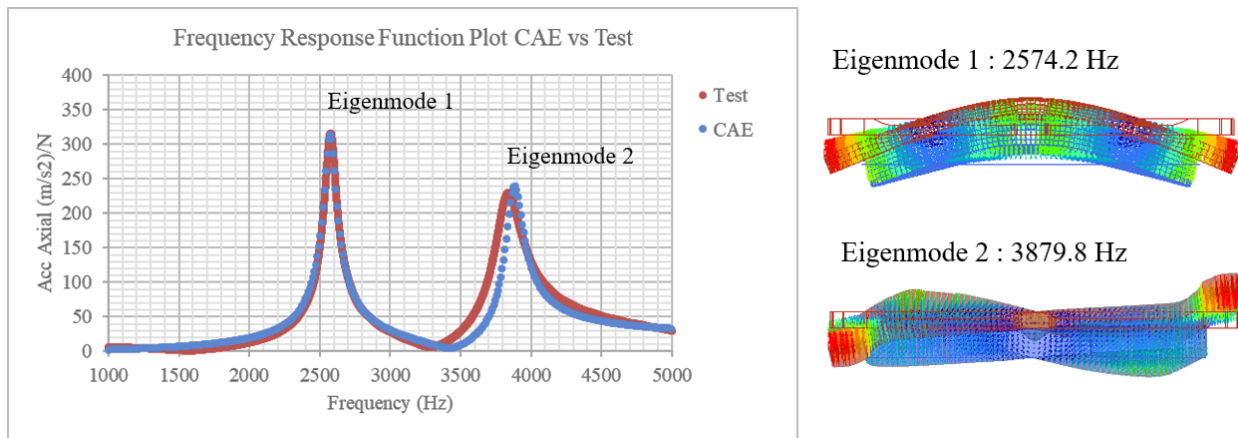
Figure IV.3. Frequency response function correlation for the brake pad's 1st and 2nd normal modes: CAE simulation vs Test measurements

Physical tests and FEA simulation are currently used for studying component modal characteristics. Although FEA simulation could precisely match up with test in component level yet, it relies on physical inspection of parts and tuning of materials and geometries to capture variations to provide comparable results with test experiments. This process requires several hours of engineering and computational time for a single analysis. However, the numerical FEA model can offer many iterative designs concerning its input parameters to discover the optimum design for an NVH resolution. These data are practically beneficial to find a pattern between critical physical parameters and overall performance.

56

The contribution of this chapter is to propose and implement an alternative technique utilizing data from numerical simulations to predict NVH modal characteristics of the brake pad (i.e., the frequency response function) concerning its physical features. The pad's physical features comprise pad friction material and geometry parameters and environmental and operating conditions:

1. This method eliminates urgency to additional physical testing and numerical model at a component level analysis.

2. It accelerates the process of design and development.

3. It facilitates the perception of the brake pad's physical features and their synchronous interactions and their implications on NVH response.

4. It will allow an efficient way of redesigning products by circumventing the redundancy in design exploration.

(1) Eliminating additional tests and numerical simulations	(4) Efficient designing that minimizes redundancy
(2) Accelerating process of design and developments	(3) Perception of important features, their interactions and implications
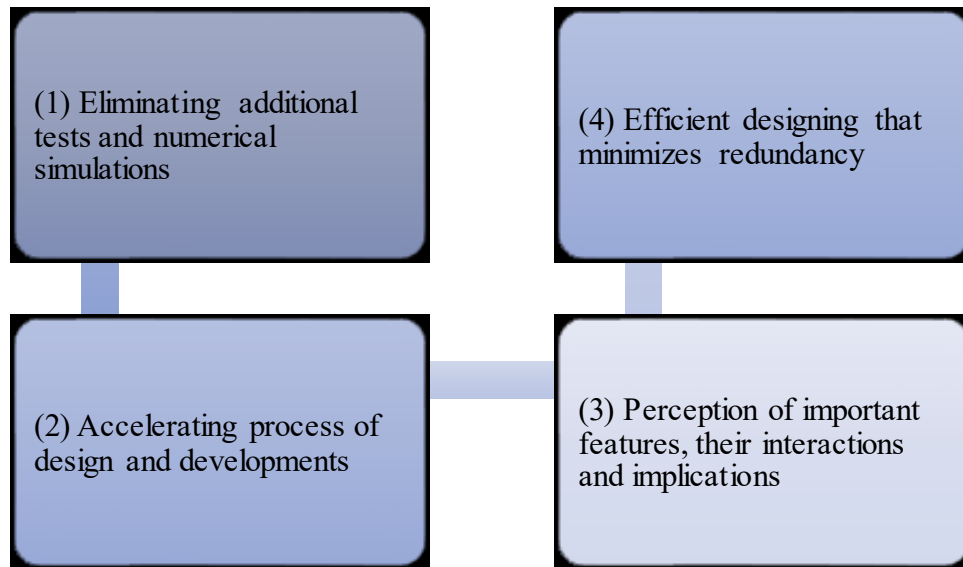
Figure IV.4. This chapter research contribution

Brake Pad Material Features

Brake pad friction material is transversely isotropic property. Transversely isotropic property is a specific subclass of orthotropic property that is characterized by a plane of isotropy at every point in the material. As shown in Figure IV.5, for transversely isotropic material, physical properties are symmetric about a normal axis for the isotropy plane. Infinite planes of symmetry could exist within this transverse plane; however, the material properties remain the same in all directions. In contrast, an orthotropic material has three orthogonal planes of symmetry, where properties differ along each of three principal directions [Schreiber et al. (1973), Every (1993), Brecht (2003), Hashmi (2014) and Aboudi (2013)].
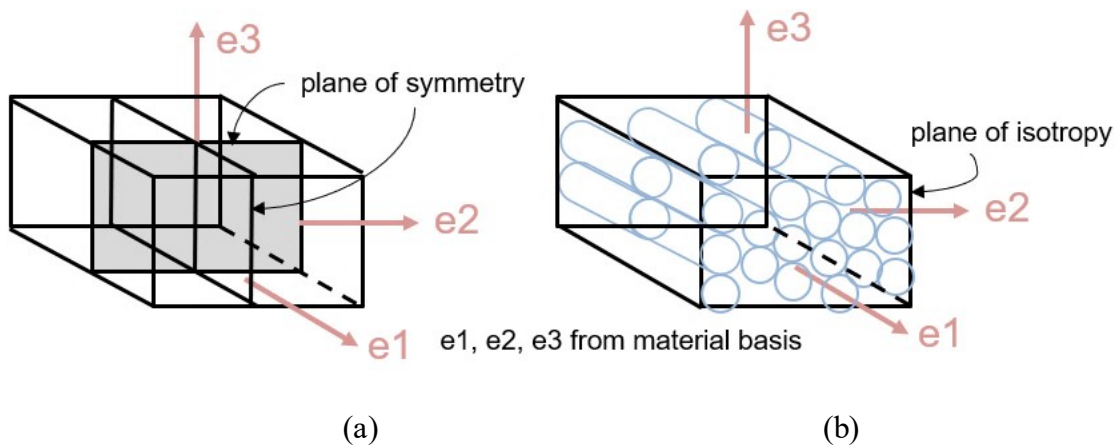
Figure IV.5. Material properties structure: Orthotropic (a) vs Transversely isotropic (b)

Orthotropic material has the compliance tensor given by [Hashmi (2014), Aboudi (2013)]:

(Equation IV.1)

$$\begin{Bmatrix} \varepsilon_{11} \\ \varepsilon_{22} \\ \varepsilon_{33} \\ \gamma_{12} \\ \gamma_{13} \\ \gamma_{23} \end{Bmatrix} = \begin{bmatrix} \dfrac{1}{E_1} & -\dfrac{v_{21}}{E_2} & -\dfrac{v_{31}}{E_3} & 0 & 0 & 0 \\ -\dfrac{v_{12}}{E_1} & \dfrac{1}{E_2} & -\dfrac{v_{32}}{E_3} & 0 & 0 & 0 \\ -\dfrac{v_{13}}{E_1} & -\dfrac{v_{23}}{E_2} & \dfrac{1}{E_3} & 0 & 0 & 0 \\ 0 & 0 & 0 & \dfrac{1}{G_{13}} & 0 & 0 \\ 0 & 0 & 0 & 0 & \dfrac{1}{G_{13}} & 0 \\ 0 & 0 & 0 & 0 & 0 & \dfrac{1}{G_{23}} \end{bmatrix} \begin{Bmatrix} \sigma_{11} \\ \sigma_{22} \\ \sigma_{33} \\ \sigma_{12} \\ \sigma_{13} \\ \sigma_{23} \end{Bmatrix}$$

Assuming the 1–2 plane to be the plane of isotropy at every point, transverse isotropy requires that: $E_1 = E_2 = E_p$, $E_3 = E_{op}$, $v_{31} = v_{32} = v_{op-p}$, $v_{13} = v_{23} = v_{p-op}$, and $G_{13} = G_{23} = G_{op}$. Where p and op stand for "in-plane" and "out-of-plane," respectively. Thus, while v_{op-p} has the physical interpretation of the Poisson's ratio that characterizes the strain in the plane of isotropy resulting from stress normal to it, v_{p-op} characterizes the transverse strain in the direction normal to the plane of isotropy resulting from stress in the plane of isotropy. In general, the quantities v_{op-p} and v_{p-op} are not equal and are related by:

(Equation IV.2)

$$\frac{v_{op-p}}{E_{op}} = \frac{v_{p-op}}{E_p}$$

And Gp is related to Ep and υp as following:

(Equation IV.3)

$$G_p = \frac{E_p}{2(1 + v_p)}$$

In the transversely isotropic materials, the stability relations for orthotropic elasticity simplify to:

(Equation IV.4)

$$E_p, E_{op}, E_p, G_{op} > 0, \ |v_p| < 1, |v_{p-op}| < \left(\frac{E_p}{E_{op}}\right)^{0.5}, |v_{tp}| < \left(\frac{E_{op}}{E_p}\right)^{0.5},$$

$$1 - v_p^2 - 2.v_{op-p}.v_{p-op} - 2.v_p.v_{op-p}.v_{p-op} > 0.$$

The characterization of a transversely isotropic material consists of finding the five independent elastic constants of the compliance tensor as of: E_p, v_{p-op}, v_{op-p}, v_p and G_{op}. Pad friction material in the brake squeal instability analysis is defined based on the five elastic constants in the compliance tensor, damping values, and the density of the pad listed in Table IV.1.

The pad material elastic constants and density are generally extracted from two experimental techniques: one technique is the Ultrasonic wave test, commonly called ETEK measurements. ETEK is a high-frequency testing technique in the MHz range, and it has been used widely in the automotive industry to measure the in-plane and out-of-plane elastic properties of the anisotropic friction material [Strickland and Yuhas (1996) and Sanders and Yuhas (2007)]. This test is known as SAE J2725 (2009) test, which specifies a standard method for measuring elastic constants in friction materials by employing a precise ultrasonic velocity measurement. Another technique uses Frequency Response Function (FRF) outputs from the SAE J2598 (2012) test and a reverse engineering technique to optimize the elastic constants of the pad friction's material properties conducted through a CAE DOE material optimization. The latter approach requires both FRF test data, numerical simulation, and DOE optimization for tuning the material features. But the advantage of this technique is it provides the dynamic properties in the given frequency range of the measurement, i.e., 500 Hz to 16 kHz, which is the same range as the problem for brake NVH. However, the ETEK measurement technique determines the properties in the MHz range. Studies have shown the dynamic properties of the pad materials are considerably varies in kHz and MHz range [Lou et al. (2007), Malmassari et al. (2015), and Augsburg et al. (2003)]. Therefore, the second technique is employed here as a more reliable technique for the material properties definition.

As discussed earlier, in this research, the classic Rayleigh damping approach is used for brake pad material, and it is described by only two variables of mass-proportional value D_m and stiffness-proportional value D_s as shown below [Geradin (1993), Newland (1989)]:

(Equation IV.5)

$$[C] = D_m [M] + D_s [K]$$

Where [M] is the component Mass matrix, [C] is the component Damping matrix, and [K] is the component Stiffness matrix.

Likewise, the mass proportional and the stiffness-proportional parameters D_m and D_s are connected to the critical damping ratio ξ_i and the natural frequency ω_i of the component at vibration mode i and is defined by Equation IV.6. The values for critical damping ratio ξ_i and the natural frequency ω_i at every eigenmodes of the component can be directly calculated from the output of the component FRF test SAE J2598 (2012) [Liu and Gorman (1995) and Meerbergen (2008)].

(Equation IV.6)

$$\xi_i = \frac{1}{2} (\frac{D_m}{\omega_i} + D_s. \omega_i)$$

Table IV.1. Brake pad friction material parameters

Variable	Variable Description
E_p	Young's modulus in the plane of isotropy
E_{op}	Young's modulus in the direction of normal to the plane of isotropy
v_p	Poisson's ratio
v_{p-op}	Poisson's ratio that characterizes the transverse strain in the direction normal to the plane of isotropy
G_{op}	Shear modulus in the direction normal to the plane of isotropy
D_m	Mass Proportional Damping value
D_s	Stiffness Proportional Damping value
Ro	Density of the pad friction

In this research work, for pad friction material, four features studied as the dominant features that influence the Frequency Response Function of the pad in Free-Free boundary condition as defined in SAE J2598 (2012). These four material features are: 1-E_p: Young's modulus in the plane of isotropy, 2- G_{op}: Shear modulus in the direction normal to the plane of isotropy, 3- D_m: Mass Proportional Damping value, and 4- D_s: Stiffness Proportional Damping value.

An initial sensitivity analysis is conducted in CAE by running a dynamic steady-state analysis using the pad FEA model by varying the material parameters (- and +) 25%, to observe the significance of these features on the frequency response function. The result is shown in Figure IV.6-9. For the material elastic constants, it is observed that the in-plane Young's modulus "Ep" and the out-of-plane shear modulus "Gop" are crucial for shifting the first two natural frequencies

of the pad. However, the in-plane Young's modulus "Ep" dominantly impacted the 1st eigenmode, which is the bending mode of the pad and out-of-plane shear modulus "Gop" mostly affected the 2nd eigenmode, which is the torsional mode of the pad.

Whereas, the material mass proportional damping "Dm" and stiffness proportional damping "Ds", mostly influences the magnitude of the response and do not have a major influence on the natural frequencies as a result shown in Figure IV.8 and Figure IV.9. Another observation is, the mass proportional variable "Dm" has a significant impact on the 1st peak (lower frequency), and the stiffness proportional "Ds" has a larger effect on the 2nd peak (higher frequency).
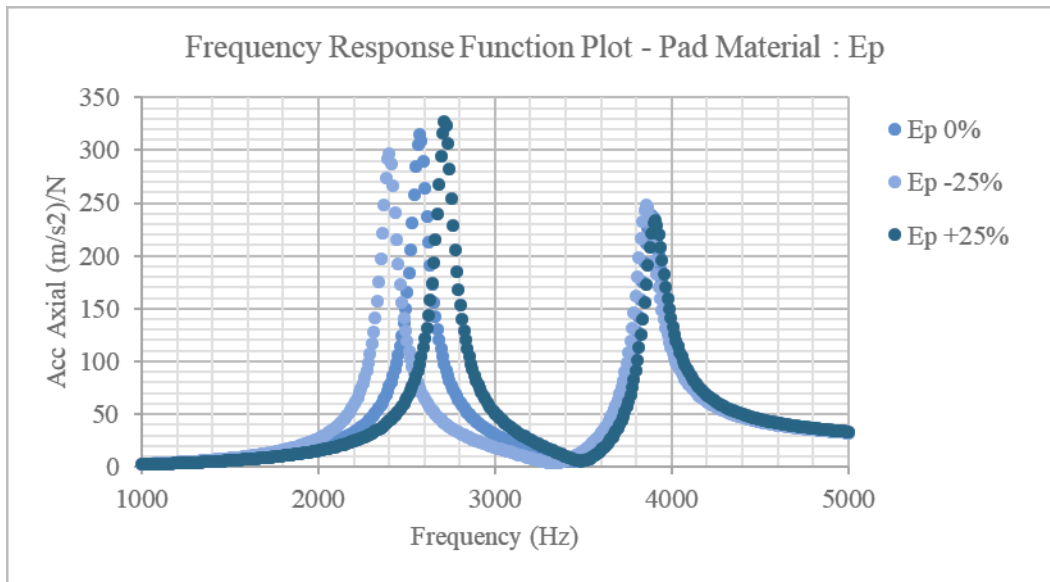
Figure IV.6. Brake pad Frequency Response Function plot for material in-plane Young's modulus "Ep" at 0%, -25% and +25% variation
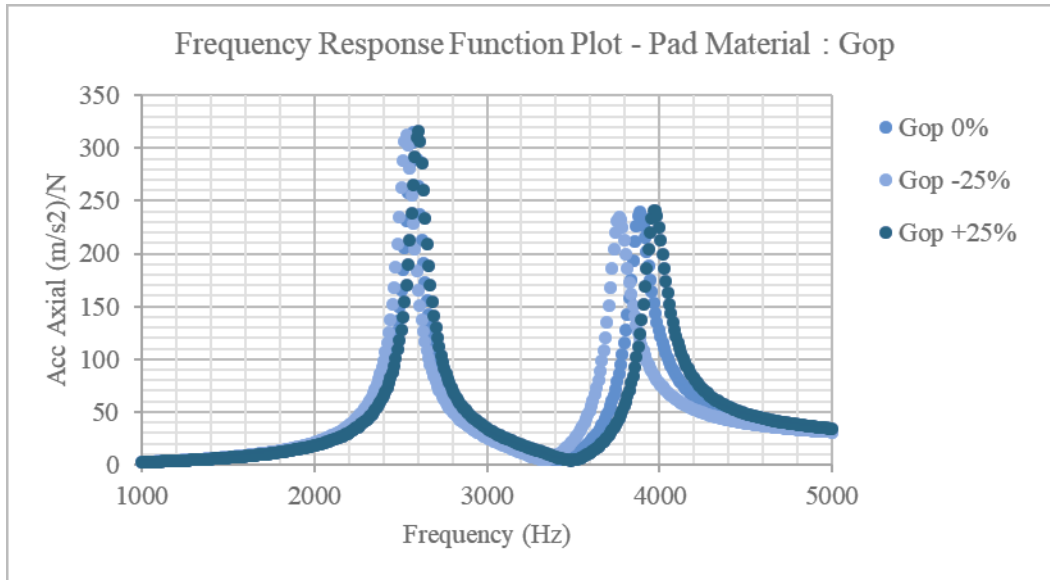
Figure IV.7. Brake pad Frequency Response Function plot for material out-of-plane shear modulus "Gop" at 0%, -25% and +25% variation
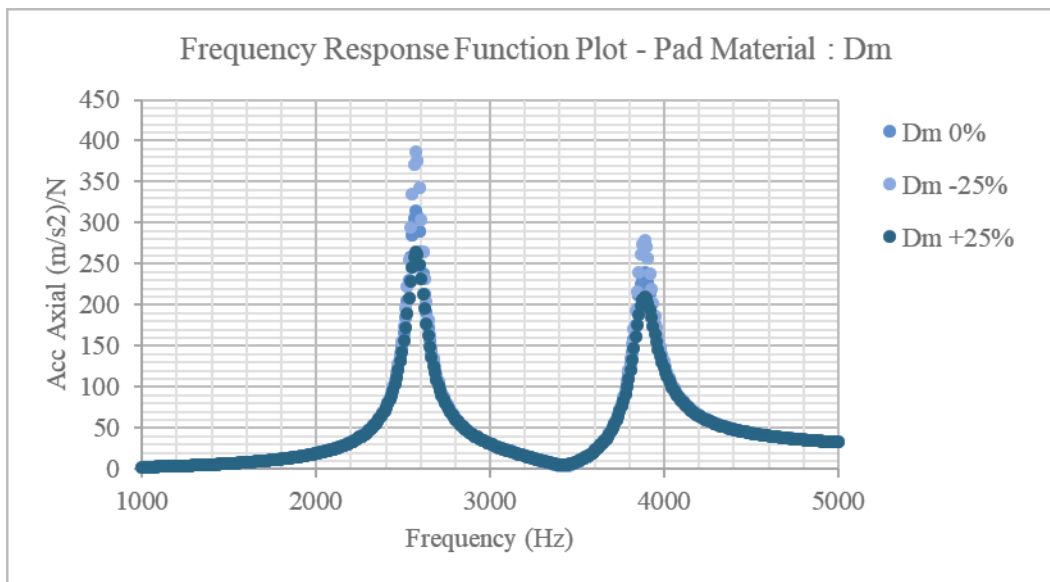
Figure IV.8. Brake pad Frequency Response Function plot for material mass proportional damping "Dm" at 0%, -25% and +25% variation
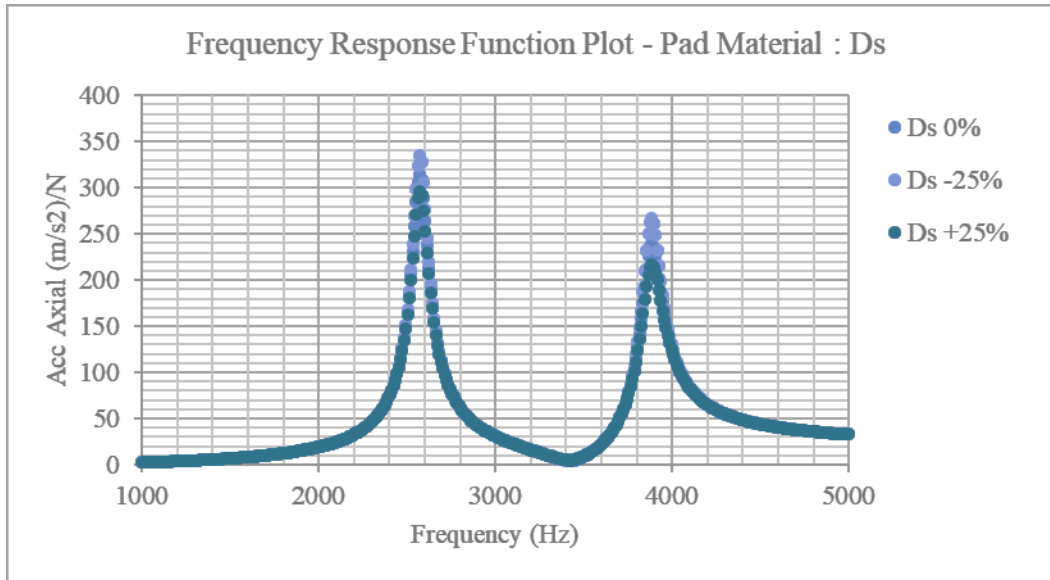
Figure IV.9. Brake pad Frequency Response Function plot for material stiffness proportional damping "Ds" at 0%, -25% and +25% variation

Brake Pad Geometry Features

Brake pad geometry is a significant effective squeal counter-measurement, especially for noise solution at higher frequencies. Pad geometry is defined by chamfer and slot geometries and the backing plate's shape, and the overall thickness. The last two are constrained by manufacturing tooling and are customarily considered inflexible. One remedy to address the brake noise is to explore the brake pad locations with the high vibration amplitudes and then optimize the chamfer or slot shape as an effective solution to mitigate the high vibration area. [Sasaki et al. (2003) and Alemani et al. (2017)] Pad geometry has multiple effects regarding changing the overall NVH performance of the brake. One impact is changing the pressure contact distribution and, as a result, the source of excitation. Contact distribution defines the contact area between rotor and pads, and it changes the vibration energy transfer. [Kinkaid et al. (2002), Liu et al. (2006)]. The other substantial effect is changing the modal frequency of the component as well as the system [Chen

(2009), Denys et al. (2006), Chen and McKillip (2008)]. Another theory describes the significance of modal frequency shifts that changes the vibration energy transfer between rotor and pads. It contends there are eigenmodes and eigenfrequencies in the first place that would reinforce the effective energy transfer. The latter implies the significance of pad geometry on the modal frequency of brake and its impact on system NVH behavior (Kinkaid et al. (2002), Liu et al. (2006), and Fieldhouse (1999)].

The two major pad geometry features are chamfer and slot (Figure IV.10). Brake pad slots mainly designed to allow air/gas flows from the pad during the braking operation also provide stress relief to avoid cracks in the material. The other purpose of the slot is to shift the brake pad's natural frequency and control the bending and torsional modes. Chamfers can considerably move the contacts between the pad and the rotor. They are mainly designed to remove high vibration regions around the brake pad's contact edges where it interacts with the disk. These two features affect the brake vibration and squeal noise predominantly. Pad shapes are studied in brake NVH development using optimization techniques to solve high-frequency noise with a cost-efficient change. Pad geometry could have sophisticated shapes that comprise chamfers and slots in different angles and form and size, including asymmetric leading to trailing design. Nonetheless, this study limited geometry complexity with only two prominent features captured for proof of the concept and the pad design assumed to be symmetric.
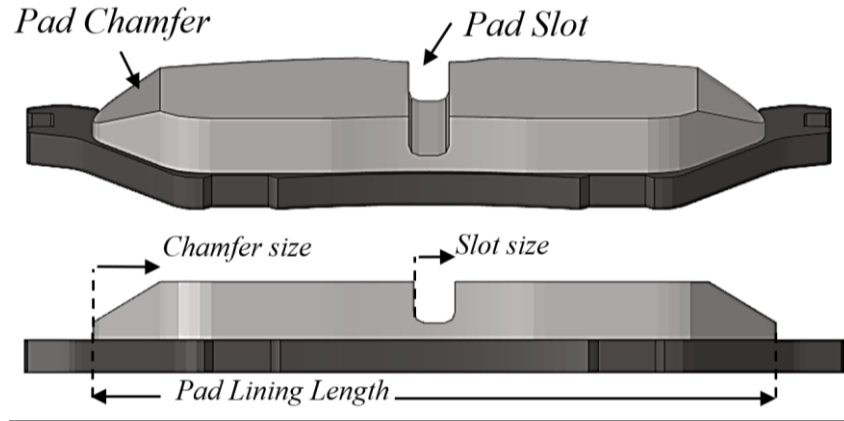
Figure IV.10 Brake pad geometry features: slot and chamfer

The pad shape geometry iterations that have been studied are shown in Table IV.2. In this work, Chamfer features are considered a simple straight cut with one dimension varies in a range of 0 to 20 % of the pad's overall lining length. Additionally, the slot size (defined by its width) changes in a range of 0 to 6 % of the lining length. Both variables are predefined in the vertical direction (i.e., depth is fixed), and they are only flexible in the tangential direction. More complex pad geometry features can be studied in future analysis and be considered as new variables.

Table IV.2. Pad geometry features: "Chamfer" and "Slot" Size to the pad lining length %

Iterations	Chamfer Size %	Slot Size %
1	0 %	0 %
2	0 %	3 %
3	0 %	6 %
4	10 %	0 %
5	10 %	3 %
6	10 %	6 %
7	20 %	0 %
8	20 %	3 %
9	20 %	6 %

A sensitivity analysis is conducted for the pad geometry in CAE, varying the chamfer and slot sizes variables from 0 to the higher bounds of their range to observe its impact on the frequency response function. As shown in Figure IV.11, these results demonstrate that adding the slot impacts the first two natural frequencies of the pad (both bending and torsional modes) and also the response's magnitude. Changing the slot size from 3% to 6% is still considerable but not as effective as including/excluding this feature. On the other side, as displayed in Figure IV.12, adding the chamfer hints no significant impact on either the natural frequencies or response; Plus, changing the chamfer from 10% to 20% (of pad length) shows a minor influence on the FRF plot at either peak.
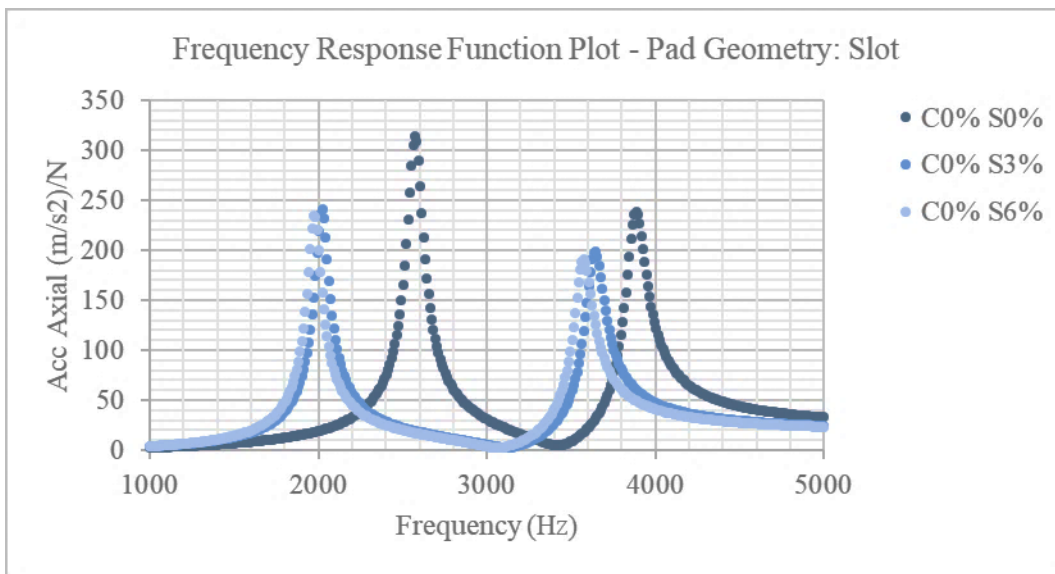
Figure IV.11. Brake pad Frequency Response Function plot for "Slot size" of 0%, 3% and 6% of the length of the pad
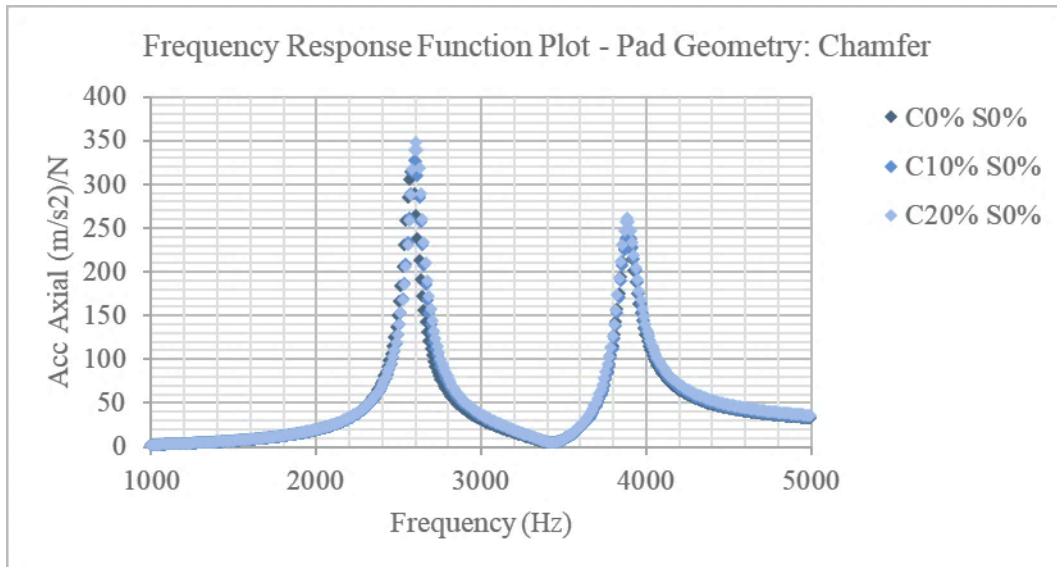
Figure IV.12. Brake pad Frequency Response Function plot for "Chamfer size" of 0%, 10% and 20% of the length of the pad

Enviormental and Operating Condition Factors

The brake's environmental and operating conditions are unique. Humidity and temperature are two primary environmental conditions. There have been numerous research developments to enhance cold and humidity test procedures to predict brake NVH better, explicitly addressing the squealing noise. Cold room chassis dynamometer is one of the most common recent tests to capture humidity and temperature impacts on noise performance. This test procedure is updated in the latest SAE standard procedure, J2521 (2005), to scrutinize environmental factors and uncertainties. Due to the braking phenomena' frictional nature, the dissipation of energy from the frictional contact surface between rotor and pada raises the pad's surface temperature up to 300 degrees Celsius. Several studies revealed the static and dynamic properties of brake pad dramatically changes in this thermal cycle [Nishioka et al. (2006), Miyoshi and Buckley (1984), Kobayashi and Odani (1997), Odani et al. (1999), Eriksson et al. (2001), Chen (2002) and Koch et al. (2006)].

69

Research studies also indicated that the pad's contact surface characteristics, including surface to surface frictional behavior, are extremely affected by temperature varying due to the thermal expansion effect [Chen (2009)].

The fugitive nature of squeal makes it highly challenging to recreate the test rig's noise events and study the root cause. Uncertainties exist due to the variations in the operating conditions and the environmental factors that considerably influences both component and system behaviors. The main operational conditions and environmental factors considered in brake NVH analysis are temperatures, humidity, braking pressure, rotor velocity, and coefficient of friction [Kinkaid and O'Reilly (2003), Ichiba and Nagasawa (1993) and Chen et al. (2007)]. However, the last two features do not apply in the component level analysis. Besides, the braking pressure excluded, insofar as this research's scope is studying the component response in a Free boundary condition. At this point, there was no data available for the humidity impacts on modal characteristics. Therefore, in this research, only the temperature factor is considered as a primary environmental feature. The Frequency Response Function measurements were conducted for a production pad at four temperatures: -15, 25, 100, and 150 (Celsius) within the braking operating conditions range. A high-fidelity numerical model was created in ABAQUS by accounting for material temperature dependency, nonlinear geometry formulations, and thermal expansion proportion (Equation IV.7).

The numerical model correlated to the temperature-dependent test data for a production pad tested in Ford NVH Development internal facilities; The comparison results in Table IV.3. The CAE frequency response function output is shown in Figure IV.13. This result displays a strong sensitivity of the Frequency Response Function to thermal variations. This result concludes that both natural frequency and response highly connected to the thermal effect, and the two normal-mode peaks (bending and torsional) shifted consecutively.

70

(Equation IV.7)

$$\epsilon^{th} = \alpha.\left(\theta, f_\beta\right).\left(\theta - \theta^0\right) - \alpha.\left(\theta^I, f_\beta^I\right).\left(\theta^I - \theta^0\right)$$

Where α is the thermal expansion coefficient; θ is pad temperature; θ^I is the initial temperature; f_β are the values of the predefined field variables; f_β^I are the initial values of the field variables; and θ^0 is the reference temperature for the thermal expansion coefficient. The second term in the above equation represents the strain due to the difference between the initial temperature, θ^I, and the reference temperature, θ^0.

Table IV.3. Comparison of the correlated CAE model results vs. the FRF test results

Temp. (c)	-15	25	100	150
Eigenfreq.1 Test (Hz)	2702	2595	2386	2305
Eigenfreq.1 CAE (Hz)	2670	2573	2377	2248
Var.	-1%	-1%	0%	-2%
Eigenfreq.1 Test (Hz)	4059	3861	3486	3395
Eigenfreq.2 CAE (Hz)	4027	3874	3562	3350
Var.	-1%	0%	2%	-1%
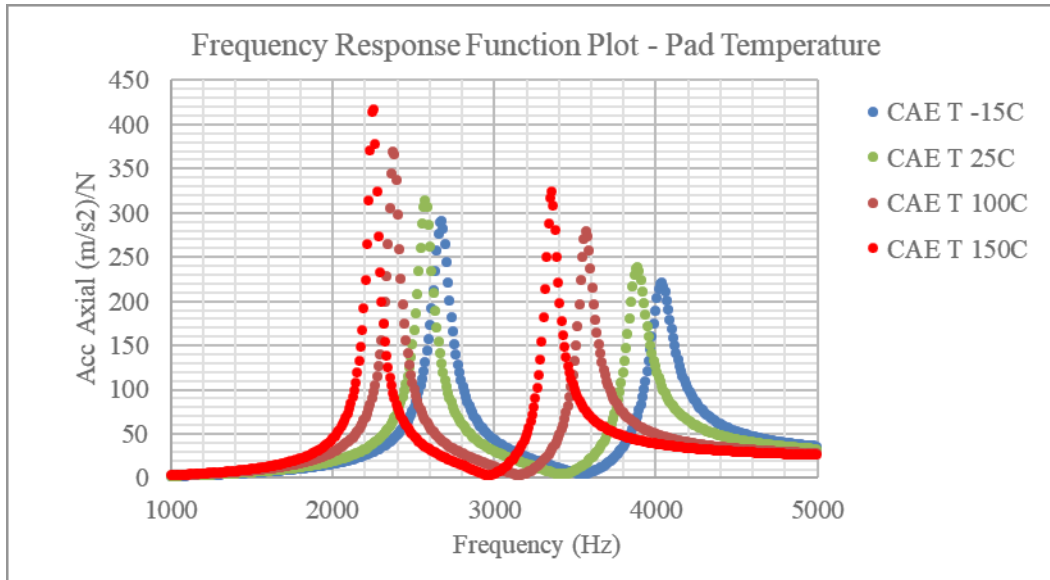
Figure IV.13. Brake pad Frequency Response Function plot for pad temperatures at: -15 C, 25 C, 100 C and 150 C

Methodology: A Structured Physics-Guided Machine Learning Technique

Machine learning (ML) models in recent years played a pivotal role to support critical decision making, automation of the time-consuming process, predicting the complicated systems, and advancing scientific discoveries [Karpatne et al. (2017), Karpatne et al. (2018), Nathan (2017) and Rahul Rai and Chandan (2020), Baker (2019)]. The state-of-the-art machine learning research has been making significant progress in many directions. In engineering, due to an increasing evolution of standard testing and design rules, ML has potential applications for product characteristics identification, decision-making, and process optimization, specifically in product developments [Willard et al. (2020)]. ML-based model aspires to equip a system with an intelligent element to automatically improve its performance through experience, pattern recognition, and statistical inference [Pham and Afify (2005)]. Progressive ML techniques discover sophisticated data patterns and transform information into an autonomous system that imitates human

intelligence and activities [Panchal et al. (2019)]. ML techniques increasingly developed and deployed in growing engineering and technology industries in a wide range of activities from the tuning of numerical parameters [Lynch et al. (2019)] and synthesizing high-dimensional optimizations [Chen and Fuge (2019)] to extracting human preferences and design strategies [Raina et al. (2019)].

However, Predicting the behavior of complex systems by only exploring correlation and reasoning relationships between inputs and outputs could be inefficient and may have multiple drawbacks. On the other hand, by developing physics-based models, it is expansive and infeasible to run many design iterations within the demanded resolution. Considering that neither an absolute ML-based nor an explicit physics-based methodology alone functions effectively for complex science and engineering problems. Thus, researchers are recently studying the continuum between mechanistic and ML models to incorporate merits from science-based and data-driven learnings [Karpatne et al. (2017) and Rahul Rai and Chandan (2020)].

Integrating science-based principles and ML models in a synergistic manner seems to be an efficient technique to accelerate computationally expensive physics-based models. The essential to this approach is to generate a data repository that could be used to discover a pattern for predicting the system's outcome. In many cases, this technique's disadvantages are that prediction is unreliable beyond the range of tested input variables. In training a machine learning algorithm directly from the operative data, it should be noted that the model prediction capability shrinks as parameters diverge from the trial data, considering the fact that machine learning algorithms tend to fail in predictions with an extrapolation nature. One remedy to improve predictive ability is to implement a physics-guided machine learning algorithm with a structured architecture that accounts for the complexity of input features and variables and allows for

73

expansion of the range of variables independently at any point. This facilitates the machine learning algorithm's training by employing a structured framework that is designed based on the physical properties of data. This technique provides a more precise image to find the patterns according to the underlying physics of the system [Willard et al. (2020), Karpatne et al. (2017), Schleder et al. (2019), Ivezic et al. (2019) and Raccuglia et al. (2016)].

This section provides an overview of a structured physics-guided machine learning technique that is the main contribution of this research work. The outline is drafted in the flowchart shown in Figure IV.14. The proposed approach aims to predict the brake pad's NVH modal characteristics from its physical features and feed the results into brake system NVH analysis.

The brake pad's physical features include geometry, material, and environmental features collected through experiments. These features are imported to both the ML model and the computational model (CAE). The computational model then generates a more extensive database through an iterative DOE to deliver adequate samples to the machine learning (ML) model. The output from this CAE DOE is the Frequency Response Function (FRF) of the pad, which converted to its mechanistic properties defined by three attributes of Eigenfrequency (Eigenfreq.), Acceleration (Acc.), and Loss Factor.

For the brake pad, geometrical features are available from either the parametric CAD model or the geometry library. Each brake pad may have different geometries and shapes, but the geometrical parameters remain the same as long as the fundamental structure doesn't change. Material features are collected through the material library, and environmental data is captured through experimental records.

In this study, a physics-guided machine learning algorithm is employed to combine experimental and computational data. With this basis, an advancement to the ML algorithm is

74

enforced by integrating data from the correlated CAE paradigm and correspondent physics. Input features are assigned by their physical property associated with distinct attributes. Aggregation of experimental and computational data provides higher precision for the predictive Machine Learning algorithm.
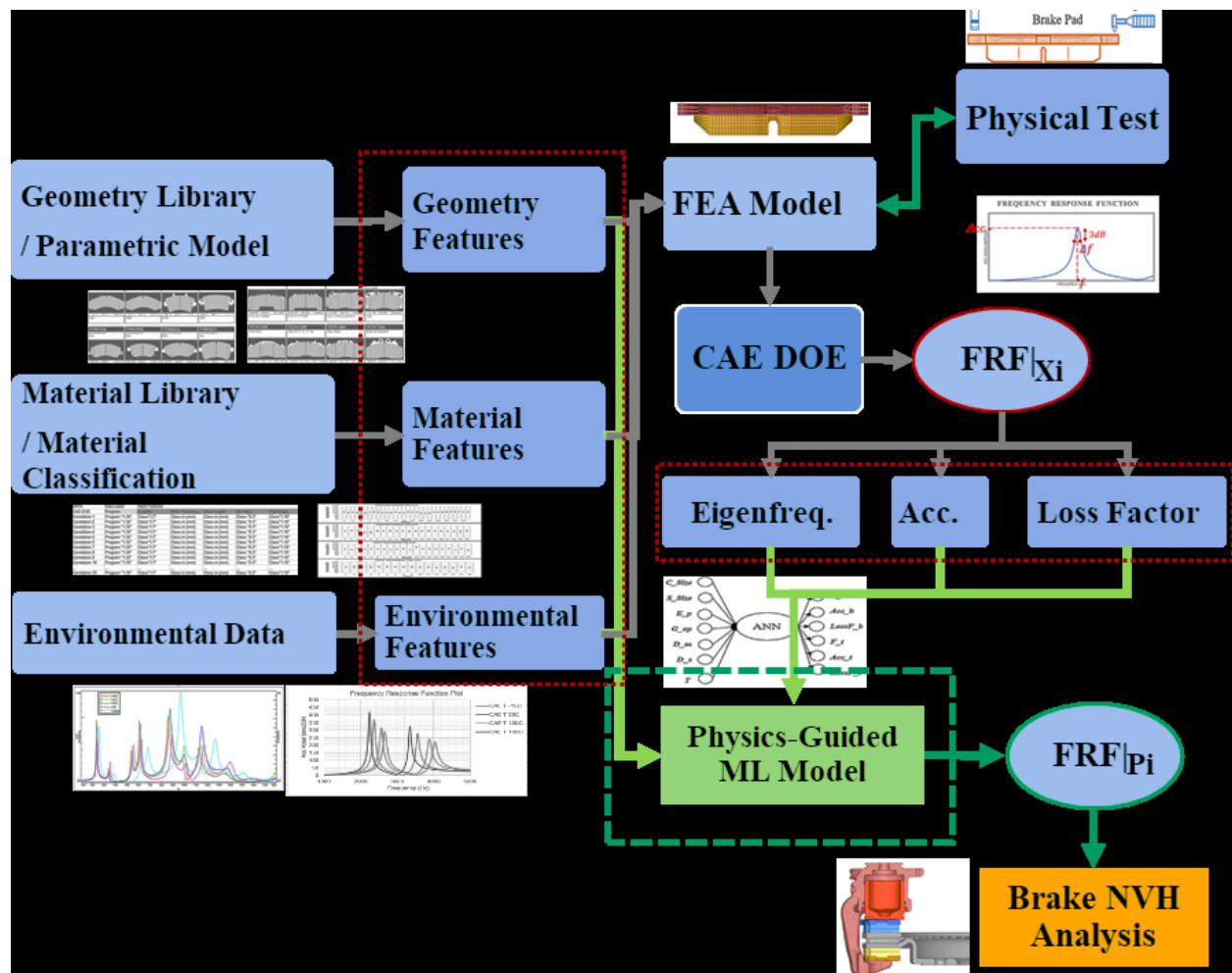
Figure IV.14. Methodology flowchart: employing a physics-guided ML model to predict modal characteristics from the physical properties of the brake pad
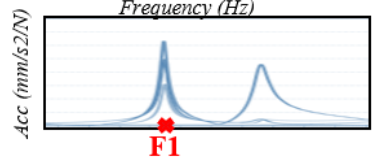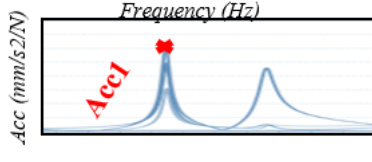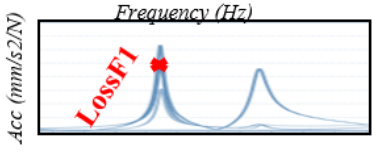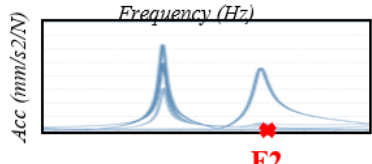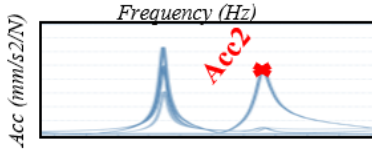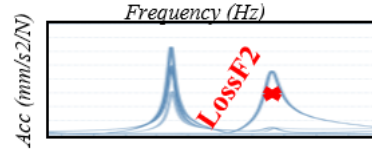
Data Analysis and DOE Interactions

Data in this study is collected from CAE DOE. The baseline model is precisely correlated with the experimental test result (SAE J2598 test). A case study with 9216 design iterations developed through a Design of Experiment (DOE), which ran through iterative CAE using ModeFrontier software (interface) and ABAQUS software (solver). The dataset consists of seven inputs and six outputs, as listed in Table IV.4. There are two geometry inputs: pad chamfer size (C_Size) and slot size (S_Size). Also, four material inputs include two elastic constants E_p and G_op and two damping parameters D_m and D_s. Lastly, the pad temperature as the environmental input.

Additionally, six outputs are driven based on the FRF plot. Three outputs define each eigenmode: including Frequency, Acceleration magnitude, and the Loss factor, for two normal modes of the pad. A feasible range for variables is decided according to the design and manufacturing constraint and the operating conditions range. The DOE iterations are established based on a pseudorandom selection of material and temperature variables and limited selections for geometry features.

Table IV.4. Parameters specification for the case study dataset

Input	Unit	Range	Dataset	Descriptions	Output	Unit	Descriptions
C_Size	mm	[0:20] % Pad Length	0, 10, 20	Chamfer Size (1D): Length	**F 1**	Hz	1st Eigenmode Frequency
S_Size	mm	[0:6] % Pad Length	0, 3, 6	Slot Size (1D): Width			
E_p	kPa	[-25:25] % C-Property	Pseudo random	Young's Modulus in the plane of isotropy	**Acc 1**	mm/s2/N	Acceleration for the1st Eigenmode
G_op	kPa	[-25:25] % C-Property	Pseudo random	Shear Modulus normal to the plane of isotropy	**LossF 1**	NA	Loss Factor for the1st Eigenmode
D_m	NA	[-25:25] % C-Property	Pseudo random	Mass Proportional Damping value	**F 2**	Hz	2nd Eigenmode Frequency
D_s	NA	[-25:25] % C-Property	Pseudo random	Stiffness Proportional Damping value	**Acc 2**	mm/s2/N	Acceleration for the 2nd Eigenmode
T	C	[-15: 150]	-15, 25, 100,150	Pad Temperature	**LossF 2**	NA	Loss Factor for the 2nd Eigenmode

In general, a correlation between two variables is defined by measuring a linear association between those two variables, which is a value between -1 to 1. A correlation coefficient value close to 1 or -1 indicates the two variables are ideally correlated (respectively, with a positive or negative relationship). Additionally, a correlation coefficient close to zero indicates variables have poor correlation, or in other words, variables are linearly unassociated. The correlation analysis shows what variables have a relationship with another; however, it doesn't provide any insights into cause and effect relationships. In this data analysis, the Pearson correlation approach is used, a common technique in science and engineering. Pearson product-moment correlation coefficient (PPMCC) measures the strength of linear dependence between two variables x_1 and x_2, defined by Equation IV.8 as following [Hogg et al. (2014), Lindeman et al. (1980)]:

(Equation IV.8)

$$\rho_{x_1,x_2} = \frac{COV\ (x_1\ , x_2)}{\sigma_{x_1}\ \sigma_{x_2}} = \frac{E[(x_1 - \mu_{x_1})\ (x_2 - \mu_{x_2})]}{\sigma_{x_1}\ \sigma_{x_2}}$$

Where, COV is the covariance and σ is the standard deviation. Additionally, in the other form of the equation μ is the mean and E is the expectation.

Parallel to the correlation matrix, a scatter matrix chart shows any dependency between the variables. Still, it also provides information such as the nature and the strength of such correlation, how data is dispersed, visualize the distribution of data, and enables detection of the outliners. Besides, a potential advantage of the scatter plots is it allows to explore non-linear relationships between variables.

The correlation and scatter matrix chart shown in Figure IV.15 displays the relationships of all the input and output features for the iterations executed in the CAE DOE through this work. The scatter charts for each variable pair are shown in the upper triangular of the matrix. The

correlation charts are shown in the lower triangular; the probability density function charts are shown on the matrix's main diagonal.

In this analysis, a general guideline is used as an indicator for determining the strength of the correlation:

- Coefficient from 0.1 to 0.3 and -0.1 to -0.3 considered as low strength correlation.

- From 0.3 to 0.5 and -0.3 to -0.5 considered as medium strength correlation.

- From 0.6 to 1.0 and -0.6 to -1.0 considered a high strength correlation.

This analysis (Figure IV.15) demonstrates a strong linear correlation between the acceleration responses for the 1st and the 2nd eigenmodes. Also, there is a significant relationship between the acceleration responses and the loss factors. Furthermore, there is a positive linear correlation between the 1st and the 2nd eigenmodes' loss factor. For the input features, elastic constants E_p and G_op mainly tied positively with the eigenfrequencies. Another observation is that the mass proportional damping D_m negativity correlated with the Loss Factors and Acceleration Peaks. Also, for the geometry variables, the slot size (S_Size) is adversely connected with the outputs. Besides, there is a strong correlation between the material elastic constants and the temperature inputs.
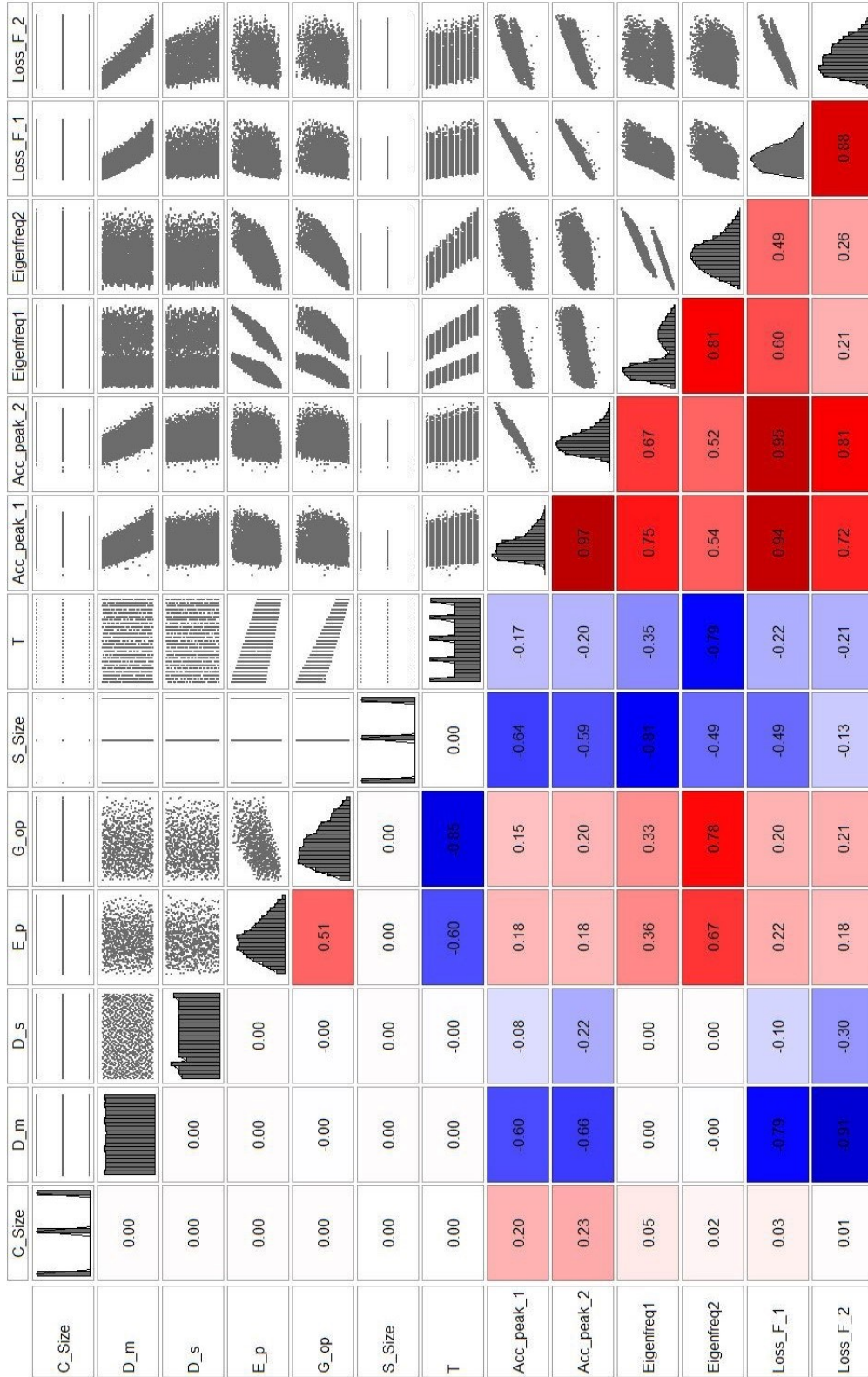
Figure IV.15. The correlation and scatter matrix chart for all the input and output features from the CAE DOE dataset

Interaction Effect in Statistics is defined by a condition that a concurrent effect of two or more covariates on an outcome is not additive. The impact of one covariate on the outcome depends on the state of the other covariates. Interactions analysis gives an insight into how to evaluate better a relationship between covariates in the model and their effects on the outcome, leading to improving the model fit [Hayes and Matthes (2009)]. In a more complex scenario, independent covariates could interact with another, and a third variable influences the relationship between an independent and dependent variable. In this situation, it is crucial to incorporate the effect in the model to capture a more pragmatic implication of the real behavior [Hayes and Matthes (2009), Aschard (2016), Jaccard, and Turrisi (2003) and Reno et al. (1991)].

A DOE Interaction Effects explored here using ModeFrontier software. The Interaction Effects Chart refers to a sequence of box-whiskers plots that visualize the first-order interaction effects to assess the significance of the interactions through the evaluated factors. Interaction Effect accounts for contributions of the product of factors for 2-level and 3-level analysis. For two variables x_1 and x_2 the Interaction Effect is calculated by Equation IV.9. For 2-level analysis only $x_1 + x_2$ terms are considered; for the 3-level analysis both $x_1 + x_2$ and $x_1^2 + x_2^2$ terms are accounted. Albeit, in this study only the 2-level analysis evaluated.

(Equation IV.9)

$$F_{(x_1, x_2)} = k + x_1 + x_2 + x_1 x_2 + x_1^2 x_2 + x_1 x_2^2 + x_1^2 + x_2^2$$

Each factor initially ranked by low and high rank, then by multiplying each factor by all the other factors, a new rank calculated and assigned is shown with a box-plot at each level. A factor considered significant if it has a more remarkable shift from negative to positive levels concerning the outcome. The slope of the connecting line denotes variation; a steeper slope implies a larger variation that indicates a significance of that factor. A positive slope indicates that the

81

given factor and the outcome positively correlated, whereas a negative slope indicates a negative correlation. The Interaction Effect chart for input variables with respect to the FRF outcomes shown in Figure IV.16-18 for the dataset in this study. For eigenfrequency outcomes at both normal modes (Figure IV.16), an apparent positive correlation exists for G_op*S_Size and E_p*S_Size. At the 1st eigenfrequency, a significant negative correlation factor appears for C_Size*S_Size. At the 2nd eigenfrequency, E_p*G_op, S_Size*T, and C_Size*T are prominent factors.

For the acceleration peaks (Figure IV.17), a strong correlation exists for G_op*S_Size and E_p*S_Size and then D_m*G_op and D_m*E_p. Also, there is a substantial negative correlation for C_Size*D_m, S_Size*D_m, and C_Size*S_Size. For the Loss factors (Figure IV.18), a dominant positive tie corresponds to the D_m*E_p and D_m*G_op and dominant negative factors associated with C_Size*D_m, S_Size*D_m.
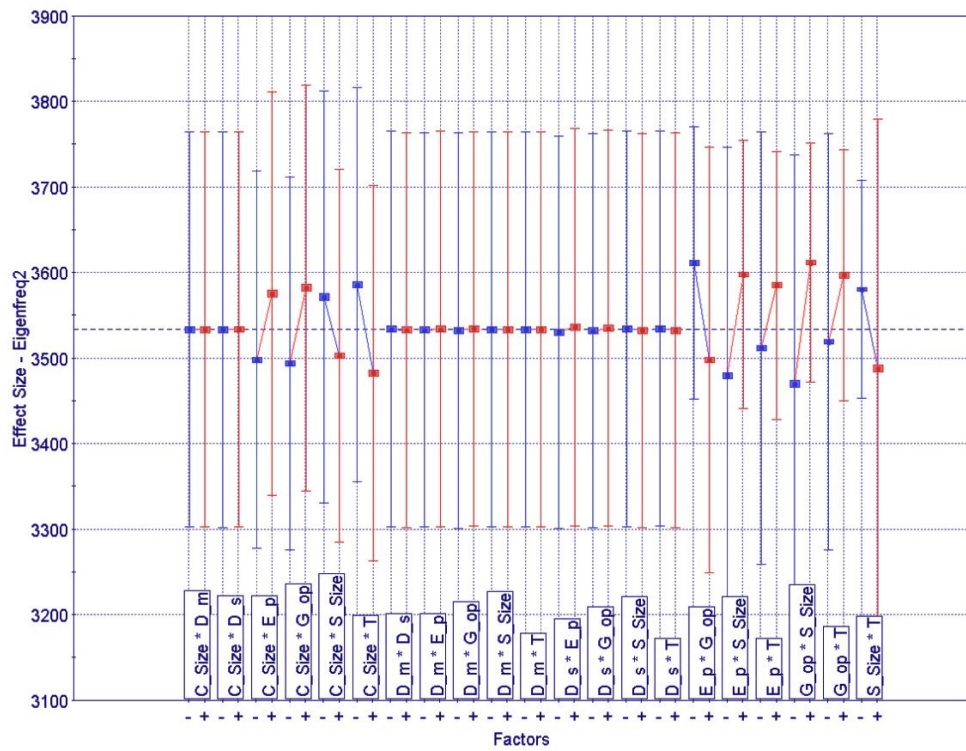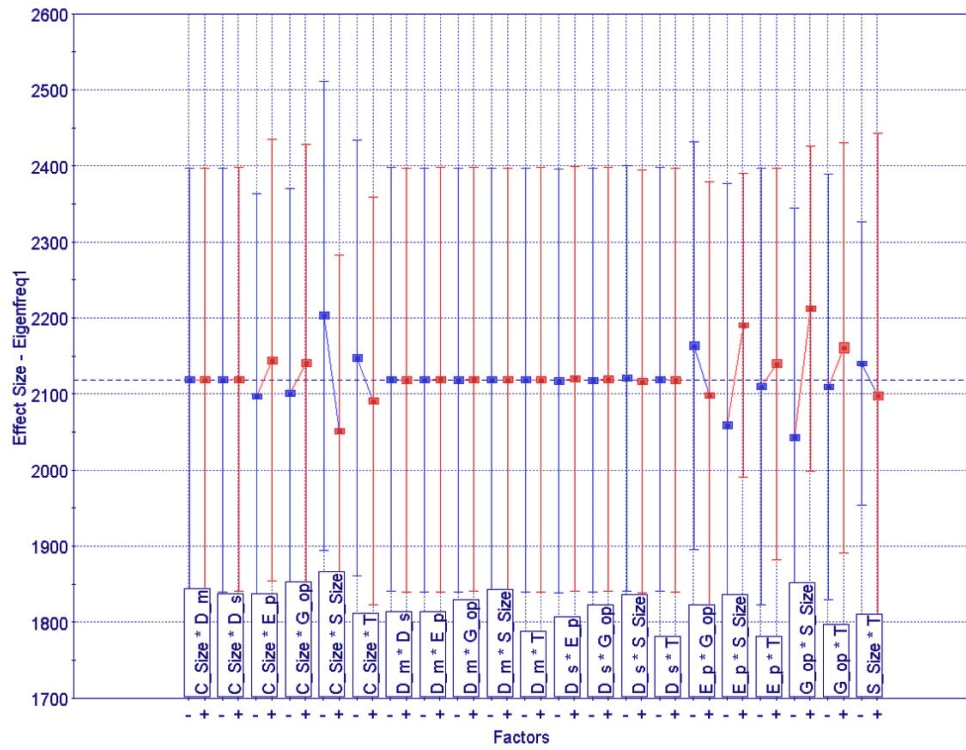
Figure IV.16. DOE Interaction Effect chart for input variables for the outcome: Eigenfreq1 and Eigenfreq2
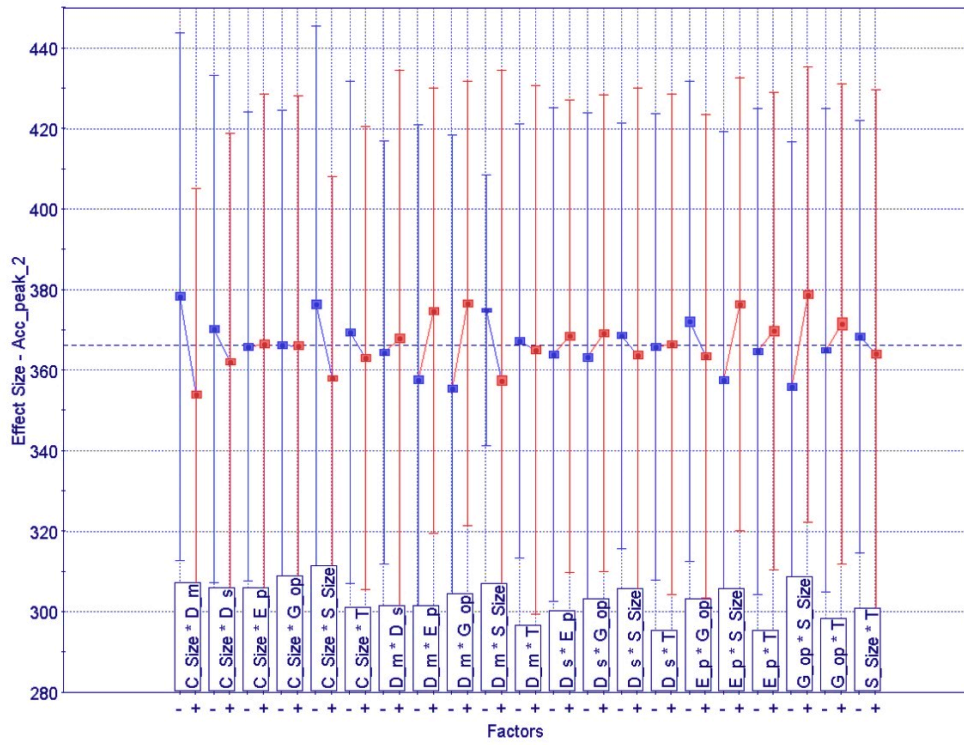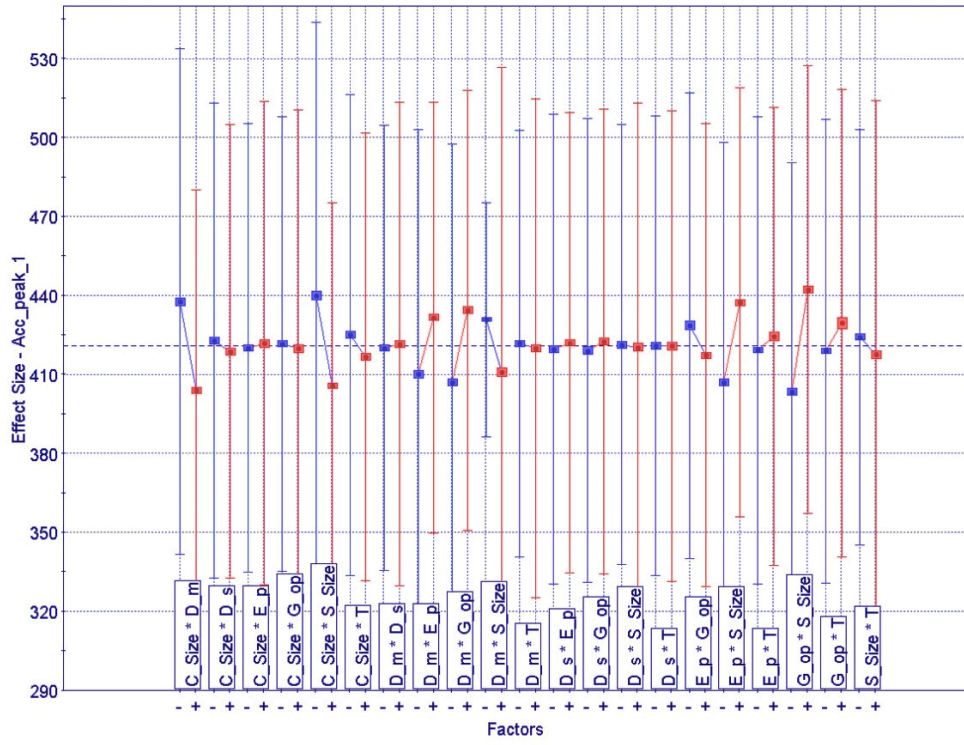
Figure IV.17. DOE Interaction Effect chart for input variables for the outcome:
Acceleration_Peak_1 and Acceleration_Peak_2
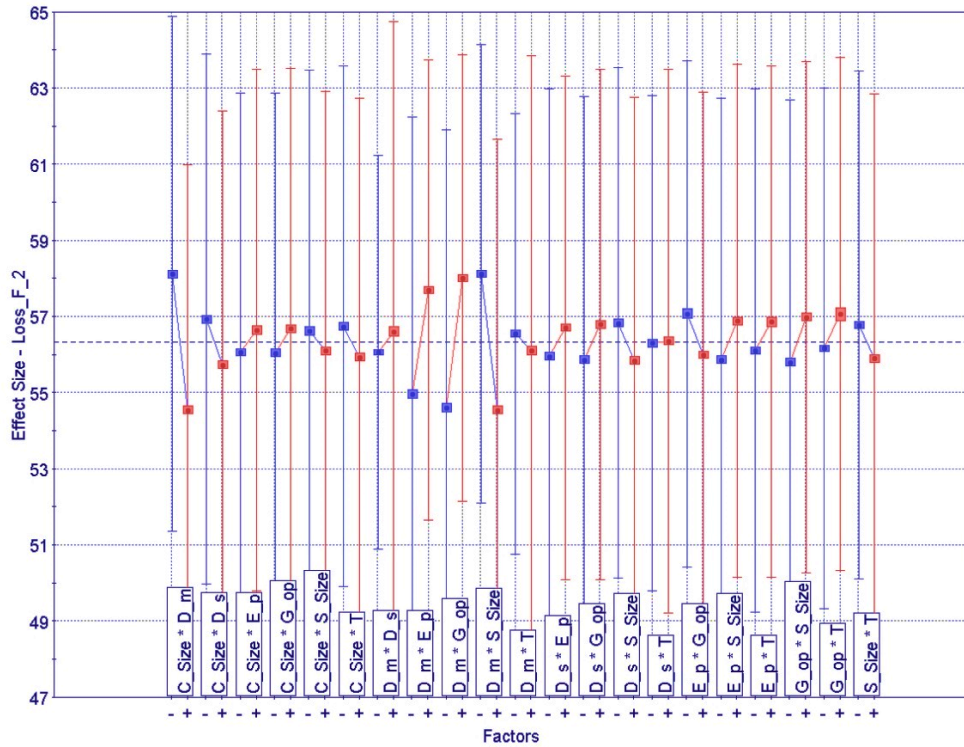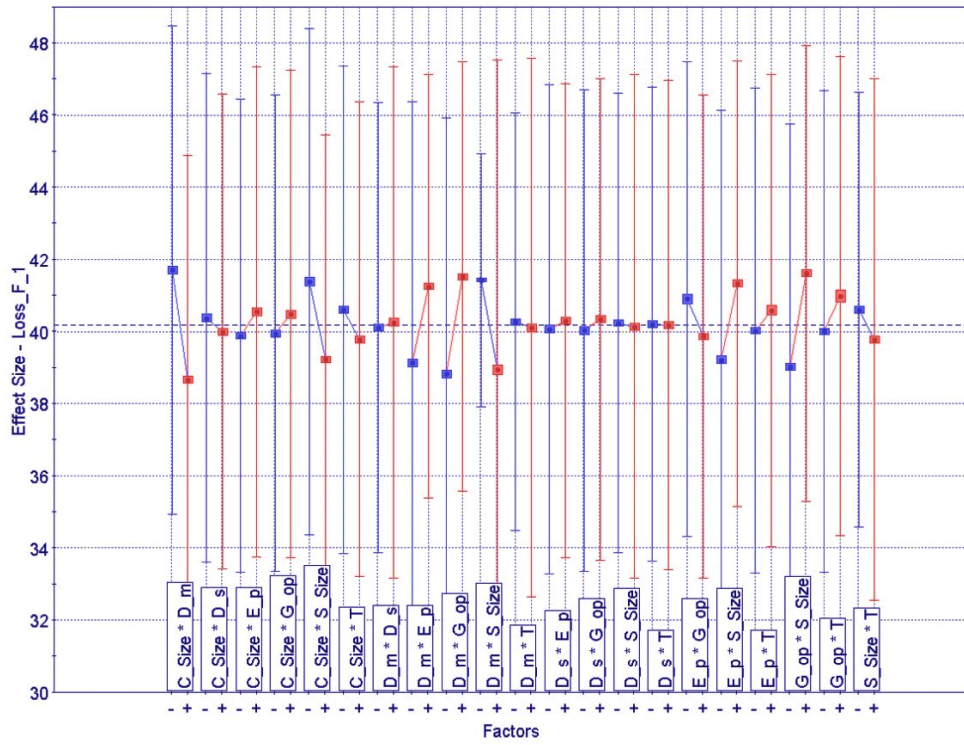
Figure IV.18. DOE Interaction Effect chart for input variables for the outcome: Loss_Factor_1 and Loss_Factor_2

Implementing an Innovative Deep Learning Model

In machine learning, the area referred to as brain-inspired computation is categorized as an Artificial Neural Network (ANN) inspired by the brain's biology. ANN mimics the basic form and functionality from a human brain's physics that simulates an interconnected process that can learn and operates as an intelligent program. But, unlike a biological brain that neurons connect within a distinct space, ANN has a particular pattern of layers and connections with their directions of data propagation [VanRullen (2017), Hassoun (1996) and Esser et al. (2016)]. In other words, Artificial Neural Network (ANN) is a computational arithmetic model acquired by information processing emulating the human neural network. Neurons in Neural Networks are connected and specified by an output function called an excitation function. The neuron's computation entails a weighted sum of the input values. Any change to the connection modes, weight (synapses), and the excitation function changes the network's output [Hassoun (1996)]. The functional operation within the neuron performed on the combined inputs can be a non-linear function that results in creating output for the inputs by exceeding a threshold. In this definition, neural networks apply a non-linear function to the weighted sum of the input values. Weighted sums being propagated through the neurons from the input layer to the hidden layers and eventually receives to the output layer [VanRullen (2017), Hassoun (1996) and Esser et al. (2016)].

Deep learning is a newer field of machine learning that emerged from ANN researches in the 1960s [Lecun (2015)]. Deep learning generally referred to a domain of Neural Network in which the network has more than one hidden layer, and it is often called Deep Neural Networks (DNNs). DNNs can learn multi-level representations of complex neural networks with many features, and they showed superior performance in processing visual data and images. Deep learning is believed to have increasing success from the 2010s due to 1- rapid grow of training

data and information, 2-advances in semiconductor devices and computing capacities, and 3-development of algorithms and frameworks that facilitates research and explorations [Sze et al. (2017), Russakovsky et al. (2015) and Deng et al. (2013)]. Since then, it has widely been used in many applications from multimedia [Pouyanfar et al. (2018) and Girshick et al. (2014)] to robotics [Kustikova and Druzhkov (2016).], medical [Esteva et al. (2019), Angermueller et al. (2017) and Ching, T. et al. (2017)], and engineering design and product developments [Márcia et al. (2020) and Stender et al. (2021)]. The aim of training the Deep Neural Networks (DNN) is to establish the value of the weights and bias to optimize the model's score depending on the defined metric. If the metric is defined as Loss, its score is appraised by the difference between prediction and actual outcomes. Therefore, the model objective is to search for the best set of weights that minimize the Loss through the training dataset. By applying the gradient descent approach, the weights are updated given Equation IV.10, by computing the partial derivative of the Loss concerning the weight. This gradient determines the updated weights to minimize the Loss through an iterative process [Sze et al. (2017)].

(Equation IV.10)

$$W_{ij}^{t+1} = W_{ij}^t - \alpha \, \frac{\Delta E}{\Delta W_{ij}}$$

Where, W_{ij} are weights and, α is called the learning rate and E is Error.

A backpropagation technique is used to compute the gradient's partial derivatives and update the weights regarding the loss. Various techniques employed to train the weights depend on the application. The DNNs are classified according to their learning mode to supervised, unsupervised, and reinforcement learning (a special form of supervised learning). The backpropagation algorithm described here is supervised learning, one of the most frequent neural networks approach adopted for multilayer perceptron (MLP) [Sze et al. (2017), Towell and Shavlik

(1993) and Craven (1997)]. These DNNs have superior performance in many tasks and provide a general pragmatic module for learning numerical and categorical data that is robust to noise in the training data. However, their drawbacks are: 1- They can create too convoluted models that are hard to perceive and 2- They can computationally be very expensive [Pham and Liu (1999) Haykin (1994) and Mitchell (1997)]. Nonetheless, there has been an expansion of development and research in recent years that specifically concentrated on these two issues [Hsieh (2009)].

This research employs a supervised, structured Deep Neural Network (DNN) with seven inputs and six outputs to fit the database collected from the CAE DOE (Shown in Figure IV.19). Input features subdivide into three main groups: 1- Geometry group composed of pad chamfer size (C_Size) and slot size (S_Size). 2- The material group that includes the material elastic constants of in-plane Young's modulus (E_p) and out-of-plane shear modulus (G_op), and damping features of mass proportional damping (D_m) and proportional stiffness damping (D_s). 3- Environmental group composed of the pad temperature. On the other side, outputs are Frequency, Acceleration magnitude, and the Loss factor for the first two eigenmodes of the pad.
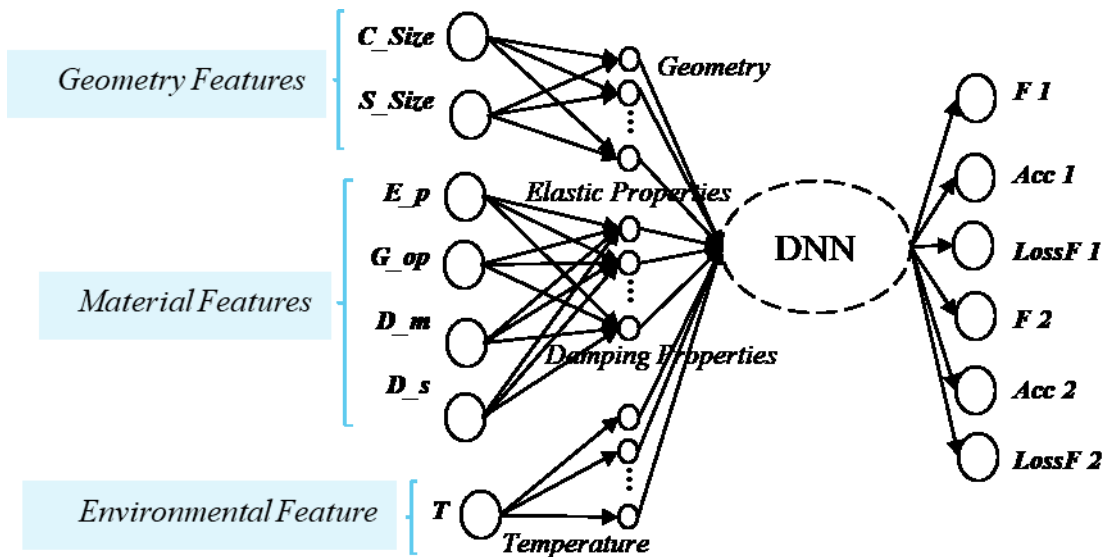
Figure IV.19. A schematic of the DNN model with multi-input and multi-output

Innovative network architecture is defined with distinct inception modules consisting of geometry, materials, and environmental blocks. This architecture allows multiple-input, including numerical and categorical data in a single end-to-end network with separate neurons, layers, activations, and normalization structures. The modules then are concatenated to get maximal multiscale features of the data. For each module, a distinct multi-layer perceptron (MLP) is developed and finally combined with other MLPs, as shown in Figure IV.20. The features are extracted from a fully connected layer, and after the concatenation from different Inception modules are passed to the final MLP, between the combined inputs and the outputs. The advantage is that each deep layer Inception module could be structured separately, which induces a superior performance for the overall network.
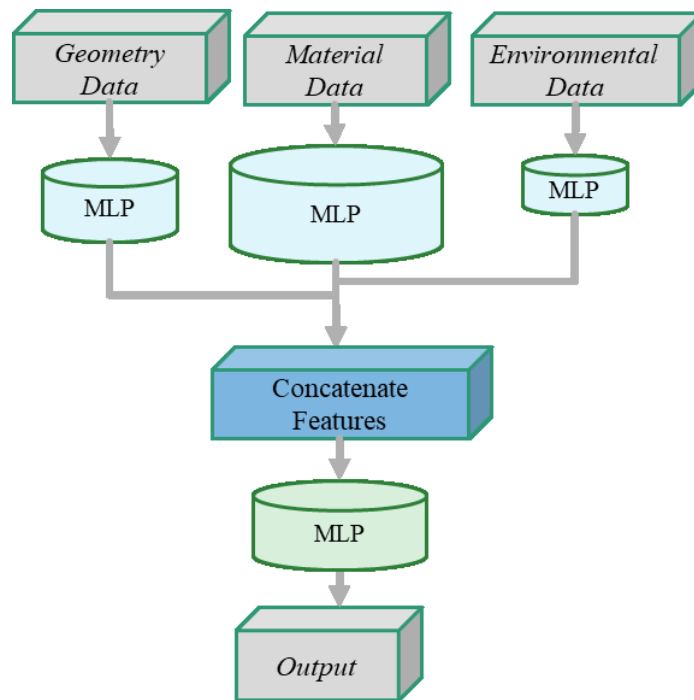
Figure IV.20. Architecture of the DNN model with distinct modulus and concatenated features

The structured DNN model proposed in this work is based on a backpropagation technique. It uses hyperparameters for training and optimizes those through training utilizing a loss function and an optimizer. Progressively, the loss function learns to minimize the prediction error with the assist of an optimization function. This deep learning model's primary task is learning a function approximation between input and output features that partially benefits from its deep structure. A decent training strategy for parameter updating is important to achieve the desired results. Through the data preprocessing, all input features initially scaled using the min-max scaler, which translates each input individually such that it values returns in a range of [0, 1]. This preserves the original distribution's shape; besides, the meaning of the information embedded in the original data remains the same. The data split to separate training and validation sets with a distribution of 85 to 15 percent (on the total sample size of 9216).

Next, the structure of hidden layers and neurons are determined for each of the three MLP modules by developing a hybrid algorithm. This hybrid algorithm explores each MLP under an iterative fashion for hidden layers and selects the number of nodes (neurons) through a flexible random sampling. The number of the hidden layers iteratively increased from 1 to the number of inputs. In parallel, flexible random selection allows the user to determine the scale of the trial. It is given by a lower bound, higher bound, and a sampling size so that it could be adjustable for a larger or smaller scale of design space depends on the condition. If it is needed for a more in-depth search, these three parameters could be adjusted to fit the desired design space. Ultimately, these three MLP modules concatenate to generate a combined input for the latter MLP that links the combined input to predicted outputs. Conditioning is imposed for the learning process to define a constraint for the maximum number of parameters allowed in the network structure. The conditioning not just balances the parameters but improve interpretability and addresses overfitting

issues. The constraint limits the number of parameters to be less than 80% of the overall training sample size. This restricts the search space and thus over-complexity for the network structure.

This study investigates two different optimizer algorithms, Adam and RMSProp. The Metric for compiling the model is the root means square error (RMSE). Also, the learning rate for optimizer is tuned through trial and error. Adjusting the learning rate is crucial for model training. Because a high learning rate could increase loss error and results in extreme weight changes, on the contrary, a low learning rate can prevent these problems but increases convergence time. A rectified linear unit (ReLU) activation function was used for each intermediate layer, and a linear activation applied to the output layer due to the dataset's nature. Finally, the number of epochs and batch size decided using empirical analysis. An overview of the algorithm developed for the entire deep learning model structure is depicted in Table IV.5.

Table IV.5. An overview of the algorithm for the deep learning model structure

Step	Function
1	**scaling**: min-max scaler [0,1]
2	**data split**: training-set←85% (s-size) & validation-set ←15% (s-size)
3	**constraint**: par-number ≤ **0.8** * s-size
4	**for** n = 1 to length (input) **do**
	| **l**-bound-nodes & **h**-bound-nodes & nodes-size {*user-defined*}
	| create MLP-Geo (**l**-bound-nodes, **h**-bound-nodes) {activation}← ReLU
	| **for** n = **l**-bound-nodes to **h**-bound-nodes **do**
	| | **return** model MLP-Geo
	| **end**
	| create MLP-Mat (**l**-bound-nodes, **h**-bound-nodes) {activation}← ReLU
	| **for** n = **l**-bound-nodes to **h**-bound-nodes **do**
	| |**return** model MLP-Mat
	| **end**
	| create MLP-Tem (**l**-bound-nodes, **h**-bound-nodes) {activation}← ReLU
	| **for** n = **l**-bound-nodes to **h**-bound-nodes **do**
	| | **return** model MLP-Temp
	| **end**
	end
5	[combined input] ← **concatenate** [MLP-Geo, MLP-Mat, MLP-Temp]
6	create MLP {activation}← Linear
	[prediction] ← **model** [combined input]
7	**model compile** (optimizer, metric = loss)
	{optimizer} ← Adam & RMSProp {*learning rate, decay*}
	{loss} ← root means square error (RMSE)
8	**model fit** ([X-Geo, X-Mat, X-Temp] $_{training}$, [Y]$_{training}$)
	([X-Geo, X-Mat, X-Temp] $_{validation}$, [Y]$_{validation}$)
	{*epochs, batch size*}

Results and Discussion

This section presents results and discussion for the implemented deep learning model described in the previous section. The architecture and algorithm for the deep neural network model elaborated. The model is investigated here uses the database presented in the past section in Table IV.4. Based on the input features, a unique flexible structure for hyperparameters (the number of hidden layers and neurons) is specified to optimize the deep learning model. In this case study, the structure of DNN is determined by the arrangement of the number of hidden layers at each of three MLP modules: Geometry, Material, and Environmental. The number of hidden layers at each MLP increased from 1 to the number of inputs (inside the MLP). This process carried out iteratively as the structures produced are listed in Table IV.6. The neuron numbers in each layer are decided by the user; in this study, specified as a random independent selection of 20 iterations in a given range of 8 to 40 nodes at each hidden layer. As a result, this experiment generates 140 different DNN models categorized by seven unparalleled structures. With the conditioning applied to the number of parameters, the parameters are limited to 6635. Therefore, for the feasible designs evaluated in this case study, the model's complexity remains within this constraint. A major task here is finding the optimal model complexity that minimizes the validation (test) error. The general guideline used to find the best model complexity regarding comparing the performance of training and validation datasets shown in Figure IV.21.
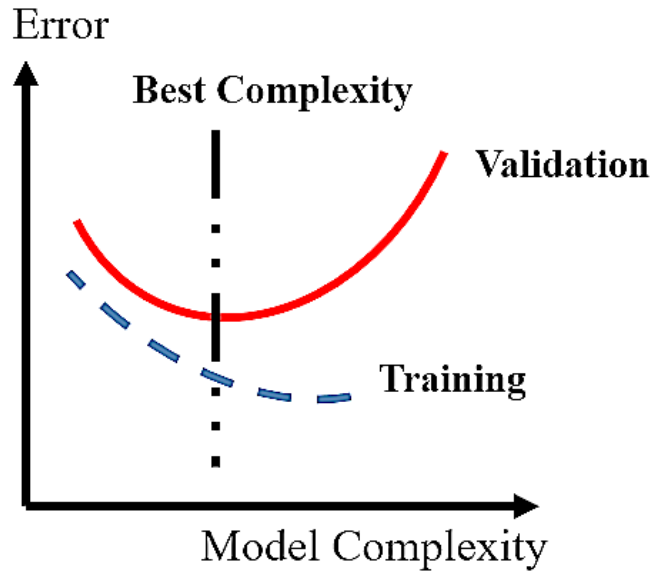
Figure IV.21. General guideline for best model complexity

Table IV.6. The case study DNN structures (number of hidden layers)

DNN	# of H Layers (Geometry MLP)	# of H Layers (Materials MLP)	# of H Layers (Environmental MLP)
DNN s -1	1	1	1
DNN s -2	1	2	1
DNN s -3	1	3	1
DNN s -4	1	4	1
DNN s -5	2	2	1
DNN s -6	2	3	1
DNN s -7	2	4	1

A resolution to adopt the premier feasible DNN structure obtained by a trade-off of minimum loss score for validation dataset regarding the number of parameters. The number of

parameters determined by the arrangement of neurons and hidden layers. Two optimizers RMSProp and Adam, investigated through all 140 deep learning models.

The results presented correspondingly in Figure IV.22. (a) and (b). Each cluster for the DNN structure is displayed with a distinct color mark. The primary observation is the clusters with the least complex structure condensed more in the min-loss region. Comparing the DNN s-1 (with only one hidden layer at each module) to DNN s-7 (with two geometry layers and four material layers) indicates that the model can perform efficiently with minimal convolution. However, Adam optimizer shows a slight improvement in higher complexity with certain node arrangements. The other important observation is that the neuron numbers sequence appears to be more effective, particularly where the hidden layers structures become more convoluted. One further remark is in plot (b) with the Adam optimizer; a horizontal trend of the minimal loss is witnessed from approximately 1300 to 3600 parameters; This indicates that eminent convergence is achievable by optimizing the neuron number arrangements departs from the depth of the hidden layers. That means by optimizing the nodes' arrangement across a less complex structure, convergence to the optimal paradigm is forthcoming.

(a)
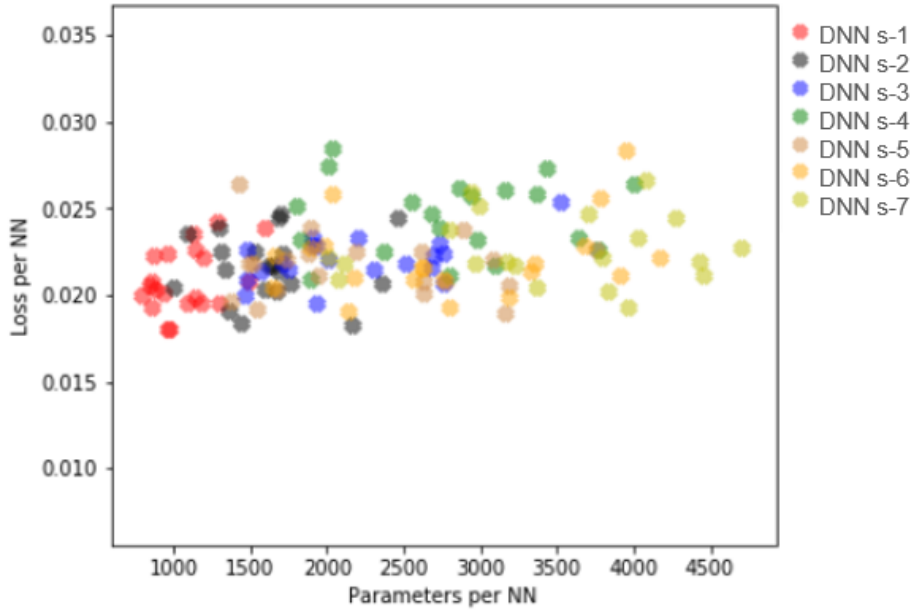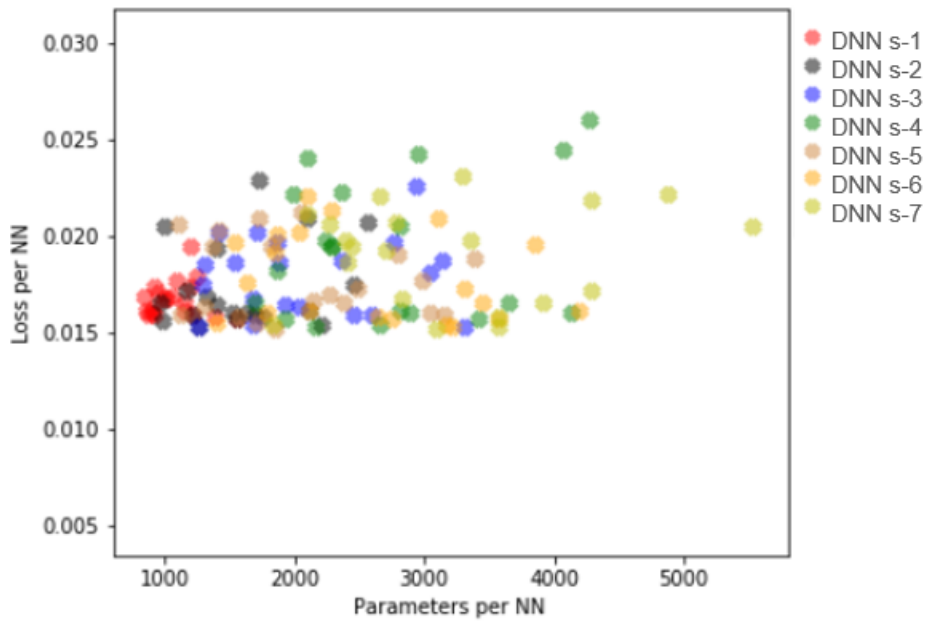
(b)

Figure IV.22. DNN models trade-off based on validation loss vs. number of parameters: (a) RMSProp and (b) Adam optimizers

Regarding the primary observations on various network structures, a high-fidelity exploration was performed with reference to the DNN s-1 model (composed of a "1-1-1" hidden layers structure). This is conducted by taking a deep dive into the hyperparameters search for node number arrangements at every hidden layer in geometry, material and environmental MLPs. The new exploration broadens the design space to 100 iterations to uncover the best practicable neurons arrangements. The node number range is a carryover from the previous study (from 8 to 40). 3D scatter plot and heatmap are found as meaningful, intuitive tools that allow for transparency to explore interconnection mapping between hyperparameters in this case study. The bivariate interconnection mapping for each two MLP modules concerning the neuron numbers (of hidden layers) in response to the min-loss score is demonstrated in Figure IV.23 and Figure IV.24. The min-loss values are computed based on the validation dataset. The detection of minimal loss explores the optimum region through this multivariate design space. This analysis provides insight into a smart selection of neuron number arrangement to optimize the learning model for an optimum hyperparameters margin.
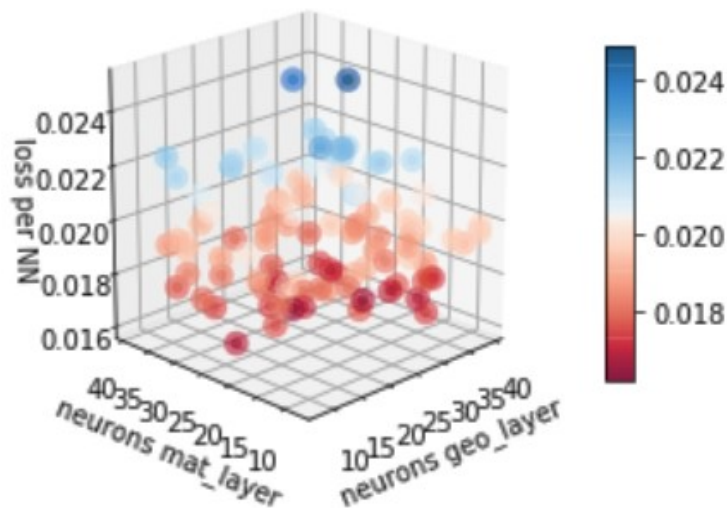
(a)

(b)
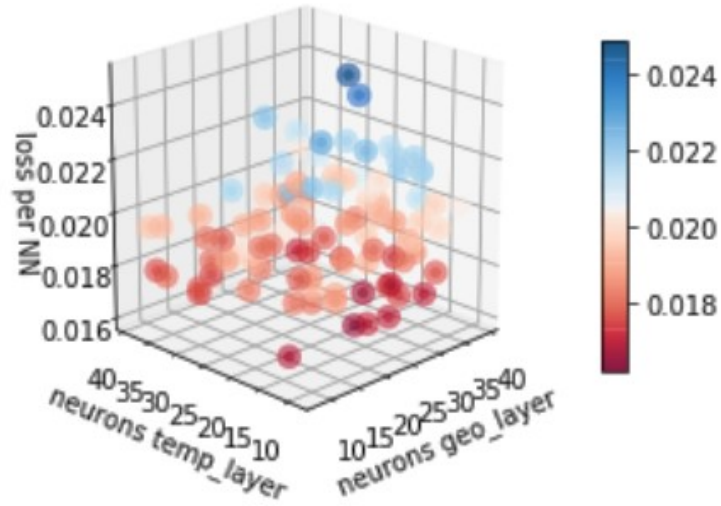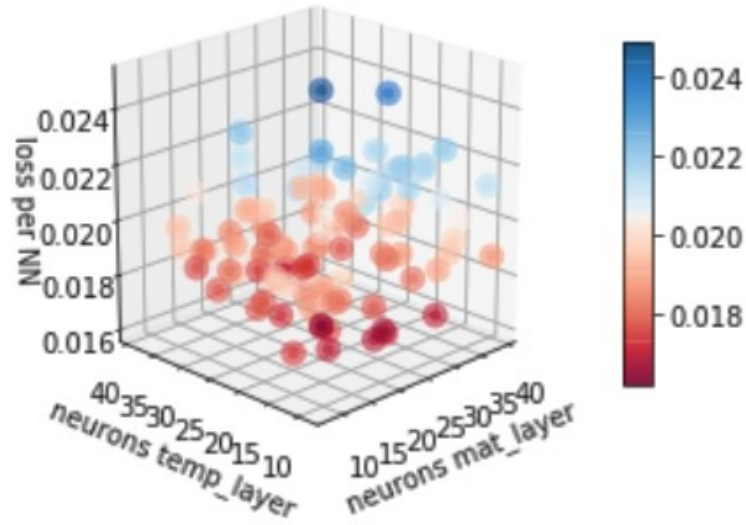
(c)

Figure IV.23. Scatter plot for neuron number exploration: (a) Geometry vs Material, (b) Geometry vs. Environmental and (c) Material vs. Environmental
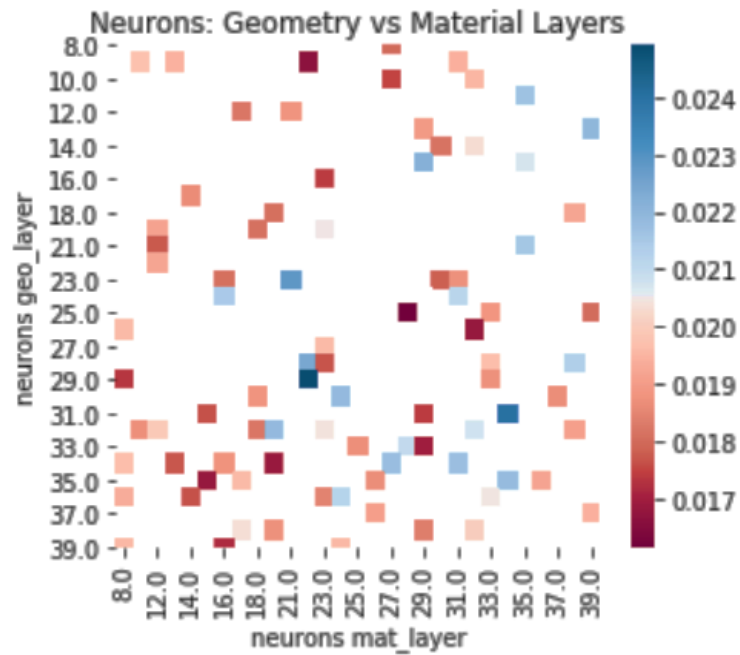
(a)
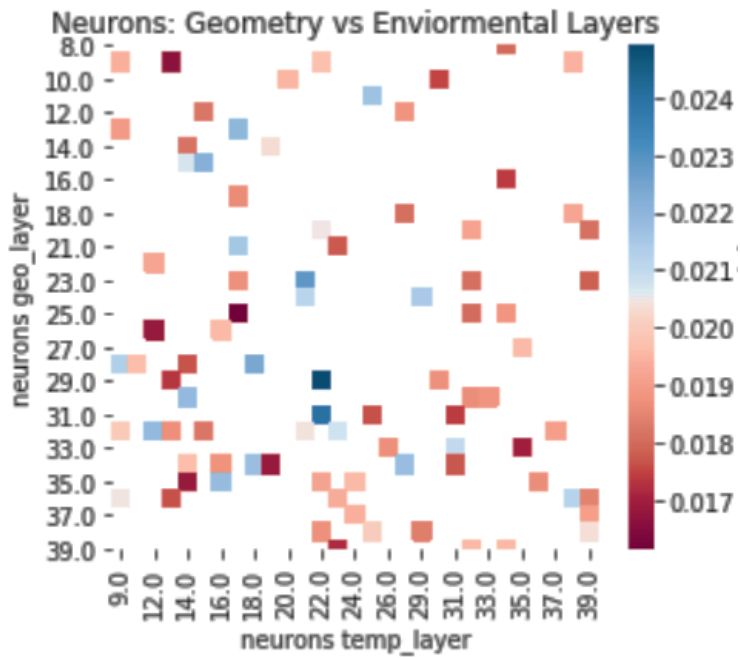
(b)
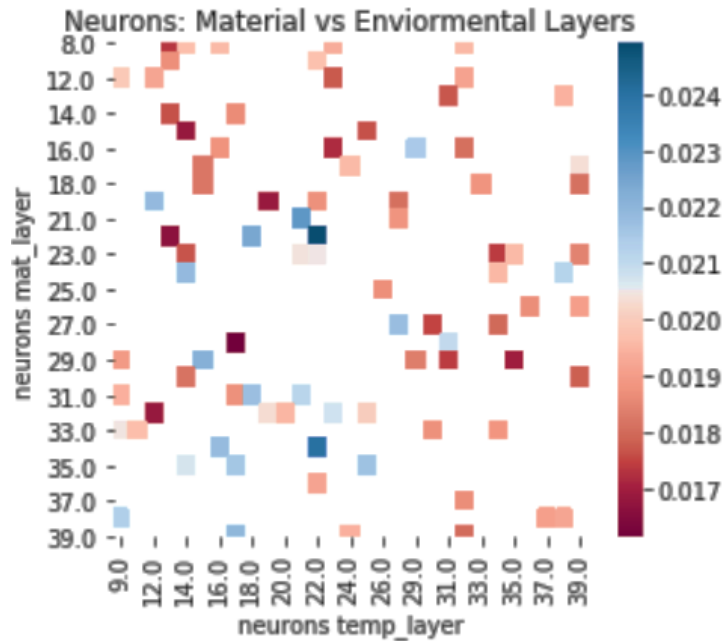
(c)

Figure IV.24. Heatmap plot for neuron number exploration: (a) Geometry vs Material, (b) Geometry vs. Environmental and (c) Material vs. Environmental

Learning curves is a classic indication of learning performance over the sequences. In this study, the learning curves measured on the loss metric bases to evaluate and diagnose the model; the same reference the model parameters are being optimized. The score for loss monitored over the number of epochs and the model behavior investigated for under/ overfitting. An epoch here refers to a pass that the model goes through the training samples during the learning process. The model behavior is evaluated on the training dataset and the hold-out validation dataset. It is worth noting that the training dataset and validation dataset are exclusively independent.

As shown in Figure IV.25, for the Optimal DNN model, a decent fitting achieved for the learning curve on training and validation sets. This gives an insight into what degree the model is learning as well as generalizing. After passing 5 to 10 epochs, the loss reaches a stability point

with a minimal gap between the two dataset losses. Accordingly, this indicates the model optimized to a level that efficiently converges.
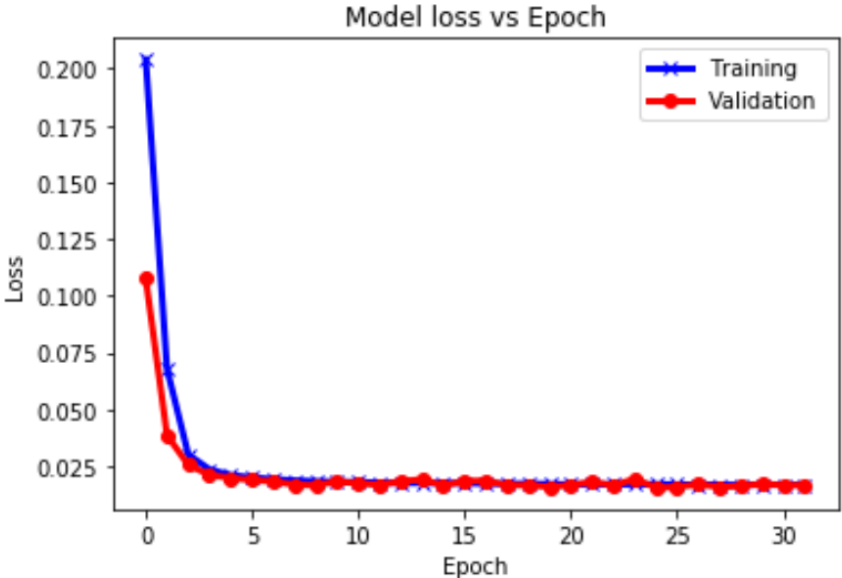
Figure IV.25. Learning curve for the optimal DNN model through training and validation sets

CHAPTER V

Future Works

Brake NVH and particularly brake squeal is due to dynamic instability of the brake system. This phenomenon contains complex physics due to its nature of the problem and complicated interconnections and variation within the subsystems; also, a wide range of operational conditions and a broad range of frequency.

Currently, Analytical approaches integrated with numerical finite element simulation provide a somehow understanding of the phenomena and estimating squeal behavior for designing the brake system. However, still, it requires some physical experiments to guide and coordinate the computational investigations. The author believes that with the advances in CAE methods on the one hand and significant development and progress in the area of Artificial Intelligent (AI) in recent years, it is now feasible to develop a machine learning tool integrated with the numerical model that:

- Facilitates the prediction of the brake squeal.
- Provides an efficient tool to adequately estimating brake components' NVH modal characteristics from their physical properties.

The first part of this research describes the most recent CAE methodologies and advancements for brake squeal. Then, it proposes a new metric based on the exploration of cross-checking the operating condition distributions from the result of the computational model to

physical experiments. Besides, this work introduces a statistical technique and implements it to enable this investigation. An ML algorithm is developed and employed to fit CAE data from brake squeal analysis and simulated CAE and experimental results. The ML-based model significantly saves computational cost by examining the whole design space in operating conditions and skipping unnecessary iterations. In the presented work, the two major features for operating conditions: pressure and temperature taken into consideration, and their corresponding formulation and analytical representation elaborated. A higher-dimension model can be considered in the future to study and include additional parameters for operating conditions such as friction values, disk velocity, and considering geometrical and material variations. Variations could extend into many sub-features that, in some ways, identified but not quantified yet. That includes but not limited to: variations due to the wearing and surface imperfectness, geometry difference because of casting and manufacturing specs and tolerances, materials change due to the material treatment and processes, environmental and cyclic loading conditions which have impacts on both materials and geometries, connections and compliances, etc. On the other side, the Machine-learning model can be further modified and improved. With the advances in AI algorithms and computational resources in recent years, this area is developing exponentially. New algorithms enable capturing more complicated and mechanistic features; therefore, an up-to-date methodology should be considered in future studies that could better demonstrate the real physics of the system and add more critical features. Furthermore, this study evaluated and validated the methodology for only one primary noise frequency; however, to implement this concept in an industrial investigation, the full spectrum of noise frequencies must be considered. Accordingly, the technique should be examined low-mid-high frequency range.

The second part of this research proposes a multi-resolution deep learning approach inspired by physics and data. Then, it develops a deep learning model to predict brake pad NVH modal characteristics from the physical properties. The brake pad, known as the excitation source that crucially affects the brake NVH. Studies have shown the relevance of mode-coupling that arises from neighboring natural frequencies in the brake system on high-frequency noises. This phenomenon is mainly influenced by pads and rotor characteristics, including modal factors and surface-to-surface interactions. In this work, a high-fidelity numerical model developed and correlated with the experimental test data. The numerical model captured the physical aspects of the component. The CAE model then generated a big database using a design of the experiment (DOE) technique to feed the machine learning model.

As the primary solution, a physics-inspired deep learning model developed with a flexible structure to capture multi-dimensional interconnections between the pad's physical properties and the corresponding response. The goal of this ML-based approach is to advance the design and development process for brake NVH and minimize the urgency to additional physical tests and numerical models at component level analysis.

The relationship between the component's physical properties and the ultimate modal response is captured by employing a structured deep learning algorithm. Through this algorithm, separate multi-layer perceptron (MLP) modules developed for each of geometry, materials, and environmental groups of features and eventually concatenated to incorporate adequate complexity required by the input features. It was described that this scheme better represents the physics of the system through the analysis. A unique network structure presented in this work that optimized the model for optimum feasible hyperparameters (hidden layers and hidden units). This scheme is

explained by searching for optimal possible solutions from hundreds of neural networks to achieve minimum complexity and computational costs.

Several areas can be further studied for future work. The first one is to incorporate a more complex representation of input features (including material, geometry, and environmental). While, in this study, a smaller input size was considered to prove the concept. For instance, for geometry, only two geometry features were accounted, and for environmental, only one feature (temperature) was considered as the main factor. However, in the real world, geometry and environmental features would be more complicated. Therefore, more complex geometry features could be added in future work, and also features such as humidity and constraint/loading conditions may be studied. Likewise, including additional material features to explore the behavior within the entire regime. Moreover, another group of features can potentially be included in the inputs, such as manufacturing variations and uncertainties. Another investigation is to expand the database for more experimental tests. Experimental data is a significant challenge because it is costly and challenging to acquire. This is an essential step for employing the proposed technique for product benchmark and design and developments. Additionally, the developed machine-learning algorithm could be modified, capturing a more efficient optimization for parameters and hyperparameters, so the modified model outperforms the baseline. This could be critical when a more extensive database is acquired. The sampling method could also be reformed concerning scalability and computational efficiency. Finally, the methodology can be extended and applied to other brake components to generate a powerful, efficient design tool for component NVH analysis.

APPENDIX

Machine Learning Code:
A Deep Learning Technique to Predict Brake Pad NVH Modal Characteristics Based on Physical Properties

Jupiter Notebook (Intuitive-Deep-Learning) Python 3

```
# ****************************************
# import the necessary packages
import pandas as pd
import numpy as np
from sklearn import preprocessing
from sklearn.utils import shuffle
from sklearn.model_selection import train_test_split
import tensorflow as tf
from tensorflow import keras
from tensorflow.keras import backend as K
import keras.backend as K
from keras.layers.normalization import BatchNormalization
import matplotlib.pyplot as plt
from keras.models import Sequential
from keras.optimizers import Adam
from keras.optimizers import rmsprop
from keras.models import Model
from keras.layers import Concatenate, Dense, LSTM, Input, Activation, Flatt
en, concatenate
from keras.layers import Dropout
from keras import regularizers
from sklearn.model_selection import KFold
import numpy as np
from keras.losses import mean_squared_error
```

```python
# ****************************************
# reading data
df = pd.read_csv("datasets/Pad_DOE_Data_EM12.csv", sep=",")
dataset = df.values
X_g= dataset[:,0:2]
X_m= dataset[:,2:6]
X_t= dataset[:,6:7]
Y= dataset[:,7:13]


# ****************************************
# data cleaning


df = shuffle(df)
min_max_scaler = preprocessing.MinMaxScaler()
X_g_scale = min_max_scaler.fit_transform(X_g)
X_m_scale = min_max_scaler.fit_transform(X_m)
X_t_scale = min_max_scaler.fit_transform(X_t)
Y_scale = min_max_scaler.fit_transform(Y)


# data slpit
split = train_test_split(X_g_scale, X_m_scale,X_t_scale,Y_scale, test_size=
0.1)
(X_g_train, X_g_val, X_m_train, X_m_val, X_t_train, X_t_val,Y_train, Y_val)
= split


training_samples = Y_train.shape[0]
print(f'> Training_Samples: {training_samples}')
print(f'> Geometry_Inputs: {X_g_train.shape[1]}, Materials_Inputs: {X_m_tra
in.shape[1]}, Enviormental_Inputs: {X_t_train.shape[1]},  Response_Outputs
: {Y_train.shape[1]}')


# ****************************************
# model parameters


L_bound_neurons = 8
H_bound_neurons = 40
n_doe_size = 100
```

```python
par_constrain = 0.8 * training_samples
opt = rmsprop(lr=1e-3, decay=1e-3 / 200)


# ****************************************
# initial values


verbosity = 1
n_g1= np.random.randint(L_bound_neurons,H_bound_neurons,n_doe_size)
n_m1=np.random.randint(L_bound_neurons,H_bound_neurons,n_doe_size)
n_t1=np.random.randint(L_bound_neurons,H_bound_neurons,n_doe_size)
NN_s1 = 1
acc_per_NN_s1 = []
loss_per_NN_s1 = []
params_per_NN_s1 = []
neurons_feas_s1 = []
neurons_feas_s1 = [[0, 0, 0, 0]]
loss_best_NN_s1 = loss_best_NN_f_s1 = 1
best_NN_f_s1 = 0


# ****************************************
# model DNN S-1 : [1,1,1]
for n in np.arange(len(n_t1)):
    def create_mlp(dim_h,dim_out):
        model = Sequential()
        for i in np.arange(len(dim_h)-1):


            model.add(Dense(dim_h[i+1], input_dim=dim_h[i], activation="rel
u"))
        model.add(Dense(dim_out, activation="relu"))
        return model


    mlp_g1 = create_mlp([X_g_train.shape[1],n_g1[n]],12)
    mlp_m1 = create_mlp([X_m_train.shape[1],n_m1[n]],12)
    mlp_t1 = create_mlp([X_t_train.shape[1],n_t1[n]],6)
```

```
    combinedInput_s1 = concatenate([mlp_g1.output, mlp_m1.output, mlp_t1.ou
tput])


    prediction_s1 = Dense(6, activation="linear")(combinedInput_s1)


    model_s1 = Model(inputs=[mlp_g1.input, mlp_m1.input, mlp_t1.input], out
puts=prediction_s1)



    def root_mean_squared_error_s1(Y_scale,prediction_s1):
        return K.sqrt(mean_squared_error(Y_scale,prediction_s1))


    print('NN_s1 ',NN_s1)
    model_s1.compile(optimizer=opt,loss=root_mean_squared_error_s1,metrics=
['accuracy'])
    model_s1.summary()
    hist_s1 = model_s1.fit(
        [X_g_train, X_m_train, X_t_train],Y_train,
            validation_data=([X_g_val, X_m_val, X_t_val],Y_val),
                epochs=16,
                batch_size=64,
                verbose=verbosity)
    scores_s1 = model_s1.evaluate([X_g_val, X_m_val, X_t_val],Y_val, verbos
e=0)
    parnum_s1 = model_s1.count_params()
    loss_per_NN_s1.append(scores_s1[0])
    params_per_NN_s1.append(parnum_s1)
    NN_s1=(NN_s1)+1


print('--------------------------------------------------------------------
--------------------------------')
print(f'> NN_s1 () : geo1 - mat1 - temp1      (Par. Constrain: N of Par. <
{par_constrain})')
for j in range(0, len(loss_per_NN_s1)):
    if (params_per_NN_s1[j] < par_constrain):
            print(f'> NN_s1({j+1}): Loss: {loss_per_NN_s1[j]} N of Par.
: {params_per_NN_s1[j]}')
            neurons_feas_s1 = np.append(neurons_feas_s1, [[n_g1[j], n_m
1[j], n_t1[j], loss_per_NN_s1[j]]], axis=0)
```

```python
                if (loss_per_NN_s1[j] < loss_best_NN_f_s1):
                    loss_best_NN_f_s1=loss_per_NN_s1[j];best_NN_f_s1 = j+1;
best_par_f_s1 = params_per_NN_s1[j];
print('Best Feasible NN for s1:')
print(f'> NN_s1({best_NN_f_s1}): Loss: {loss_best_NN_f_s1}   N of Par.: {be
st_par_f_s1}')
if (best_par_f_s1 < 1):
    print('No Feasible NN for s1')



# *****************************************
# design iterations 3D plot


from mpl_toolkits import mplot3d
%matplotlib inline
import numpy as np
from matplotlib import cm
from matplotlib.ticker import LinearLocator, FormatStrFormatter
import matplotlib.pyplot as plt
from mpl_toolkits.mplot3d import Axes3D
fig = plt.figure(figsize=plt.figaspect(0.25))
ax1 = fig.add_subplot(1, 3, 1, projection='3d')
scatter_plot1=ax1.scatter(n_g1, n_m1, loss_per_NN_s1, c=loss_per_NN_s1, cma
p='RdBu', linewidth=5, alpha=0.5);
cb1=fig.colorbar(scatter_plot1, cmap='RdBu', shrink=0.6, aspect=12);
ax2 = fig.add_subplot(1, 3, 2, projection='3d')
scatter_plot2=ax2.scatter(n_g1, n_t1, loss_per_NN_s1, c=loss_per_NN_s1, cma
p='RdBu', linewidth=5, alpha=0.5);
cb2=fig.colorbar(scatter_plot2, cmap='RdBu', shrink=0.6, aspect=12);
ax3 = fig.add_subplot(1, 3, 3, projection='3d')
scatter_plot3=ax3.scatter(n_m1, n_t1, loss_per_NN_s1, c=loss_per_NN_s1, cma
p='RdBu', linewidth=5, alpha=0.5);
cb3=fig.colorbar(scatter_plot2, cmap='RdBu', shrink=0.6, aspect=12);


ax1.view_init(elev=20, azim=225);ax1.dist=11;ax2.view_init(elev=20, azim=22
5);ax2.dist=11;ax3.view_init(elev=20, azim=225);ax3.dist=11;
ax1.set_title('Neurons: Geometry vs Material Layers');ax2.set_title('Neuron
s: Geometry vs Enviormental Layers');ax3.set_title('Neurons: Material vs En
viormental Layers');
```

```
ax1.set_xlabel('neurons geo_layer', labelpad=2);ax1.set_ylabel('neurons mat
_layer', labelpad=2);ax1.set_zlabel('loss per NN', labelpad=5);
ax2.set_xlabel('neurons geo_layer', labelpad=2);ax2.set_ylabel('neurons tem
p_layer', labelpad=2);ax2.set_zlabel('loss per NN', labelpad=5);
ax3.set_xlabel('neurons mat_layer', labelpad=2);ax3.set_ylabel('neurons tem
p_layer', labelpad=2);ax3.set_zlabel('loss per NN', labelpad=5);


# ****************************************
# design iterations heatmap

%matplotlib inline
import pandas as pd
import matplotlib.pyplot as plt
import seaborn as sns
import numpy as np
n_feas= neurons_feas_s1[1:,:]
df = pd.DataFrame(n_feas)


df.columns=['neurons geo_layer','neurons mat_layer','neurons temp_layer','l
oss_per_NN']
df_copy =  df.copy()
df_copy.drop_duplicates(subset=['neurons geo_layer', 'neurons mat_layer'],i
nplace=True)
df_copy.drop_duplicates(subset=['neurons mat_layer','neurons temp_layer'],i
nplace=True)
df_copy.drop_duplicates(subset=['neurons geo_layer','neurons temp_layer'],i
nplace=True)


geo_mat = df_copy.pivot(index='neurons geo_layer',columns='neurons mat_laye
r', values='loss_per_NN')
geo_temp = df_copy.pivot(index='neurons geo_layer',columns='neurons temp_la
yer', values='loss_per_NN')
mat_temp = df_copy.pivot(index='neurons mat_layer',columns='neurons temp_la
yer', values='loss_per_NN')


fig, ax1 = plt.subplots(1,3, figsize = (16,4))
sns.heatmap(geo_mat,cmap='RdBu',ax=ax1[0])
sns.heatmap(geo_temp,cmap='RdBu',ax=ax1[1])
```

```
sns.heatmap(mat_temp,cmap='RdBu',ax=ax1[2])


ax1[0].set_title('Neurons: Geometry vs Material Layers', fontsize = 12)

ax1[1].set_title('Neurons: Geometry vs Enviormental Layers', fontsize = 12)

ax1[2].set_title('Neurons: Material vs Enviormental Layers', fontsize = 12)


# ****************************************
# loss vs epoch plot


plt.plot(hist_s1.history['loss'], color='blue', linewidth=3, marker='x')

plt.plot(hist_s1.history['val_loss'], color='red', linewidth=3, marker='o')

plt.title('Model loss vs Epoch')

plt.ylabel('Loss')

plt.xlabel('Epoch')

plt.legend(['Training', 'Validation'], loc='upper right')

plt.show()
```

BIBLIOGRAPHY

Aboudi J., Arnold S. M. and Bednarcyk B. A., Micromechanics of Composite Materials, Elsevier Inc., Chapter 2 - Constituent Material Modeling, 2.1.1.2 Transversely Isotropic in Global Coordinates, (2013), , ISBN 978-0-12-397035-0

AbuBakar A. R. and Ouyang H. J.,"Complex eigenvalue analysis and dynamic transient analysis in predicting disc brake squeal", International Journal of Vehicle Noise and Vibrations, (2006), vol. 2, no. 2, pp. 143–155

Adhikari S., "Damping Models for Structural Vibration", Ph.D. thesis, Cambridge University Engineering Department, Cambridge, UK., (2000)

Adhikari S. and Friswell M.I., "Random matrix eigenvalue problem in structural dynamics", International Journal for Numerical Methods in Engineering, (2007), 69, 562-591

Akay A., "Acoustics of friction", Journal of the Acoustical Society of America, (2002), Vol. 111, Issue 4, p. 1525-1548

Alemani M., Gialanella S., Straffelini G., et al., "Dry sliding of a low steel friction material against cast iron at different loads: characterization of the friction layer and wear debris" Wear, (2017), 376–377:1450–9

Angermueller C., Lee H. J., Reik W. and Stegle O. "Deepcpg: accurate prediction of single-cell dna methylation states using deep learning", Genome Biol., (2017)

Augsburg K., Günther H., Abendroth H., and Wernitz B., "Comparison Between Different Investigation Methods of Quasi-Static and Dynamic Brake Pad Behaviour", SAE Technical Paper, (2003), 2003-01-3340

Bae J.C. and Wickert J.A., "Free vibration of coupled disk-hat structures", Journal of Sound Vibration, (2000), 235(1), pp. 117–132

Bajer A. and Belsky V., "The Influence of Friction-Induced Damping and Nonlinear Effects on Brake Squeal Analysis" ABAQUS, Inc. Shih-Wei Kung Delphi Corporation, 22nd Annual Brake Colloquium & Exhibition. Anaheim, California. SAE TECHNICAL PAPER SERIES, (2004), 01-2794

Bajer A., Belsky V. and Zeng L. J., "Combining a Nonlinear Static Analysis and Complex Eigenvalue Extraction in Brake Squeal Simulation", SAE Technical Paper, (2003), 2003-01-3349

Baker N., Alexander F., Bremer T., et al., "Workshop report on basic research needs for scientific machine learning: Core technologies for artificial intelligence", Technical Report. USDOE Office of Science, (2019)

Brake Lining Standards Committee, "Friction Material Elastic Property Measurement", SAE Standard J2725, Rev. Sep. 2017

Brecht J., Elvenkemper A., Betten J., Navrath U. and Multhoff J., "Elastic Properties of Friction Materials." SAE Transactions, (2003), 112, 2393-2400

Breuer B. and Bill K.H., "Brake Technology Handbook", SAE International, Warrendale, PA, March, (2008), ISBN 978-0-7680-1787-8

Brunel J.F. and Dufrénoy P.,"Transient analysis of squealing mode selection in disc brake", Tech. Rep., SAE, Warrendale, PA, (2008), Paper No. 2008-01-2537

Caughey T., "Classical normal modes in damped linear systems", Journal of Applied Mechanics, (1960), 27: p. 3

Cerna M. and Harvey A., "The Fundamentals of FFT-Based Signal Analysis and Measurement, National Instruments", Application Note 041, (2000)

Chen F. "Vehicle front brake cold squeal root cause study and resolution", Ford NVH Newsletter, (2002), Vol. 5, No. 2, pp.15, 16

Chen F., "Disc brake squeal: an overview", Tech. Rep., SAE, Warrendale, PA, (2007), Paper No. 2007-01-0587

Chen F., "Automotive disk brake squeal _ an overview", International Journal of Vehicle Design, (2009), Vol. 51, Nos. 1/2,

Chen F., Abdelhamid M. K., Blashke P., and Swayze J., "On automotive disc brake squeal. Part III: test and evaluation." SAE Technical Paper, (2003b)

Chen F. and McKillip D., "Laser metrology: state of the art in the automotive applications", in Arkin, W.T. (Ed.): New Trends in Lasers and Electro-Optics, Nova Science Publishers Inc., New York, (2008), pp.61–90

Chen F., Tan C. A., and Quaglia R. L., "On automotive disc brake squeal. Part I: mechanisms and causes." SAE Technical Paper, (2003a)

Chen F., Tan C. A., and Quaglia R.L., Disc brake squeal – mechanism, analysis, evaluation, and reduction/prevention, SAE International, Warrendale, PA, (2006), ISBN 978-0-7680-1248-4

Chen G.X., Zhou Z.R., Kapsa P., and Vincent L., "Effect of surface topography on formation of squeal under reciprocating sliding", Wear, (2002), 253, pp. 411–423

Chen W. and Fuge M., "Synthesizing Designs with Interpart Dependencies Using Hierarchical Generative Adversarial Networks" ASME. J. Mech. Des., (2019), 141(11): 111403

Ching T., Elton D. C., Titus A. J., et al. "Opportunities and obstacles for deep learning in biology and medicine", Journal of the Royal Society Interface, (2017), Volume 15, Issue 141, doi: /10.1098/rsif.2017.0387

Craven M. W. and Shavlik J. W. "Using neural networks for data mining" Future Generation Comput. Syst., (1997), 13, 211–229

Dai Y. and Lim T.C., "Suppression of brake squeal noise applying finite element brake and pad model enhanced by spectral-based assurance criteria", Appl. Acoust., (2008), 69, pp. 196–214

Denys E., Kappagantu R. and Mahajan S., "Issues and Tools in Prediction of Composite Loss Factors for the Brake Pad-Insulator System", SAE Paper, (2006)

Deng L., Li J., Huang J.-T., Yao K., Yu D., et al., "Recent advances in deep learning for speech research at Microsoft", in ICASSP, (2013)

Dunlap K.B., M.A. Riehle, and R.E. Longhouse, "An investigative overview of automobile disc brake noise", Tech. Rep., SAE, Warrendale, PA, (1999), Paper No. 1999-01-0142,

Earles S.W.E., "A mechanism of disc-brake squeal", Tech. Rep., SAE, Warrendale, PA, (1977), Paper No. 770181

Earles S.W.E. and Badi M.N.M., "Oscillatory instabilities generated in a double-pin and disc undamped system: a mechanism of disc-brake squeal", Proc. IMechE C 198 (4), (1984), pp. 43–50

Earles S.W.E. and Chambers P.W., "Disc brake squeal noise generation: predicting its dependency on system parameters including damping", International Journal of Vehicle Design, (1987), 8 (4/5/6), pp. 538–552

Earles S.W.E. and Lee C., "Instabilities arising from the frictional interaction of a pin-disk system resulting in noise generation", Trans. Amer. Soc. Mech. Eng. J. Eng. Industry, (1976), 98 (1), pp. 81–86

Earles S.W.E. and Soar G.B., "Squeal noise in disc brakes", Vibration and Noise in Motor Vehicles, Institution of Mechanical Engineers, London, England, (1971), Paper No. C 101/71, pp. 61–69

Eriksson M., Bergman F. and Jacobson S., "Surface characterisation of brake pads after running under silent and squealing conditions" Wear, (1999), 232, 163–167

Eriksson M., Lundqvist A. and Jacobson S. "A study of the influence of humidity on the friction and squeal generation of automotive brake pad", IMechE, Proc. Instn. Mech. Engrs., (2001), Vol. 215, No. 3, Part D, pp.329–342

Esgandari M., Olatunbosun O. and Taulbut R., "Effect of damping in complex eigenvalue analysis of brake noise to control over-prediction of instabilities: an experimental study", SAE Brake Colloquium, Jacksonville, FL: SAE International, (2013a)

Esser S. K., Merolla P. A., Cassidy A. S., et al., "Convolutional networks for fast, energy-efficient neuromorphic computing", Proceedings of the National Academy of Sciences, (2016)

Esteva A., Robicquet A., Ramsundar B., et al., "A guide to deep learning in healthcare", Nat Med, (2019), 25, 24–29

Every, A.G., "Determination of the Elastic Constants of Anisotropic Solids", NDT International, (1993), Vol. 27, No. 1, p. 3

Every, A.G. and McCurdy, A.K., Landolt-Bornstein New Series Group II, vol. 29a. ed. Madelung, Springer, Berlin, (1992)

Fieldhouse, J.D., Ashraf, N., Talbot, C., Pasquet, T., et al., "Measurement of the Dynamic Center Pressure of a Brake Pad during a Braking Operation", SAE Paper, (2006)

Garg S. "Derivatives of eigensolutions for a general matrix", AIAA J, (1973), 11:1191–1194

Geradin M. and Rixen D., Mechanical Vibrations. Theory and Application to Structural Dynamics., John Wiley & Wiley and Sons, (1994), ISBN: 978-1-118-90020-8

Giannini O. and Sestieri A., "Predictive model of squeal noise occurring on a laboratory brake" Journal of Sound Vibration, (2006), 296, pp. 583–601

Girshick R., J. Donahue, T. Darrell, and J. Malik, "Rich Feature Hierarchies for Accurate Object Detection and Semantic Segmentation," in CVPR, (2014)

Hamzeh O. N., W. Tworzydlo, H. J. Chang, and S. Fryska, "Analysis of Friction-Induced Instabilities in a Simplified Aircraft Brake", SAE Brake Colloquium, (1999)

Hassoun M.H., "Fundamentals of artificial neural networks", Journal of Proceedings of the IEEE, (1996), 84 (6): 906

Hayes A.F. and Matthes J., "Computational procedures for probing interactions in OLS and logistic regression: SPSS and SAS implementations", Behavior Research Methods, (2009), 41, 924–936

Haykin S. S., Neural Networks: A Comprehensive Foundation, Maxwell Macmillan International, (1994), 2nd Edition, ISBN-13: 978-0132733502

Hoffmann N., Fischer M., Allgaier R. and Gaul L., "A minimal model for studying properties of the mode-coupling type instability in friction induced oscillation" Mech. Res. Commun., (2002), 29 (4), 197_205

Hoffmann N. and Gaul L., "Friction induced vibrations of brakes – research fields and activities" SAE paper, (2008), 01-2578

Hogg R. V., McKean J., and Craig A. T., Introduction to mathematical statistics, 7th. ed., Harlow, Essex: Pearson Education, (2014), ISBN-13: 978-0321795434

Hsieh W. W., Machine learning methods in the environmental sciences: Neural networks and kernels, Cambridge University Press, (2009), ISBN: 9780511627217

Hugues A., "A perspective on interaction effects in genetic association studies", Genetic Epidemiology, (2016), 10.1002/gepi.21989, 40, 8, (678-688)

Ichiba Y. and Nagasawa Y., "Experimental study on disc brake squeal", Tech. Rep., SAE, Paper No. 930802, Warrendale, PA, (1993)

Ivezic Z., Connolly A. J., VanderPlas J. T., and Gray A., Statistics, data mining, and machine learning in astronomy: a practical Python guide for the analysis of survey data, Princeton University Press, (2019), ISBN: 9780691198309

Jaccard J. and Turrisi R., Quantitative Applications in the Social Sciences: Interaction effects in multiple regression., Thousand Oaks, CA: SAGE Publications, (2003), Inc. doi: 10.4135/9781412984522

Kang J., Krousgrill C.M. and Sadeghi F., "Comprehensive stability analysis of disc brake vibrations including gyroscopic, negative friction slope and mode- coupling mechanisms" Journal of Sound and Vibration, (2009), 324(1-2): p. 387-407

Karpatne A., Atluri G., Faghmous J.H., et al., "Theory-guided data science: A new paradigm for scientific discovery from data" IEEE Transactions on Knowledge and Data Engineering, (2017), 29(10), pp.2318-2331

Karpatne A., Ravela S., Babaie H.A., et al., "Machine learning for the geosciences: Challenges and opportunities", IEEE Transactions on Knowledge and Data Engineering, (2019), vol. 31, no. 8, pp. 1544-1554, doi: 10.1109/TKDE.2018.2861006

Kinkaid N.M., O'Reilly O.M. and Papadopoulos P., "Automotive disc brake squeal: a review", Journal of Sound and Vibration, (2003), Vol. 267, No. 1, pp.105–166

Kinkaid N.M., O'Reilly O.M. and Papadopoulos P., "On the transient dynamics of a multi-degree-of-freedom friction oscillator, a new mechanism for disc brake noise", Journal of Sound and Vibration, (2005), 287 pp. 901–917

Kobayashi M. and Odani N., "Study on Stabilization Friction Coefficient of Disc Brake Pads in Cold Condition", SAE Paper, (1997), 973030

Koch M., Blaschke P. and Willner K., "The Role of Climatic Conditions on Disc Brake Noise", SAE Paper, (2006), 2006-01-3209

Kustikova V.D. and Druzhkov P.N., "A survey of deep learning methods and software for image classification and object detection", Pattern Recognit. Image Anal., (2016), 26, 9–15

Kutz J. N., "Deep learning in fluid dynamics.", Journal of Fluid Mechanics, (2017), 814, 1-4

Lecun Y., Bengio Y., Hinton G. "Deep learning", Nature, 2015, 521 (7553): 436-444

Lee H., "An Optimal Design Method for Brake Squeal Noise Based on Complex Eigenvalue and Sensitivity Analysis and Response Surface Methodology", PhD dissertation at the University of Michigan, (2000), UMI number: 9963833

Lee S., Jeon J., Jeong J., Park B., et al., "Disc Brake Squeal vs. Disc Pad Compressibility-Caliper Stiffness Interactions: Low-Frequency Squeal and High-Frequency Squeal vs. Differential Pad Wear", SAE Technical Paper, (2017), 2017-01-2528,

Lee Y. S., Brooks P.C., Barton D.C. and Crolla D.A., "An integrated finite element approach to modeling disc brake squeal", Proceedings of FISITA, (1996), B0404,

Leona S. A., West S. G., and Reno R., Multiple regression: Testing and interpreting interactions, SAGE Publication Inc., (1991), ISBN-13: 978-0761907121

Liles G.D., "Analysis of Disc Brake Squeal Using Finite Element Methods", SAE Paper, (1989), 891150

Lindeman R. H., Merenda P. F. and Gold, R. Z., Introduction to bivariate and multivariate analysis, Glenview, IL: Scott, Foresman and Company, (1980)

Liu M. and Gorman D.G., "Formulation of Rayleigh damping and its extensions", Computers & Structures, (1995), 57(2): p. 277-285

Liu W., Vyletel G.M. and Li J., "A Rapid Design Tool and Methodology for Reducing High Frequency Squeal", SAE Paper, (2006)

Lou G., Lee L., and Malott B., "Introduction of Anisotropic Lining Elastic Constants Optimization (ALCO) Method for Friction Materials", SAE Technical Paper, (2007)

Lynch M. E., Sarkar S. and Maute K. "Machine Learning to Aid Tuning of Numerical Parameters in Topology Optimization" ASME. J. Mech. Des., (2019), 141(11): 114502

Malmassari C., Cucchi F., Yuhas D., et al., "Evolution of Brake Noise Performance and its Relation to Variations in Friction Material Elastic Properties", EuroBrake, Dresden, Germany, (2015), /EB2015-NVH-011

Matsuzaki M. and Izumihara T., "Brake noise caused by longitudinal vibration of the disc rotor", Tech. Rep., SAE Paper, Warrendale, PA, (1993), Paper No. 930804

Massi F., Giannini O. and Baillet L., "Brake squeal as dynamic instability: an experimental investigation" Journal of the Acoustical Society of America, Vol. 120, Issue 3, (2006), p. 1388-1398

Márcia B., Elsa H. and Kai G., "More effective prognostics with elbow point detection and deep learning", Mechanical Systems and Signal Processing, (2020), 146. 1-23. 10.1016/j.ymssp.2020.106987

Meerbergen K., "Fast frequency response computation for Rayleigh damping" International Journal for Numerical Methods in Engineering, (2008), 73(1): p. 96-106

Mitchell T. M., Machine Learning, McGraw Hill, New York, (1997)

Miyoshi K. and Buckley D.H., "Effects of water vapor on friction and deformation of polymeric magnetic media in contact with a ceramic oxide", In Bushman B. (Eds.): Tribology and Mechanics of Magnetic Storage Systems, ASLE, SP-16, (1984), pp.27–34

Mottershead J.E., "Vibration- and friction-induced instability in disks", Journal of Shock and Vibration Digest, (1998), 30 (1), pp. 14–31

Mottershead J.E. and Chan S.N., "Flutter instability of circular discs with frictional follower loads", ASME J. Vibration Acoust., (1995), 117, pp. 161–163

Mottershead J.E., Ouyang H., Cartmell M. and Friswell M., "Parametric Resonances in an Annular Disc, with a Rotating System of Distributed Mass and Elasticity; And the Effects of Friction and Damping", Proceedings of The Royal Society A: Mathematical, Physical and Engineering Sciences, (1997), 453. 1-19. 10.1098/rspa.1997.0001

Nack W.V., "Brake squeal analysis by finite elements", International Journal of Vehicle Design, (2000), 23 (3/4), pp. 263–275

Nack W.V. and Joshi A.M., "Friction induced vibration: brake moan", Tech. Rep., SAE Paper, Warrendale, PA, (1995), No. 951095

Nagy L.I., Cheng J. and Hu Y. "A New Method Development to Predict Brake Squeal Occurrence", SAE Paper, (1994), 942258

Newland D. E., Mechanical Vibration Analysis and Computation., Longman, Harlow and John Wiley, New York, (1989)

Nishioka M., Hara Y., Nomoto M. and Ono M., "Brake Squeals after Standing in Low Temperatures", SAE Paper, (2006)

Nouby M., Abdo J., Mathivanan D., and Srinivasan K. "Evaluation of disc brake materials for squeal reduction" Tribology Transactions, (2011), 54(4), 644-656

Nouby M., Mathivanan D. and Srinivasan K., "A combined approach of complex eigenvalue analysis and design of experiments (DOE) to study disc brake squeal", International Journal of Engineering Science and Technology, (2009), Vol. 1, No. 1, pp.254–271

Oberst S. and Lai J. C. S., "Chaos in brake squeal noise", Journal of Sound and Vibration, (2011), 330(5), 955-975

Oberst S. and Lai J. C. S., "Statistical analysis of brake squeal noise", Journal of Sound and Vibration, (2011), 330(12), 2978- 2994

Oura Y., Kurita Y, Matsumura Y., and Nishizawa Y., "Influence of distributed stiffness in contact surface on disk brake squeal", Tech. Rep., SAE Paper, Warrendale, PA, (2008), No. 2008-01-2584

Ouyang H., Cao Q., Mottershead J.E., and Treyde T., "Vibration and squeal of a disc brake: modelling and experimental results", Proceedings of the Institution of Mechanical Engineers, Part D: Journal of Automobile Engineering, (2003), 217 (10), pp. 867–875

Ouyang H., Mottershead J.E. and Li W., "A moving-load model for disc-brake stability analysis", ASME J.Vib. Acoust., (2003), 125 (1), pp. 1–6

Ouyang H., Nack W. V., Yuan Y. and Chen F., "Numerical analysis of automotive disc brake squeal: a review", International Journal Vehicle Noise and Vibrations, (2005), Vol. 1, Nos. 3-4, 207-230

Panchal J. H., Fuge M., Liu Y., Missoum S., and Tucker C., "Special Issue: Machine Learning for Engineering Design", ASME. J. Mech. Des.,(2019), 141(11): 110301

Papinniemi A., Lai J.C.S., Zhao J. and Loader L., "Brake squeal: a literature review", Appl. Acoust., (2002), 63: 391-400

Pham D.T. and Afify A.A., "Machine-learning techniques and their applications in manufacturing", Proceedings of the Institution of Mechanical Engineers, Part B: Journal of Engineering Manufacture, (2005), 219(5):395-412, doi:10.1243/095440505X32274

Pham D. T. and Liu X., Neural Networks for Identification, Prediction and Control, Springer-Verlag, London, (1999), ISBN 978-1-4471-3244-8

Pouyanfar S., Yang Y., Chen S. C., Shyu M. L. and Iyengar S. S., "Multimedia big data analytics: A survey", ACM Comput. Surveys, vol. 51, no. 92, pp. 1-36, (2018)

Raccuglia P., Elbert K. C, Adler P. DF, Falk C., et al., "Machine-learning-assisted materials discovery using failed experiments", Nature 533, (2016), 7601, 73–76

Rai R. and Sahu C. K., "Driven by Data or Derived Through Physics? A Review of Hybrid Physics Guided Machine Learning Techniques with Cyber-Physical System (CPS) Focus", in IEEE Access, (2020), vol. 8, pp. 71050-71073, doi: 10.1109/ACCESS.2020.2987324

Raina A., McComb C., and Cagan J., "Learning to Design from Humans: Imitating Human Designers Through Deep Learning" ASME. J. Mech. Des., (2019), 141(11): 111102

Russakovsky O., Deng J., Su H., et al., "ImageNet Large Scale Visual Recognition Challenge", International Journal of Computer Vision (IJCV), (2015), vol. 115, no. 3, pp. 211–252

SAE International Surface Vehicle Recommended Practice, "Automotive Disc Brake Pad Natural Frequency and Damping Test", SAE Standard J2598, Rev. Jul. 2012

SAE International Surface Vehicle Recommended Practice, "Disc and Drum Brake Dynamometer Squeal Noise Test Procedure," SAE Standard J2521, Rev. Apr. 2013

SAE J2521 (2005) "Brake Noise Dynamometer Test Procedure", Published by US Working Group

Saleem H., Gilmar F. B. and Bekir Y., Comprehensive Materials Processing, Elsevier Inc., (2014), Chapter 2 - Materials Modeling and Characterization, 2.04.3.2 - Ultrasonic Characterization of Anisotropic Materials, ISBN 978-0-08-096533-8

Sanders P. and Yuhas D., "Friction Material Elastic Property Round Robin Study", SAE Technical Paper, (2007), 2007-01-3940, https://doi.org/10.4271/2007-01-3940

Sanders P.G., Xu N., Dalka T.M. and Maricq M.M., "Airborne brake wear Debris: size distributions, composition, and a comparison of dynamometer and vehicle tests" Environ Sci Technol, (2003), 37:4060–9

Sasaki Y. and Kusaka S., "The Transition of Automotive Brake Lining Materials", Journal of Japanese Society of Tribologists, (2003), Vol.41, No.4, p.197-201

Schleder G. R., Padilha A., Acosta C. M., et al., "From DFT to machine learning: recent approaches to materials science–a review" Journal of Physics: Materials 2, 3 (2019), 032001

Schreiber E., Anderson O.L. and Soga M., Elastic Constants and Their Measurement, McGraw-Hill, New York, (1973)

Spurr R. T., "Brake Squeal", Institution of Mechanical Engineers, Conference on Road Braking, (1971), C95/71, 13-16

Sriwiboon M., Tiempan N., Kaewlob K., Rhee S., and Yuhas D., "Disc Pad Physical Properties vs. Porosity: The Question of Compressibility as an Intrinsic Physical Property", SAE International Journal of Materials and Manufacturing, (2018), 11(1), 57-78. doi:10.2307/26556831

Steege R. and Marx F., "A New Approach to Material Compressibility of Brake Pads", SAE Technical Paper, (2008), 2008-01-2572, doi:10.4271/2008-01-2572

Stender M., Tiedemann M., Spieler D., et al., "Deep learning for brake squeal: Brake noise detection, characterization and prediction", Mechanical Systems and Signal Processing, (2021), 149. 107181. 10.1016/j.ymssp.2020.107181

Strickland I. and Yuhas D., "Development of Correlation Between Experimental and Analytical Modal Analysis of Brake Pads", SAE Technical Paper 962130, (1996)

Sze V., Chen Y., Yang T. and Emer J. S., "Efficient Processing of Deep Neural Networks: A Tutorial and Survey", in Proceedings of the IEEE, (2017), vol. 105, no. 12, pp. 2295-2329, doi: 10.1109/JPROC.2017.2761740

Towell G. G. and Shavlik J. W. "The extraction of refined rules from knowledge-based neural networks", Machine Learning, (1993), 13(1), 71–101

Triches M.J., Gerges S.N.Y. and Jordan R., "Reduction of squeal noise from disc brake systems using constrained layer damping", Journal of the Brazilian Society of Mechanical Science and Engineering, (2004), 26, 340–348

Truell R., Elbaum C. and Chick B.B., Ultrasonic Methods in Solid State Physics, Academic Press, New York, (1969), ISBN978-1-4832-3318-5

VanRullen R., "Perception science in the age of deep neural networks", Frontiers in Psychology, (2017), vol. 8, p. 142

Wegmann E. and Dohle A., "Correlation Analysis between Friction Material Parameters and the NVH Behavior", SAE Technical Paper, (2015), 2015-01-2686, doi:10.4271/2015-01-2686

Wegmann E., Dohle A. and Stähler T., "Non-Destructive Dynamic Material Parameter Measurement on Entire Brake", EuroBrake, (2010), 2010-01-1701, EB2015-FMC-019

Willard J., Jia X., Xu S., et al., "Integrating Physics-Based Modeling with Machine Learning: A Survey", Association for Computing Machinery, (2020), Vol. 1, No. 1, doi:10.1145/1122445.1122456

Yuhas D., Gesch E., Yamane T., Vorres C., et al., "Comparative Studies of Non-destructive Methods for As-manufactured Brake Pads", SAE Technical Paper, (2010), 2010-01-1701